PETROLOGY, THERMOCHRONOLOGY, AND TECTONIC SIGNIFICANCE OF CORONITIC MAFIC GRANULTIES SOUTHAMPTON ISLAND, NUNAVUT

Christopher J.A. Yakymchuk

Submitted in Partial Fulfilment of the Requirements
For the Degree of Bachelor of Sciences, Honours
Department of Earth Sciences
Dalhousie University, Halifax, Nova Scotia

Abstract

This study presents the first *P-T* estimates and $^{40}Ar/^{39}Ar$ dates from mafic granulite enclaves from Southampton Island, south-central Nunavut, indicating a tectonmetamorphic affinity to the Rae domain of the western Churchill Province. Southampton Island occupies the "Dorset corridor", the enigmatic boundary region between the Trans-Hudson Orogen and the western Churchill Province. The eastern part of the island is underlain largely by granulite and upper amphibolite facies metagranitoid rocks, with local supracrustal enclaves. Mineral assemblages, textures, and *P-T* estimates in mafic enclaves from the eastern part of the island shed light on first-order aspects of the regional tectonometamorphic history. Most samples contain the granulite facies assemblage Grt + Opx + Cpx + Plag ± Hbl, with spectacular coronitic textures developed around garnet porphyroblasts. Three suites of texturally heterogeneous granulites each preserve three textural domains, interpreted to represent three points on the *P-T* path: (1) near-peak metamorphic conditions of 850-900 °C and 9-12 kbar; (2) near-isothermal decompression to 750-850°C and 7-9 kbar; (3) retrogression to amphibolite-facies conditions. $^{40}Ar/^{39}Ar$ thermochronology on hornblende yields ages of 1750-1720 Ma. The *P-T-t* evolution documented by these samples is interpreted to represent tectonic thickening, tectonic transport to mid-crustal levels, intrusion of granites, slow cooling and exhumation controlled by thrusting and erosion. Similar *P-T-t* estimates from the western Churchill Province indicate Southampton Island may be the southeast extent of the Rae Province.

Key Words: mafic granulite, coronite, Trans-Hudson Orogen, thermobarometery, thermochronology

TABLE OF CONTENTS

TABLE OF TABLES

Table of Figures

TABLE OF MINERAL ABBREVIATIONS

Mineral	Abbreviation
Anorthite	An
Almandine	Alm
Biotite	Bt
Chalcopyrite	Ccp
Clinopyroxene	Cpx
Diopside	Di
Enstatite	En
Ferrosilite	Fs
Grossular	Grs
Hedenbergite	Hd
Hercynite	Hc
Ilmenite	Ilm
Orthopyroxene	Opx
Pargasite	Prg
Plagiolcase	Plag
Pyrite	Py
Pyrope	Prp
Spessartine	Sps
Spinel	Spl
Quartz	Qtz

After Kretz (1983)

ACKNOWLEDGEMENTS

I would like to express my sincerest gratitude to my supervisor, Dr. Rebecca Jamieson, for her limitless patience and support; to Dr. Mary Sanborn-Barrie and Dr. Joyia Chakungal for their continued support; to Keith Taylor for Ar-Ar data; to the Geological Survey of Canada and the Canada-Nunavut Geoscience Office for their generous support; and to the entire crew of the 2007 SIIG project for an outstanding field season.

CHAPTER 1
INTRODUCTION, TECTONIC SETTING, AND GEOLOGY OF SOUTHAMPTON ISLAND

1.1 Introduction

Southampton Island lies in a geologically cryptic area of Canada's north. Southampton Island is located in the centre of the ambiguous 'Dorset corridor' connecting Southwest Baffin Island and the western Churchill Province (Sanborn-Barrie and Berman 2007). Correlation of the magmatic, depositional, metamorphic, and metallogenic characteristics along the Dorset corridor will answer some of the major tectonic questions that limit the understanding of the Neoarchean to Paleoproterozic evolution of the area. The tectonic affinity of Southampton Island to either the Baffin-Ungava segment of the Trans-Hudson Orogen to the east or the western Churchill Province to the west is not known. This study will focus on the metamorphic characteristics of a mafic granulite sample suite from a study area on Southampton Island, in the centre of the Dorset corridor. The purpose of this study is to:

1. Document the mineralogy, mineral zoning, textures, and sequence of reactions in representative mafic granulites from the study area;
2. Integrate textural and mineral chemistry data to obtain *Pressure-Temperature* (*P-T*) estimates, corresponding to a set of metamorphic reactions;
3. Date cooling through ~500°C using $^{40}Ar/^{39}Ar$ thermochronology of hornblende;
4. Construct a *P-T-t* path and assess the tectonic evolution of the area.

This study is organised as follows. The remainder of chapter 1 presents the regional tectonic setting of Southampton Island in relation to the Baffin-Ungava segment of the Trans-Hudson Orogen (THO) to the east, and the Hearne, Rae, and Chesterfield domains of the western Churchill Province (WCP) to the west. Chapter 2 discusses the geology of the study area, from

which representative samples were collected. Chapter 3 discusses petrography, mineral chemistry, and the textural significance of selected samples from the study area. Chapter 4 discusses the methodology and results of quantitative *P-T* estimates from selected samples. Chapter 5 presents results of $^{40}Ar/^{39}Ar$ thermochronology from selected samples. Chapter 6 discusses the tectonic significance of *P-T* estimates and $^{40}Ar/^{39}Ar$ data, in context of a *P-T-t* path, and the potential correlation to parts of the THO and the WCP.

This study will complement similar studies on the petrography of meta-sediments, geochronology of selected units, geochemistry of granitoids, and structural interpretations conducted by Rob Berman, Mary Sanborn-Barrie, Joe Whalen, and Nicole Rayner at the Geological Survey of Canada in Ottawa.

1.2 Exploration History

Southampton Island is a 40,000 km^2 land mass located at the northwest end of Hudson Bay, first sighted by Thomas Button in 1613 (Fig. 1.1). Coral Harbour is the only community on Southampton Island, with a population of approximately 800 people. The most recent geological map of Southampton Island (SI) was produced in 1970 at a 1:1,000,000 scale by Heywood and Sanford. During the summer of 2007, the Geological Survey of Canada and the Canada-Nunavut Geoscience Office conducted a targeted mapping initiative to create a 1:250,000 map of the Precambrian geology. Sample collection and field work that pertains to this thesis were conducted during the summer of 2007. Geological descriptions of SI and the study area in this thesis are based on the field work conducted by members of the Southampton Island Integrated Geoscience Project. This project will ultimately integrate petrology, structural geology, geochemistry, and geochronology to produce an in-depth understanding of the tectonic evolution of SI and its setting in the THO and the WCP.

1.3 Tectonic Evolution

Southampton Island occupies a poorly understood territory, the "Dorset corridor" between the Baffin-Ungava segment of the Paleoproterozoic Trans-Hudson Orogen and the Mesoarchean-Paleoproterozoic western Churchill Province. Currently, no geochronological data are available on Southampton Island to test the affiliation to either east or west. Southampton Island may represent the western extent of the Meta-Incognita microcontinent, the south-eastern extent of the Rae domain, or neither.

1.3.1 Western Churchill Province

The western Churchill Province (WCP) represents one of the largest tracts of Archean crust in the world (van Breeman *et al.* 2007). It extends from northern Baffin Island into the Northwest Territories where it is terminated by the Thelon Orogen that separates the Archean Slave and Rae cratons (Fig. 1.1). Based on contrasting tectonometamorphic histories, the WCP has been divided by some authors into the Rae, Hearne and Chesterfield crustal blocks (Berman *et al.* 2007), although some authors do not recognise Chesterfield as a distinct crustal block (Ross *et al.* 2000; Flowers *et al.* 2006). The Rae and Chesterfield domains were tectonically juxtaposed at *ca.* 2.61-2.58 Ga followed by the accretion of the Hearne domain at *ca.* 1.9 Ga (Berman *et al.* 2007). The Meta-Incognita terrane, an allochtonous microcontinent, was accreted to the southern-edge of the eastern Rae domain at *ca.* 1.88-1.865 (St-Onge *et al.* 2007). The Hudson-protocontinent (Roksandic *et al.* 1987), a proposed microcontinent based on geophysical data, may have accreted at this time. For further details on the tectonic evolution of the WCP, consult Sanborn-Barrie *et al.* 2001, Berman *et al.* 2005, 2007, Martel *et al.* (*in press*).

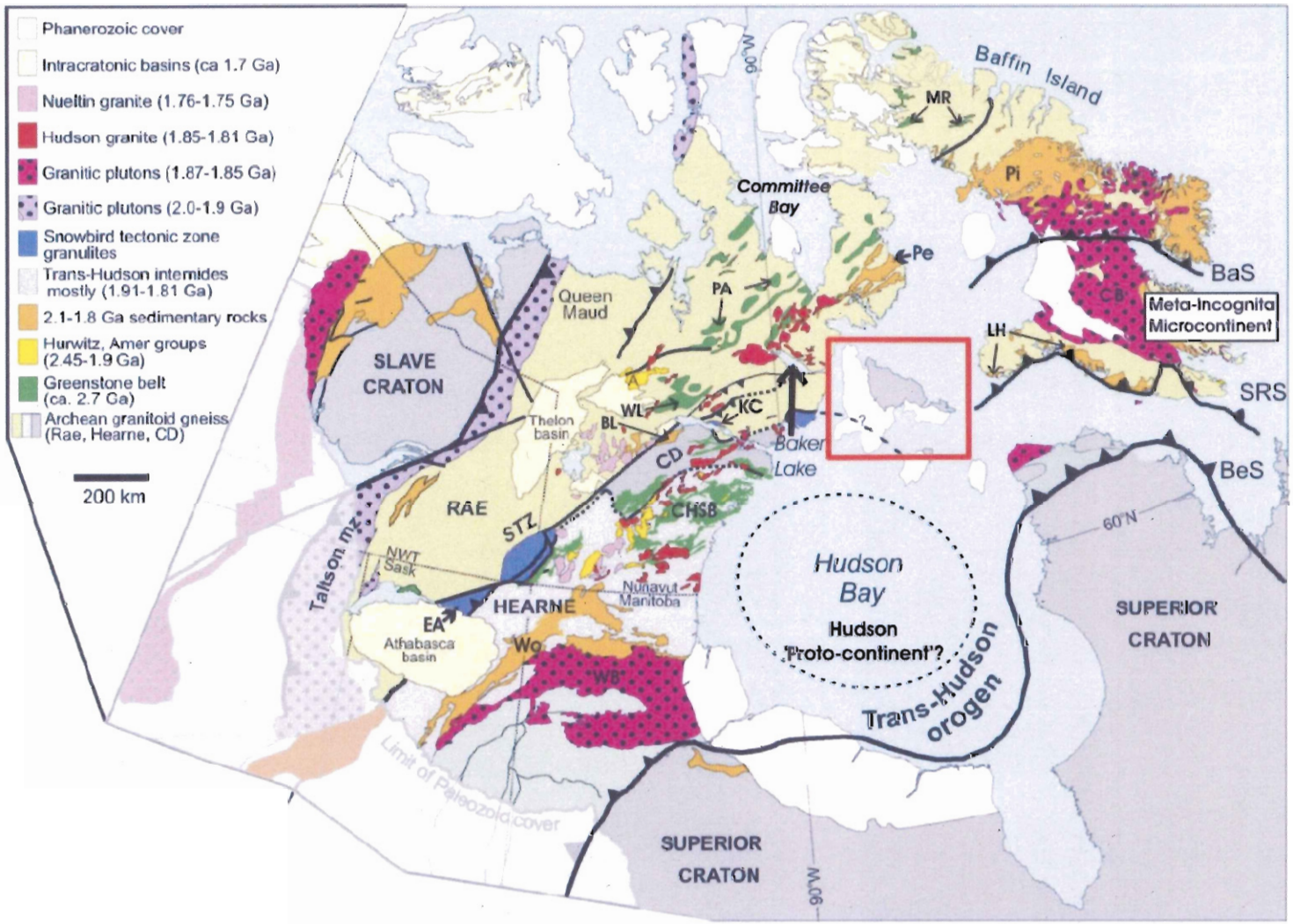

Figure 1.1 Regional geology surrounding Southampton Island after Berman *et al.* 2005, 2007; St-Onge *et al.* 2007; Martel *et al.* (*in press*). Red box shows location of Southampton Island. Abbreviations- BaS: Baffin Suture; BeS: Bergeron suture; BL: Baker Lake Group; CB: Cumberland Batholith; CD: Chesterfield domain; CHSB: Central Hearne supracrustal belt; EA: East Athabasca mylonite zone; KC: Kramanituar complex; LH: Lake Harbour Group; MR: Mary River Group; Pe: Penrhyn Group; Pi: Piling Group; SRS: Soper River suture; STZ: Snowbird tectonic zone; WB: Wathaman Batholith; WL: Woodburn Lake Group;Wo: Wollaston Group

The WCP is dominated by Archean amphibolite- to granulite-facies granitoid gneisses and laterally extensive greenstone belts, overlain by 2.45-1.75 Ga volcanic and sedimentary sequences, which are all intruded by 1.83-1.75 Ga granitoid suites.

The Rae domain is an Archean crustal block, bounded by the Snowbird Tectonic Zone (STZ) to the east and the Taltson-Thelon magmatic arc to the west. The basement of the Rae domain, the Queen Maud block, is composed of Mesoarchean granitoid gneisses. It is distinguished from the Hearne Province by the presence of a *ca.* 2.7-2.6 Ga intracontinental greenstone belt that includes komatiitic flows and fuschitic quartzite (Berman *et al.* 2007). The greenstone belts can be correlated for >1000 km from Baker Lake to northern Baffin Island (Fig. 1.1). Paleoproterozoic supracrustal units, not exclusive to the Rae domain, can be traced along strike of the STZ from the Penrhyn Group to the Piling Group of central Baffin Island. The Chesterfield block is distinguished by 2.56-2.50 Ga tectonometamorphism, believed to reflect collisional reworking of the margin (Davis *et al.* 2006).

Separating the Rae and Hearne domains is the STZ (Mahan and Williams 2005; Baldwin *et al.* 2003), a *ca.* 2800-km long medium- to high-pressure belt that has been interpreted by Berman *et al.* (2007) to be the result of a continental collision between the Hearne and composite Rae-Chesterfield blocks. Activation of the STZ was coeval with a period of microcontinent accretion that included the Hearne, Rae-Chesterfield blocks, the Meta-Incognita microcontinent and possibly the Hudson protocontinent (Berman *et al.* 2005).

The Hearne domain is composed of Mesoarchean crust intruded by mafic volcanic belts and subvolcanic tonalitic plutons. Distinguishing the Hearne domain from adjacent domains are 2.6 Ga granitic plutons. Archean greenstone belts and Paleoproterozoic supracrustal units are

present, but appear to represent a different tectonostratigraphic unit than analogous Rae-Chesterfield units (Berman *et al.* 2007).

Voluminous Paleoproterozic granitic suites are present throughout the WCP and the Baffin-Ungava segment of the THO. In the western Rae domain, the Thelon Tectonic Zone contains a 2.0-1.93 Ga calc-alkaline arc, the result of east-vergent subduction. Granitic suites thought to represent upper and lower crustal melts, emplaced at *ca.* 1.76-1.75 Ga and at *ca.* 1.83 Ga, respectively, are the products of the collision of the Superior and Churchill cratons, possibly aided by mafic underplating (Peterson *et al.* 2002). Arc-type magmatism at 1.87-1.85 Ga, the product of north-directed subduction during the Trans-Hudson orogeny, produced extensive calc-alkaline granitic plutons (Berman *et al.* 2005).

Paleoproterozoic sedimentary belts throughout the WCP are divided into an older (2.45-2.1 Ga) sequence unconformably overlain by a younger (1.95-1.91 Ga) sequence. Large intracratonic basins (1.72 Ga), such as the Athabasca and Thelon basins, are attributed to post-orogenic thermal subsidence following the termination of the Trans-Hudson Orogeny (Berman *et al.* 2005).

1.3.2 Baffin-Ungava segment of the Trans-Hudson Orogen

The Trans-Hudson Orogen is a Paleoproterozoic Himalayan-scale orogenic belt that extends from Greenland into the south-western United States (Fig. 1.1) (St-Onge *et al.* 2007). The Baffin-Ungava segment of the THO separates the Rae domain of the WCP, from the Meta-Incognita microcontinent and the Superior Province to the south, respectively. For a comprehensive review of the tectonic evolution of the Baffin-Ungava segment of the THO, the reader is directed to St-Onge *et al.* (2002, 2007).

The tectonic evolution of the Baffin-Ungava segment of the THO involved the amalgamation of the Rae and Superior provinces, the Meta-Incognita microcontinent and the Narsajuaq island-arc terrane from1880-1795 Ma. The closure of the Baffin Suture (BaS) at *ca.* 1880-1865 Ma amalgamated the Rae domain and the Meta-Incognita microcontinent (Fig. 1.1). The closure of the Soper River suture (SRS) at *ca.* 1842-1820 Ma accreted the Narsajuaq arc terrane with Meta-Incognita (Fig. 1.1). The closure of the Bergeron suture (BeS) at *ca.* 1820-1795 amalgamated the Superior craton to the composite terrane and represented the terminal collision of the THO (St-Onge *et al.* 2007).

Several meta-sedimentary units can be correlated throughout the Baffin-Ungava segment of the THO into the WCP. The Piling Group of northern Baffin Island consists of shelf, margin and foredeep strata and correlates with the Pehnyrn Group to the southwest (Martel *et al. in press*) (Fig. 1.1). The Lake Harbour Group (LH) was the cover sequence for Meta-Incognita and was involved in the collision between Meta-Incognita and the Narsajuaq island-arc terrane (St-Onge *et al.* 2007).

Like the WCP, the THO produced a series of voluminous calc-alkaline plutons associated with subduction of oceanic crust. The Cumberland Batholith was emplaced at *ca.* 1865-1848 Ma, a result of Andean-type magmatism produced by north-dipping subduction of oceanic crust beneath Meta-Incognita (St-Onge *et al.* 2007). The Wathaman Batholith in the southern Hearne domain was emplaced at similar times and is also related to arc-type magmatism (Martel *et al. in press*) (Fig. 1.1).

1.4 Geology of Southampton Island

Southampton Island is underlain by two lithological domains: the Melville Plateau of Precambrian rocks and Paleozoic limestones of the Southampton Plain (Heywood and Sanford, 1976) (Fig. 1.2).

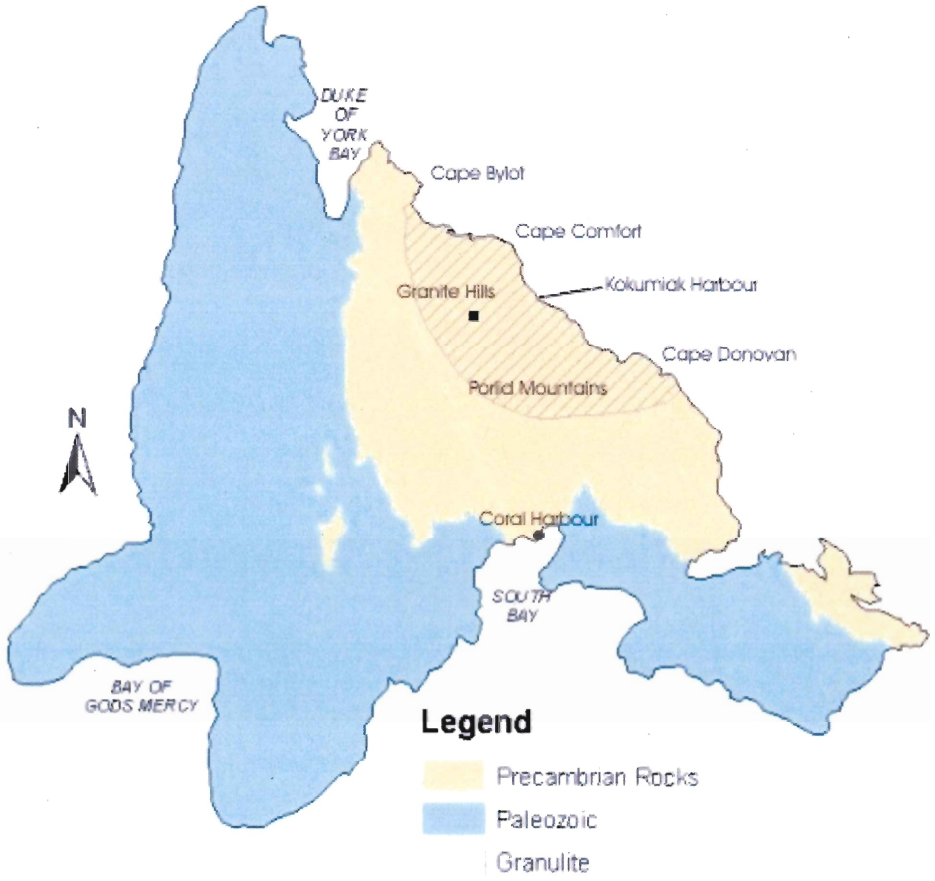

Figure 1.2. Simplified geological map of Southampton Island (after Heywood and Sanford, 1971). Black box shows location of the study area.

The Precambrian units include metasedimentary units (semi-pelites, quartzites, iron-formation and calc-silicates) intruded by a mafic-ultramafic plutonic suite. These units were intruded by several generations of pre- to syn-tectonic granitoid plutons, ranging from

monzogranite to tonalite in composition, which locally show a mineral assemblage of orthopyroxene ± biotite.

Metasediments and mafic units form metre- to kilometre-scale enclaves and rafts in several generations of the granitoids. Granulite-facies lithologies are common in the northeast of the island and are locally retrogressed to amphibolite-facies (Fig. 1.2). Amphibolite-facies units that show no evidence of retrogression from higher grades dominate the northern, western, and southern extents of the Mellevile Plateau.

Polydeformation is recorded by at least two penetrative fabrics. D_1 induced a regional foliation, defined by compositional layering and/or preferential alignment of minerals, producing a moderate- to steeply-dipping planar fabric (S_1). S_1 was pervasively folded by D_2 into tight to isoclinal recumbent F_2 folds, producing a moderately-dipping S_2 fabric. D_3 produced kilometre-scale open folding of the earlier fabrics, but produced no regionally penetrative fabrics.

CHAPTER 2
STDY AREA

2.1 Location of Study Area

The thesis study area is in the northeastern part of the Melville plateau, approximately 25 km west of Kokumiak Harbour. The study area lies between the Granite Hills to the northwest and the Porslid Mountains to the southeast at an elevation of approximately 350 m (Fig. 1.2). The study area is approximately 20 km^2 and is approximately 95% covered by Quaternary glacial tills. The study area was selected due to the high concentration of mafic and ultramafic enclaves that are found throughout northeast Southampton Island (Fig. 2.1). Field mapping and sample collection were conducted on August 11, 2007.

2.2 Geology of Study Area

The study area is dominated by voluminous Bt-Mag-monzogranite with enclaves of mafic granulites and a peridotite-garnet-anorthosite raft (Fig. 2.2). Enclaves of mafic granulite are located on opposing limbs of a west-plunging antiform in the northern limit of the study area and in the core of an east-plunging synform in the south. The peridotite-garnet-anorthosite sequence is found on the southwest-dipping limb of the antiform (Fig. 2.2).

Monzogranite is the dominant lithology in the study area and intrudes the mafic units, indicating it is the youngest lithology. Monzogranite shows a weak gneissossity (S_2), defined by biotite-rich layers alternating with biotite-poor layers. Biotite is preferentially aligned parallel to these layers. Adjacent to the study area, analogous monzogranites contains orthopyroxene surrounded by coronas of magnetite and biotite. This has been attributed to retrogression from a granulite-facies assemblage to a lower-grade assemblage. In the study area, the presence of magnetite and biotite pseudomorphing orthopyroxene in monzogranite indicates retrogression from granulite-facies conditions to lower-grade conditions.

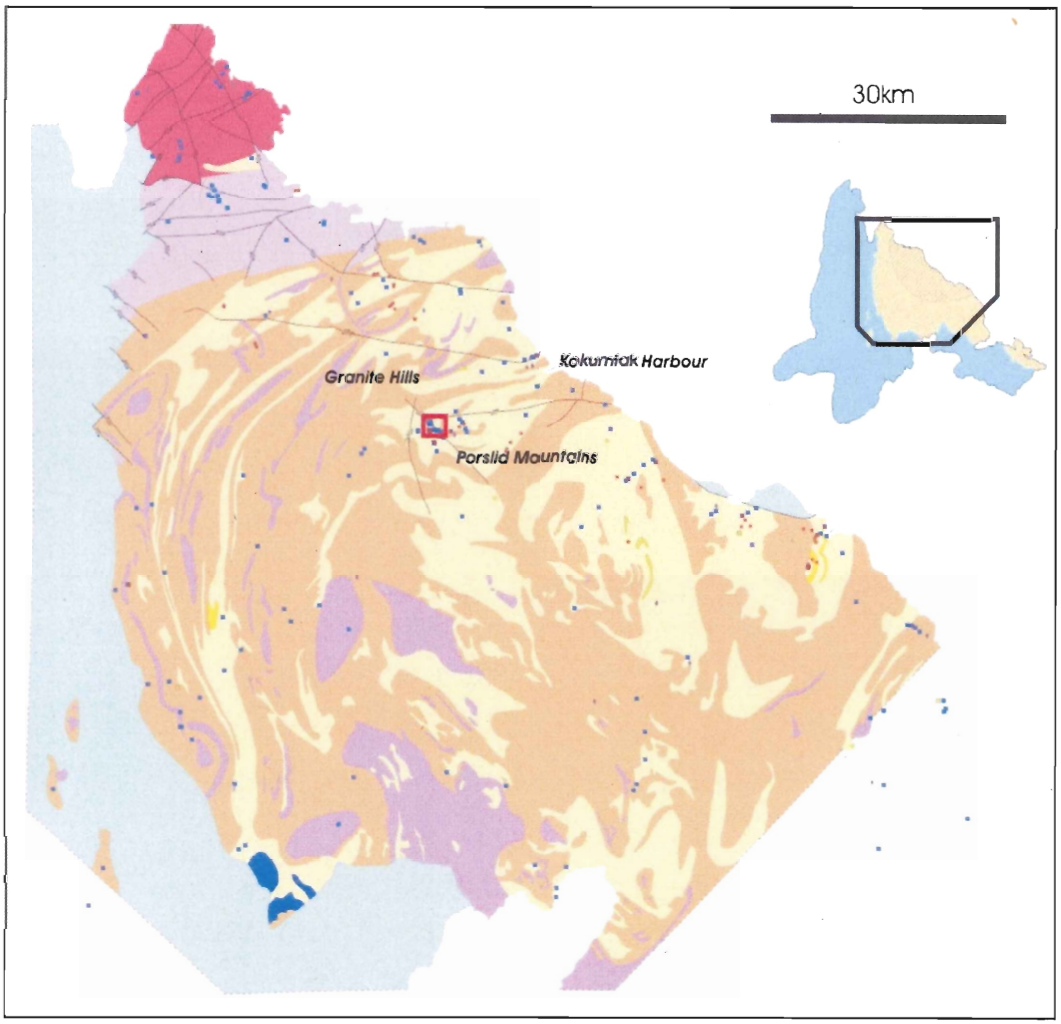

Figure 2.1. Geological map of Southampton Island. (after Sanborn-Barrie *et al.* 2008) Red box shows location of study area. Note the concentration of mafic units in the study area.

A penetrative planar fabric was used as the basis for structural measurements in Figure 2.2. This fabric correlates with the regional S_2 that is found in granitoids and metasediments throughout the island. S_2 fabrics in the study area have been folded from shallow foliations into upright, open-folds (F_3) at a scale of 10's of metres to kilometres, a feature common throughout SI. Adjacent to the study area, S_2 is defined by the axial planes of tight-to isoclinal folds (F_2) of an earlier moderate- to steeply-dipping penetrative fabric (S_1) (Fig. 2.2). This indicates that the penetrative fabric observed in the study area is S_2 and that the units were subject to at least 3 deformation events in which at least D_1 and D_2 produced penetrative fabrics.

Mafic granulites form 1-10 m enclaves within the Bt-Mag-monzogranite. The contact between units is covered by rubble and glacial debris. In other areas of Southampton Island, sharp intrusive contacts are observed between granitoids and the mafic enclaves. The mafic granulites contain cm-scale garnet porphyroblasts, surrounded by mm-scale symplectites of plagioclase and orthopyroxene. All samples are overprinted by hornblende, which replaces orthopyroxene in some hand samples.

Mafic granulite enclaves show subtle compositional layering of alternating felsic- and mafic-rich layers, which are folded into isoclinal folds parallel to S_2 in the granites (Fig. 2.3). The intrusion of monzogranite was pre- to syn-D_1 because S_1 and S_2 are parallel in both the enclaves and the monzogranite.

A 5 m thick raft of peridotite is oriented parallel to the main foliation and displays sharp contacts with the monzogranite. The raft is approximately 1 km long and shows continuous open folds, concordant with F_3 folds observed outside the study area (Fig. 2.4). The peridotite is fine-grained and equigranular, suggesting pervasive recrystallisation. No pre-F_3 fabrics were observed.

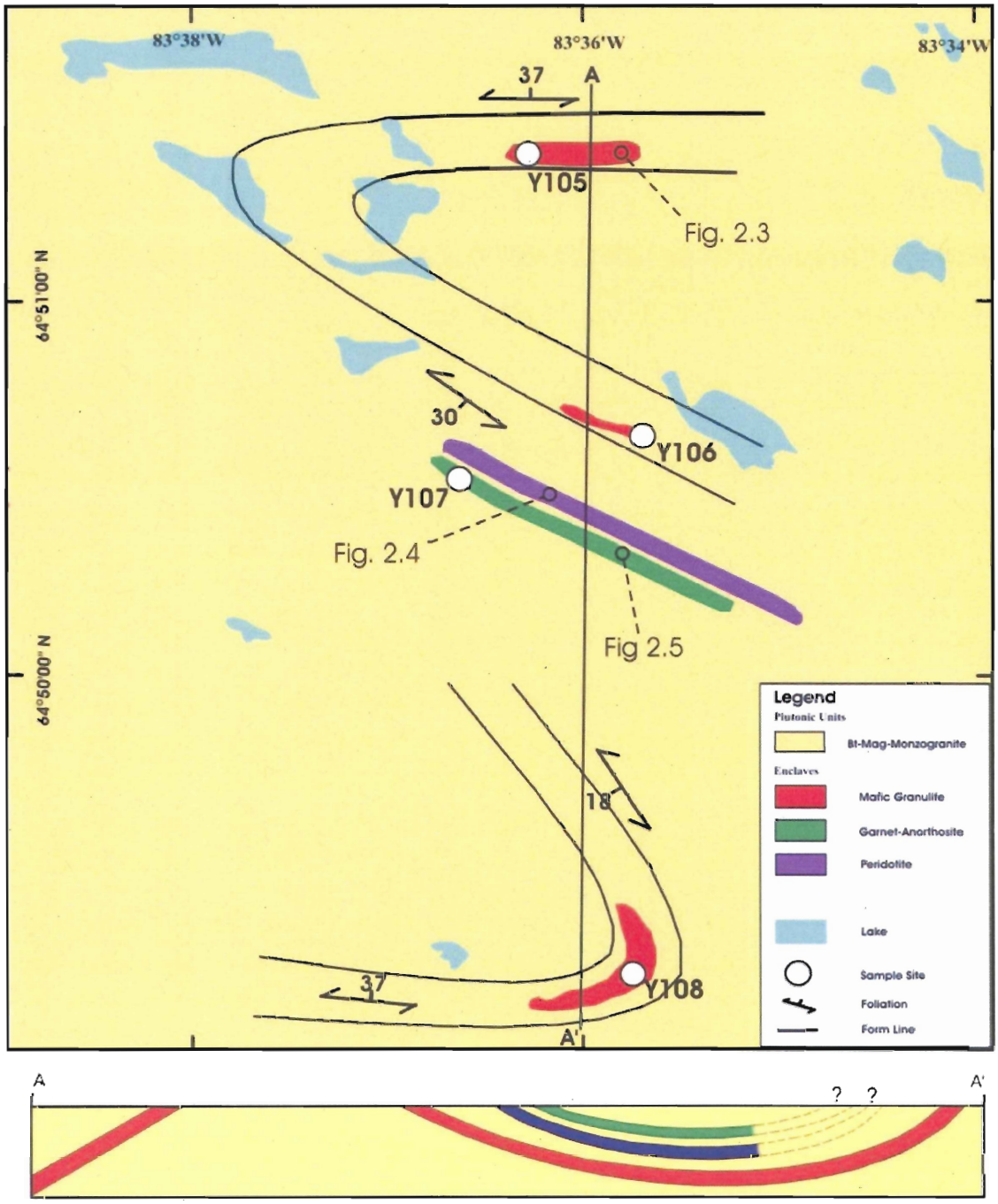

Figure 2.2 Geological map and cross-section of study area. The northern limit of the study area contains 2 enclaves of mafic granulite on opposing limbs of a west-plunging antiform. The southern limb of the antiform contains foliation-parallel rafts of garnet anorthosite and peridotite. The southern limit of the study area contains an enclave of mafic granulite in the core of an east-plunging synform.

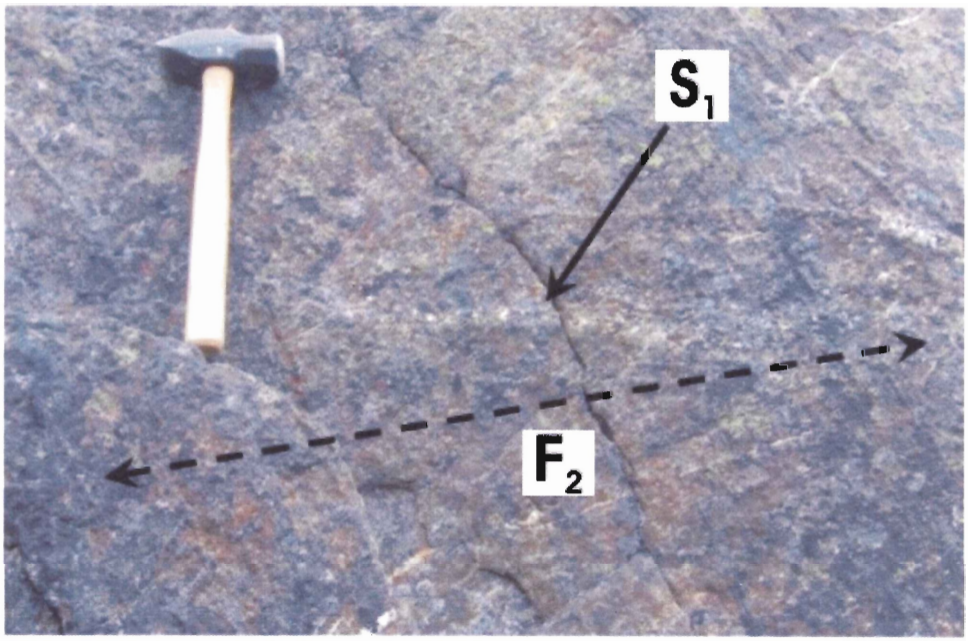

Figure 2.3. S_1 is defined by felsic layers in the mafic granulite and is folded by D_2 into F_2 folds, of which the axial plane is parallel to S_2 fabrics in the surrounding monzogranites.

A 3 m thick raft of garnet anorthosite structurally overlies the peridotite and is laterally continuous with it. The contact between the garnet anorthosite and the monzogranite is sharp. The proximity, similar orientation, and lateral continuity of the peridotite and anorthosite rafts suggest they are most likely genetically related. Garnets are up to 2 cm across and are surrounded by mm-scale symplectites of orthopyroxene and plagioclase (Fig. 2.5). Amphibole is common, but only comprises ~4% of the rock. Samples with garnet were preferentially selected for *P-T* work.

The garnet anorthosites contain a weak foliation defined by parallel alignment of amphibole. The foliation is parallel to the S_2 fabric in the surrounding monzogranites. There is no evidence of a folded S_1 fabric, indicating that the alignment and/or growth of amphibole provides a minimum age for D_1 and a maximum age for D_2.

Figure 2.4. F_3 open-fold of the peridotite layer. Structurally overlying the peridotite is a garnet anorthosite raft with the same orientation (not pictured).

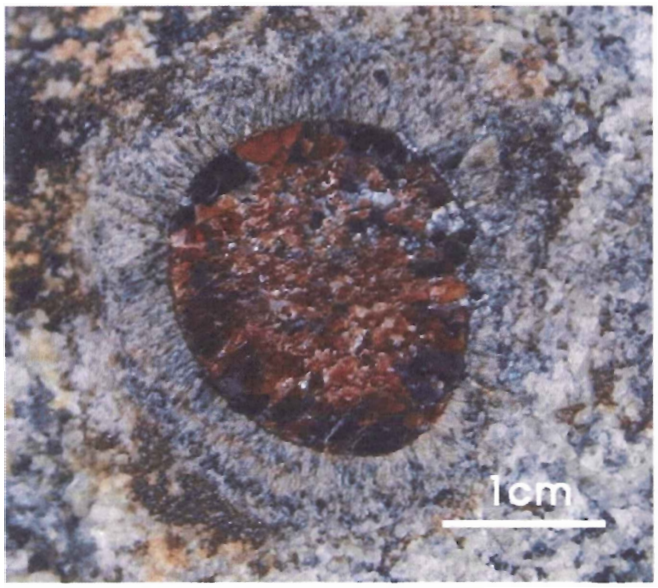

Figure 2.5. Garnet porphyroblast in garnet anorthosite with symplectite of plagioclase and orthopyroxene.

2.3 Sample Collection

Samples were collected during the summer of 2007 with the support of the Geological Survey of Canada and the Canada-Nunavut Geoscience Office. A total of 26 samples were collected from 4 localities throughout the study area representing all of the main mafic units in the area (Fig 2.2). Samples that show minimum replacement of pyroxenes by hornblende and containing orthopyroxene, clinopyroxene, and garnet were preferentially selected for *P-T* work. Samples dominated by hornblende were preferentially selected for $^{40}Ar/^{39}Ar$ analysis.

CHAPTER 3
PETROGRAPHY AND MINERAL CHEMISTRY

3.1 Introduction

Representative mafic samples from the study area were collected for petrographic and thermobarometric analysis. Garnet clinopyroxenite samples were collected from sample sites Y105 and Y108. Mafic granulite samples were collected from sample sites Y105, Y106, and Y108. Garnet anorthosites were collected from sample site Y107 (Fig. 2.2).

Petrographic analysis is essential to characterise the sequence of mineral formation in texturally heterogeneous samples. This sequence can then be used to determine several points along a *P-T* path from a single texturally heterogeneous sample (Engvik *et al.* 2007). In conjunction with reaction sequences, chemical zoning in minerals can also be used to determine multiple points along a *P-T* path.

All samples contain 3 textural domains: matrix, coronas, and inclusions in garnet. Each of these domains may contain the same mineral assemblage, but the minerals differ in composition and texture. Mineral chemistry within these domains is a product of intra-domain cation exchange and net-transfer chemical reactions.

Inclusions in garnet represent minerals that were present prior to the growth of garnet. These inclusions represent the oldest, incomplete mineral assemblages in the samples, and possible remnants of prograde metamorphism.

Monomineralic and polymineralic coronas are the result of the chemical breakdown of an unstable phase(s) into a stable phase(s), via net-transfer chemical reactions. Coronas may develop in conjunction with prograde or retrograde metamorphism. A polymineralic corona, containing vermicular intergrowths of two or more minerals, will herein be referred to as a symplectite. A summary of reaction textures from various samples is presented in Table 3.1.

Symplectites represent the terminal reaction of an unstable mineral phase(s) into a more stable mineral phase(s) during prograde or retrograde metamorphism. They are the product of rapid mineral reactions that are not facilitated by a fluid phase (Passchier and Trouw 2005). Symplecite textures are controlled by steady-state diffusion-controlled reorganisation of Si and Al into a more stable chemical structure, such as plagioclase and orthopyroxene from garnet. Coronas containing aluminous phases (eg. garnet) rely on the mobility of aluminium to be small, which most likely makes the most aluminous phase rate-controlling. Symplectites suggest that Al and Si are relatively immobile and Mg and Fe are more mobile (Grant 1988).

Matrix assemblages are either coarse- or fine-grained. Coarse-grained assemblages typically contain zoned minerals, whose rims were affected by chemical re-equilibration with surrounding phases in response to changing physical conditions (pressure, temperature, fluid activity). The cores of the large matrix minerals are less susceptible to chemical re-equilibration during retrograde ion-exchange reactions, but are chemically susceptible to exsolution of other minerals during retrogression. Fine-grained matrix assemblages are commonly chemically homogenous, reflecting near-complete chemical equilibrium with surrounding minerals.

All samples have been overprinted by an amphibolite-facies assemblage from a granulite-facies assemblage, indicated by the replacement of pyroxenes by hornblende. Most hornblende is brown, which is typical of upper-amphibolite grade assemblages. Rare blue-green hornblende and biotite in the mafic granulite samples, replaced pyroxenes and hornblende, suggest retrogression toward lower amphibolite-facies conditions.

Apatite, magnetite and ilmenite are accessory phases found in all three textural domains in all samples. Apatite forms euhedral, <0.1 mm grains that are common as inclusions in garnet and less common in coronas and the matrix. Anhedral magnetite, up to 1 mm in size, is always

associated with symplectites in anorthosite samples, and typically associated with symplectites in mafic granulite and garnet clinopyroxenite samples. Ilmenite forms anhedral <0.5mm grains that are typically associated with symplectites.

There is no evidence of penetrative fabrics in the mafic granulites or garnet clinopyroxenites. Garnet anorthosites have a weak foliation defined by the preferential alignment of the long axes of hornblende. Symplectites are always symmetrical and display no evidence of deformation.

Chemical analyses of minerals were obtained through electron microprobe (EMP) analysis at the R.M. MacKay Electron Microprobe Laboratory, Dalhousie University, Halifax. All mineral analyses for which data are displayed and/or discussed and the EMP analytical parameters are presented in Appendix 1. All mineral abbreviations are from Kretz (1983).

Table 3.1 Summary of reaction textures in various sample types

Reaction Texture	Type-I Corona	Type-II Symplectite	Type-III Symplectite
Reactants	Grt + Cpx	Grt + Opx_2	Grt +$Plag_1$
Products	Opx_2	Opx_3 + $Plag_2$	Opx_3 + $Plag_2$ + Mag
Reaction (unbalanced)	Grt + Cpx → Opx_2	Grt + Opx_2 + Qtz→ Opx_3 + $Plag_2$	Grt + $Plag_1$ + O_2 → Opx_3 + $Plag_2$ + Mag
Lithologies	All	All	Anorthosite only

3.2 Mafic Granulites

3.2.1 Matrix

The matrix of the mafic granulites is composed of plagioclase + clinopyroxene + orthopyroxene + pargasite ± magnetite ± apatite ± ilmenite (Fig. 3.1a). The matrix is typically fine-grained and is always isolated from garnet by intervening Type-I and Type-II coronas.

Plagioclase is 1-3 mm across and has an average composition of An_{58} (Fig. 3.3a). Plagioclase is rarely zoned, with anorthite content increasing from core (An_{59}) to rim (An_{78}). This suggests the activity of calcium was greater during the re-equilibration of the rim, which may have been associated with the breakdown of the grossular component of garnet.

Clinopyroxene is subhedral, up to 10 mm in size, and shows prominent exsolution lamellae of orthopyroxene with abundant intergrown ilmenite blades along cleavage planes. Titanium is relatively immobile during ion-exchange reactions, indicating that primary clinopyroxene was relatively Ti-rich. Average clinopyroxene compositions are Di_{76} with little sodium occupying the M1 site (Na approximately 0.04 atoms per formula unit (*apfu*)). The low jadeite component of the clinopyroxene indicates that this is not an eclogite-facies assemblage.

Orthopyroxene is up to 0.5 mm in size, has an average composition of Fs_{35} and is extensively replaced by brown-green hornblende. Matrix orthopyroxene is less aluminous and slightly more Fe-rich than coronitic orthopyroxene and orthopyroxene inclusions in garnet. This most likely reflects pressure-dependent Al-partitioning between orthopyroxene and garnet during decompression.

Matrix orthopyroxene (orthopyroxene-1) and clinopyroxene are extensively replaced by pargasitic hornblende. This pargasite shows relatively elevated Ca, Fe, and Si but relative depletion of Al with respect to pargasite replacing coronitic pyroxene (Table 3.2). The difference

in composition of pargasite in separate textural domains reflects different pyroxene compositions in these domains. Pargasite in the matrix is restricted to sub-domains rich in orthopyroxene.

3.2.2 Coronas

Garnet is always isolated from the matrix by Type-I and Type-II coronas. Type-I coronas separate Type-II coronas from coarse-grained clinopyroxene (Fig. 3.1b), and are composed of fine-grained aggregates of second-generation orthopyroxene (orthopyroxene-2) with an average composition of Fs_{32} and 0.13 Al *apfu* (Fig. 3.2a).

Type-II symplectites isolate garnet from all other phases and contain fine-grained vermicular intergrowths of second generation plagioclase (plagioclase-2), with an average composition of An_{93} (Figure 3.3a) and third generation orthopyroxene (orthopyroxene-3), with an average composition of Fs_{32} (Fig. 3.2a).

Type-II symplectites commonly contain green spinel and magnetite (Fig. 3.1b). Spinel has an average composition Hc_{67} and is always associated with relatively aluminous orthopyroxene-3 with an average composition of Fs_{33} and 0.15 Al *cpfu*.

Magnetite is interpreted to have formed during periods of minor oxidation of the pyroxenes during garnet-breakdown (Thost *et al.* 1991), via the reaction:

$$Grt + Cpx + Qtz + O_2 \rightarrow Opx + Plag + Mag \quad (3.1)$$

Pargasite partially to completely replaced all three generations of orthopyroxene in the matrix and in coronas. Pargasite replacing orthopyroxene-2 and orthopyroxene-3 is relatively depleted in Ca compared to pargasite which replaced matrix pyroxenes, attributed to the lack of clinopyroxene in the simplified reaction:

$$Opx_{2\ or\ 3} + H_2O \rightarrow Prg \quad (3.2)$$

Table 3.2 Representative Amphibole Compositions

Lithology	Textural Association	Structural Formula
		Pargasite $(K, Na)_{0-1}(Ca, Na)_2(Mg, Fe^{2+}, Al, Ti)_5(Si, Al)_8(OH)_2$ After Deer *et al.* 1996
Garnet clinopyroxenite	Matrix	$(K_{0.14}, Na_{0.72})(Ca_{1.95}, Na_{0.05})(Mg_{2.93,} Fe^{2+}_{1.53}, Al_{0.43}, Ti_{0.18})(Si_{6.12}, Al_{1.88})O_{22}(OH)_2$
	Replaced Opx_2	$(K_{0.21}, Na_{0.61})(Ca_{1.90}, Na_{0.10})(Mg_{2.60,} Fe^{2+}_{1.65}, Al_{0.63}, Ti_{0.20})(Si_{5.98}, Al_{2.02})O_{22}(OH)_2$
	Replaced Opx_3	$(K_{0.22}, Na_{0.61})(Ca_{1.94}, Na_{0.06})(Mg_{2.59,} Fe^{2+}_{1.62}, Al_{0.60}, Ti_{0.23})(Si_{6.05}, Al_{1.95})O_{22}(OH)_2$
Garnet anorthosite	Surrounded by matrix Opx	$(K_{0.26}, Na_{0.39})(Ca_{1.90}, Na_{0.10})(Mg_{2.75}, Fe^{2+}_{1.79}, Al_{0.47}, Ti_{0.14})(Si_{6.40}, Al_{1.60})O_{22}(OH)_2$
	Replaced matrix Opx	$(K_{0.30}, Na_{0.45})(Ca_{1.91}, Na_{0.09})(Mg_{2.60}, Fe^{2+}_{1.79}, Al_{0.44}, Ti_{0.23})(Si_{6.28}, Al_{1.72})O_{22}(OH)_2$
Mafic granulite	Replaced Opx_1	$(K_{0.18}, Na_{0.61})(Ca_{1.87}, Na_{0.13})(Mg_{2.76}, Fe^{2+}_{1.55}, Al_{0.65}, Ti_{0.19})(Si_{5.98}, Al_{2.02})O_{22}(OH)_2$
	Replaced Opx_2 + Plag	$(K_{0.16}, Na_{0.57})(Ca_{1.83}, Na_{0.17})(Mg_{2.84}, Fe^{2+}_{1.50}, Al_{0.72}, Ti_{0.14})(Si_{5.96}, Al_{2.04})O_{22}(OH)_2$
	Matrix	$(K_{0.26}, Na_{0.55})(Ca_{1.96}, Na_{0.04})(Mg_{2.50}, Fe^{2+}_{1.94}, Al_{0.40}, Ti_{0.24})(Si_{6.17}, Al_{1.83})O_{22}(OH)_2$

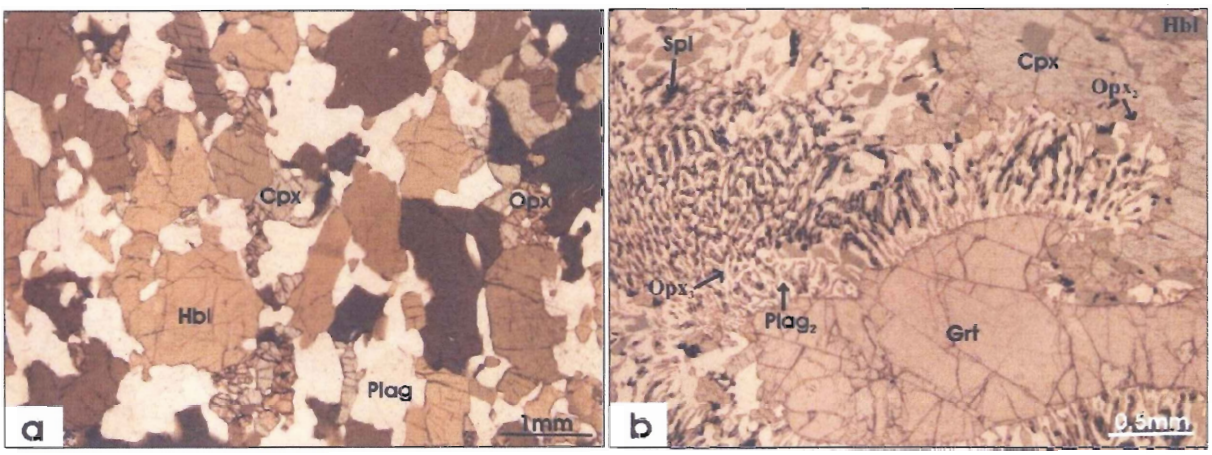

Figure 3.1 Representative textures and mineral assemblages from mafic granulites. (a) Matrix assemblage of plagioclase + orthopyroxene + clinopyroxene with replacement of pyroxenes by pargasite (Sample Y108A). (b) Type-I corona of Opx_2 between Cpx and Grt, Type-II symplectite of Opx_3 + Plag + Mag and spinel intergrowths with Opx_3 (Sample Y105C).

The mineral assemblage surrounding garnet and the associated symplectite has a profound effect on mineral chemistry. Aluminium is preferentially enriched in symplectite plagioclase proximal to matrix plagioclase and relatively depleted in symplectite plagioclase adjacent to matrix pargasite (Fig. 3.4). Nakano *et al.* (2004) suggested that plagioclase-orthopyroxene symplectites result from the isochemical breakdown of garnet. The depletion and enrichment of aluminium in the symplectites indicates an exchange of components between garnet and the surrounding minerals, indicative of an open chemical system on a limited diffusion-length scale. This suggests the breakdown of garnet in sample Y105B was not isochemical or that extensive chemical diffusion during retrogression has altered the chemistry of the surrounding minerals. Extensive chemical diffusion during retrogression seems unlikely as garnet breakdown is a terminal reaction.

3.2.3 Inclusions

Inclusions in garnet are rare, up to 1 mm in size, and are composed of quartz + plagioclase (An_{93}) ± orthopyroxene (Fs_{31}) ± apatite. Plagioclase is always associated with orthopyroxene and typically isolates orthopyroxene from garnet.

Garnet shows slight zoning with almandine increasing from core (Alm_{47}) to rim (Alm_{49}). Garnet rims show patchy zones of Ca-enrichment, with the grossular component varying from Grs_{13} to Grs_{15} (Fig. 3.4). Manganese enrichment of the rim shows the spessartine component increasing from core (Sps_2) to rim (Sps_4). The chemical zoning in garnet is most likely the result of preferential retention of Mn and Fe and the preferential donation of Ca and Mg. Garnet preferentially retains Mn because the partitioning coefficient of Mn between garnet and the matrix is normally much greater than 1 ($_{Mn}K_D >> 1$) (Spear 1995).

3.3 Garnet Clinopyroxenites

3.3.1 Matrix

Garnet clinopyroxenites contain a matrix assemblage of clinopyroxene + garnet + plagioclase (Fig. 3.6d). This mineral assemblage is typical of the high-pressure granulite-facies (O'Brien and Rötzler 2003).

Matrix plagioclase is up to 1 mm in size and is restricted to domains of several grains, commonly surrounded by clinopyroxene. Plagioclase in the matrix has an average composition of An_{58} in the core and An_{78} at the rims (Fig. 3.3a).

Clinopyroxene is xenoblastic, up to 10 mm in size, and is the most abundant mineral in the samples. Matrix clinopyroxene commonly contains exsolution lamellae of orthopyroxene and

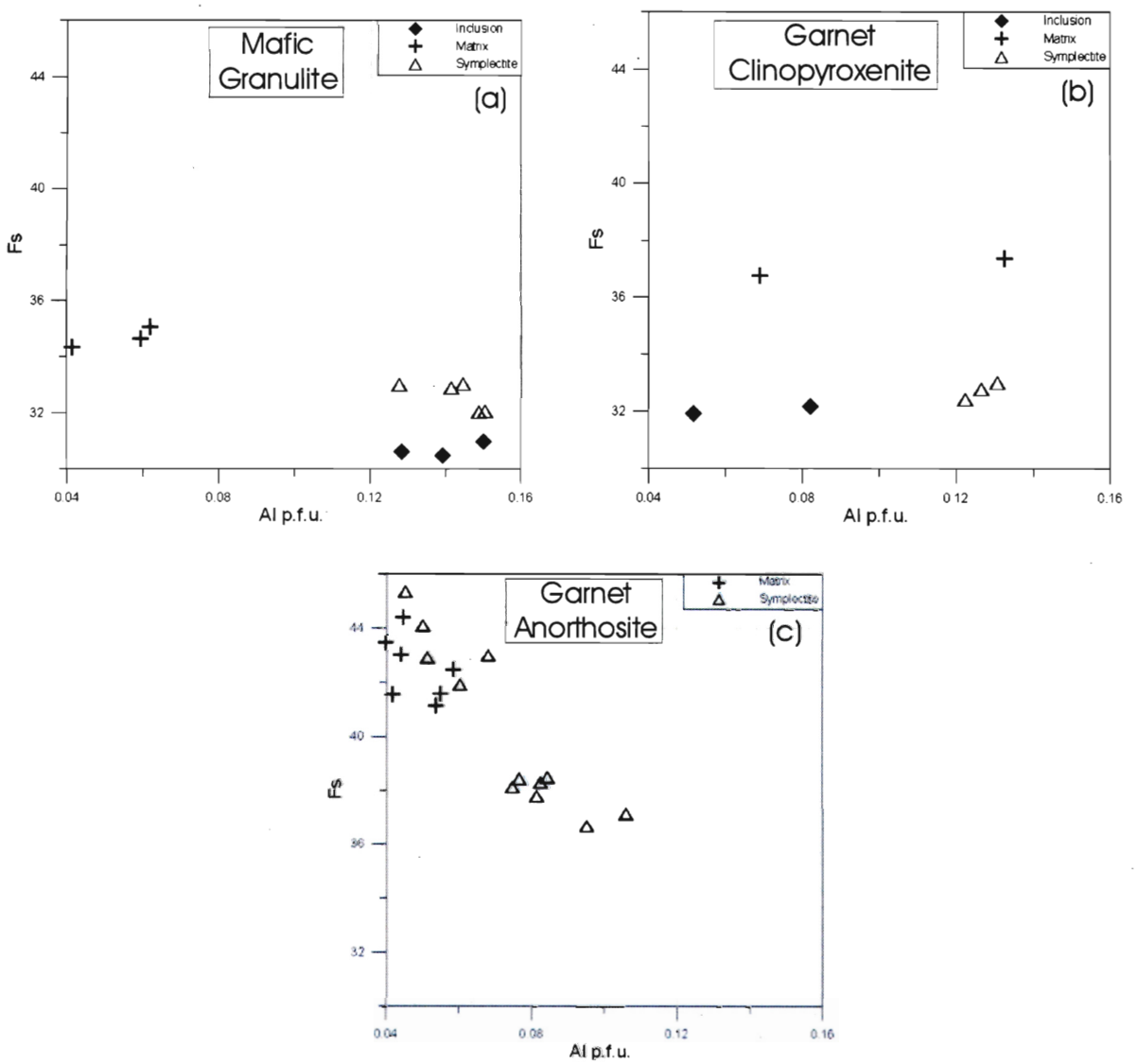

Figure 3.2 Orthopyroxene compositions from representative samples: (a) Mafic granulite; matrix orthopyroxene shows relatively enrichment of Fe and depletion of Al with respect to coronitic orthopyroxene and inclusions of orthopyroxenes in garnet, reflecting the chemical influence of adjacent garnet. (b) Garnet clinopyroxenite; elevated Al in symplectite associated with garnet dissolution and elevated Fe in matrix associated with chemistry of clinopyroxenes. (c) Garnet anorthosite; elevated Al in symplectite associated with garnet and symplectite orthopyroxene approaches matrix orthopyroxene compositions, possibly indicating an Al-rich bulk composition.

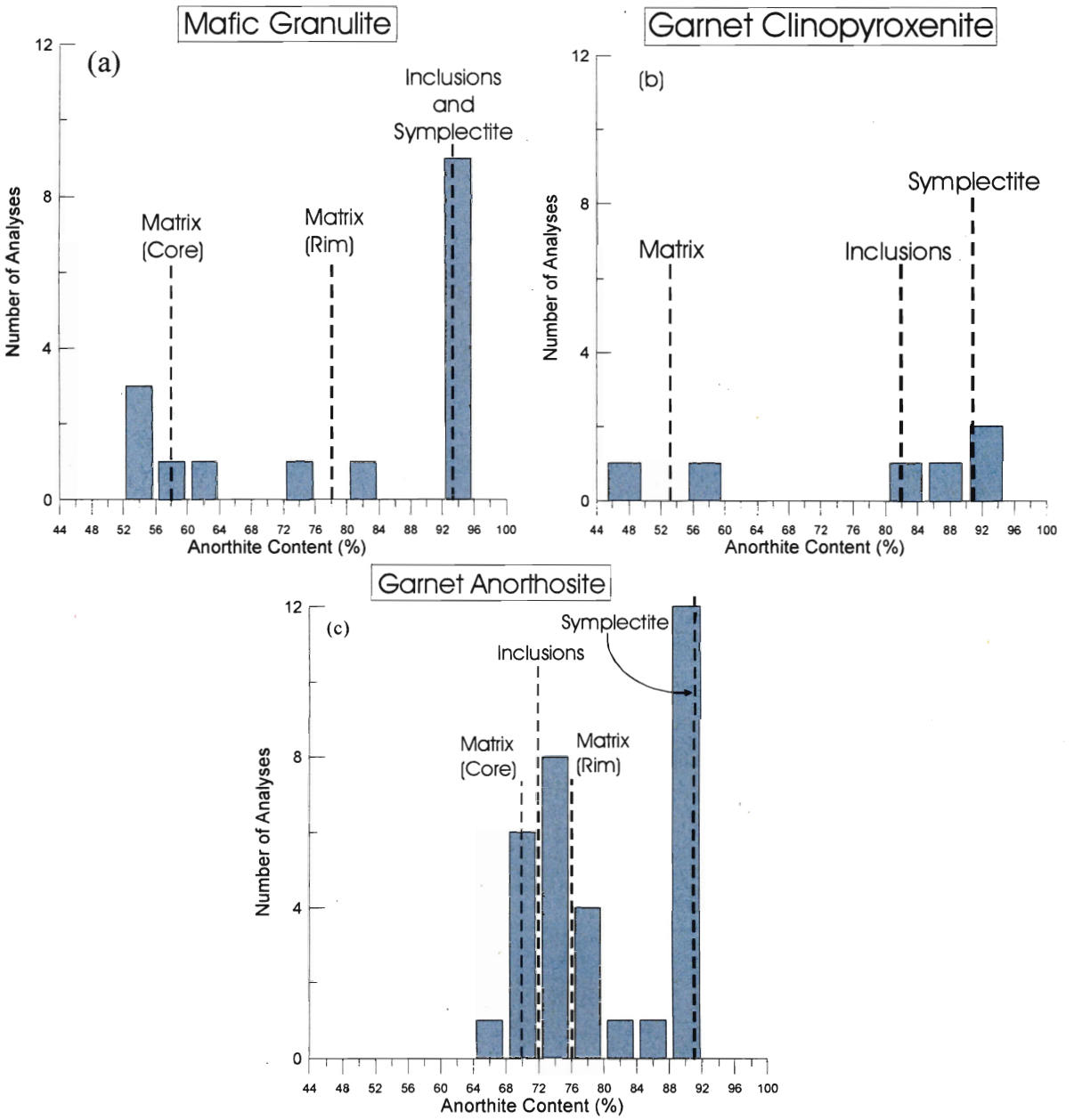

Figure 3.3 Plagioclase compositions in: (a) Mafic granulite; (b) Garnet clinopyroxenite; (c) Garnet anorthosite. Trimodal distribution in (a) of inclusions, matrix, and symplectite plagioclase. Bimodal distribution of calcic symplectite plagioclase and inclusions of plagioclase, note the lack of analyses that fall into the 'matrix' category. Bimodal distribution in (c) represents matrix plagioclase and higher-Ca symplectite plagioclase.

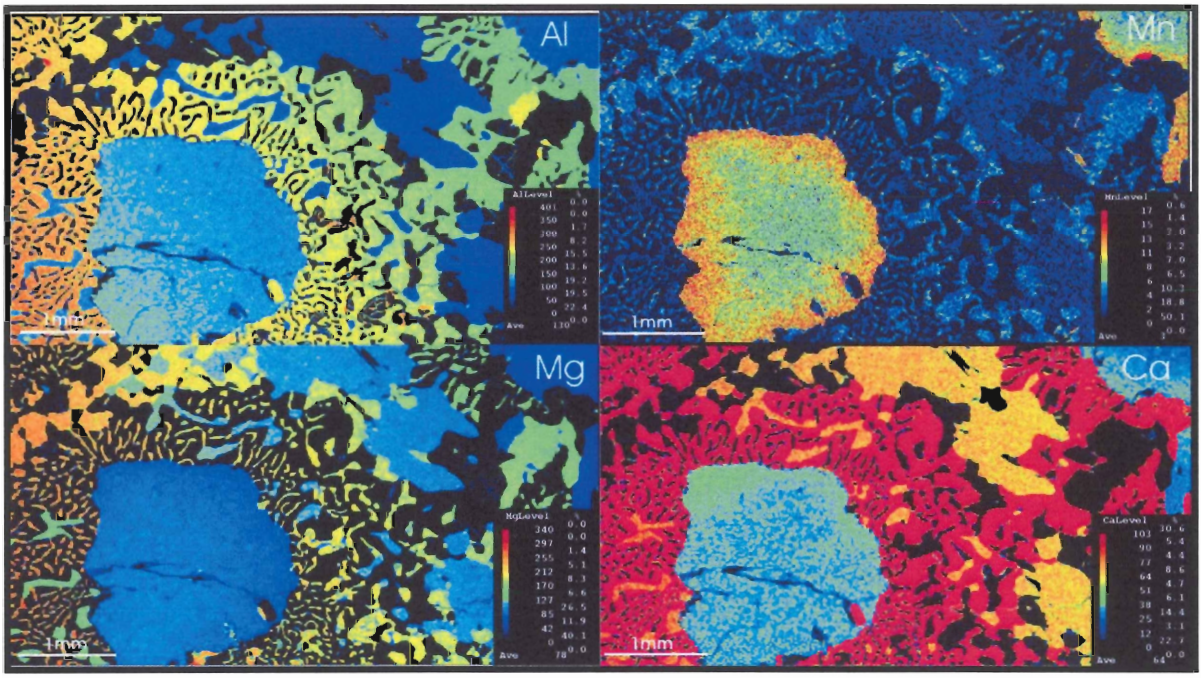

Figure 3.4. Elemental X-ray maps of garnet from sample Y105B showing enrichment of Mn from core to rim and patchy Ca enrichment around the perimeter of the garnet. Al and Mg in the symplectite are preferentially distributed on the side away from the clinopyroxene. Colour scale indicates number of counts obtained from each pixel, with red being the largest and dark blue being the smallest.

ilmenite blades along cleavage planes. This suggests that the clinopyroxene was relatively Ti-rich prior to ilmenite exsolution, which in conjunction with the lack of quartz, may suggest an alkaline protolith. Some clinopyroxene shows deformation of cleavage planes around garnet, indicating deformation at high temperatures (Figure 3.6c). Symplectites are symmetrical (post-S_1?), indicating the deformation of clinopyroxene pre-dated symplectite formation.

Garnets are typically xenomorphic, up to 15 mm in size (Fig. 3.6a), and always surrounded by Type-II symplectites (Fig. 3.6b). Symplectites that commonly completely replace garnet are typically < 2 mm in size, indicating relatively smaller garnets were more susceptible to dissolution. The susceptibility of garnet to dissolution is related to the diffusivity of particular elements.

The diffusivity of elements in minerals is dependent on: 1) chemical diffusivities between phases, 2) chemical gradients in the crystals, 3) the rate of cooling, and 4) the size of the crystal (Spear 1995). Using the simplified model developed by Cygan and Lasaga (1985), the diffusivity of Mg in garnet in their samples can be calculated from the following equations:

$$D = 6.5 \times 10^{-9} (m^2/s) \exp(-516{,}300 / RT) \quad (3.3)$$

D = chemical diffusivity
R = gas constant (8.3144 J / mol·K)
T = temperature (°K)

$$t = h^2 / D \quad (3.4)$$

t = time
h = distance of diffusion

These equations can be combined to estimate the amount of time it will take for a garnet with a given radius to chemically homogenize through volume diffusion at a given temperature (Fig. 3.5). In this study garnets with a radius >500μm were used for *P-T* estimates in order to minimize the effects of chemical re-homogenization during retrogression.

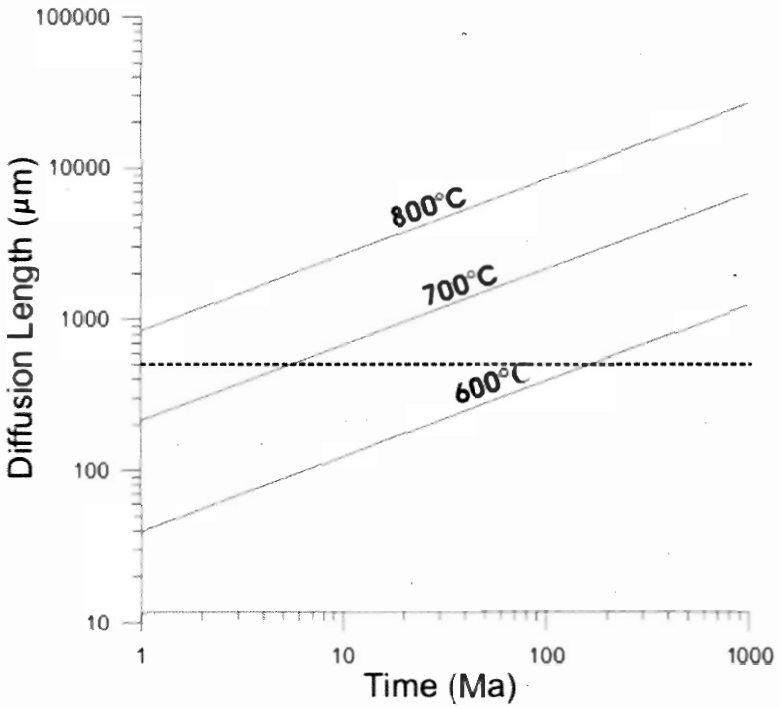

Figure 3.5. Simplified model of magnesium self-diffusion in garnet based on equations 3.3 and 3.4 after Cygan and Lasaga (1985). Dotted line represents minimum radius of garnets analyzed for representative compositions in this study. The size of the garnet has a strong effect on the time it takes for chemical homogenization through diffusion. At temperatures >800°C, even large (>1 mm radius) will homogenize in a short period of time.

3.3.2 Coronas

Garnet is always separated from matrix assemblages by Type-I and Type-II coronas (Fig 3.6d). Orthopyroxene-2 has an average composition of Fs_{37} and contains rare inclusions of plagioclase (An_{85}). Inclusions of plagioclase in orthopyroxene-2 are compositionally similar to plagioclase inclusions in garnet, indicating these grains may have once been inclusions in garnet or are the same generation.

Orthopyroxene-3 has an average composition of Fs_{41} and plagioclase-2 has an average composition of An_{91}. Aluminous orthopyroxene-3 is commonly intergrown with green spinel (Fig. 3.6b), having an average composition of Spl_{31}. Spinel and orthopyroxene in the same

assemblage are common in relatively high-temperature granulites during decompression (Elevold *et al.* 2003).

3.3.3 Inclusions

Garnets contain inclusions of plagioclase + quartz ± clinopyroxene ± orthopyroxene + apatite. Inclusions of plagioclase have an average composition of An_{82} with a slight increase in calcium from core to rim. Inclusions of clinopyroxene have a composition of Di_{72}, and always contain exsolution lamellae of orthopyroxene (Fs_{48}), indicative of chemical and textural disequilibrium.

Garnet shows a slight decrease in pyrope and increase in grossular and spessartine from core ($Alm_{49}Prp_{32}Grs_{16}Sps_3$) to rim ($Alm_{49}Prp_{29}Grs_{18}Sps_4$) (Figure 3.7). The core composition is interpreted to represent near-peak metamorphic conditions and the rim composition is interpreted to have re-equilibrated with the adjacent symplectite during garnet dissolution.

3.4 Garnet Anorthosites

3.4.1 Matrix

Garnet anorthosites contain a fine-grained matrix assemblage of plagioclase + clinopyroxene + orthopyroxene + pargasite (Fig. 3.8a). Garnet is always isolated from the matrix assemblage by Type-III symplectites.

Matrix plagioclase is typically subhedral, fine- to medium-grained, and shows subtle zoning with calcium increasing from core (An_{70}) to rim (An_{76}). The core is interpreted to represent peak *P-T* chemistry and the rims the result of re-equilibration with surrounding minerals. The rim-ward increase in Ca may be associated with the breakdown of the grossular component of garnet.

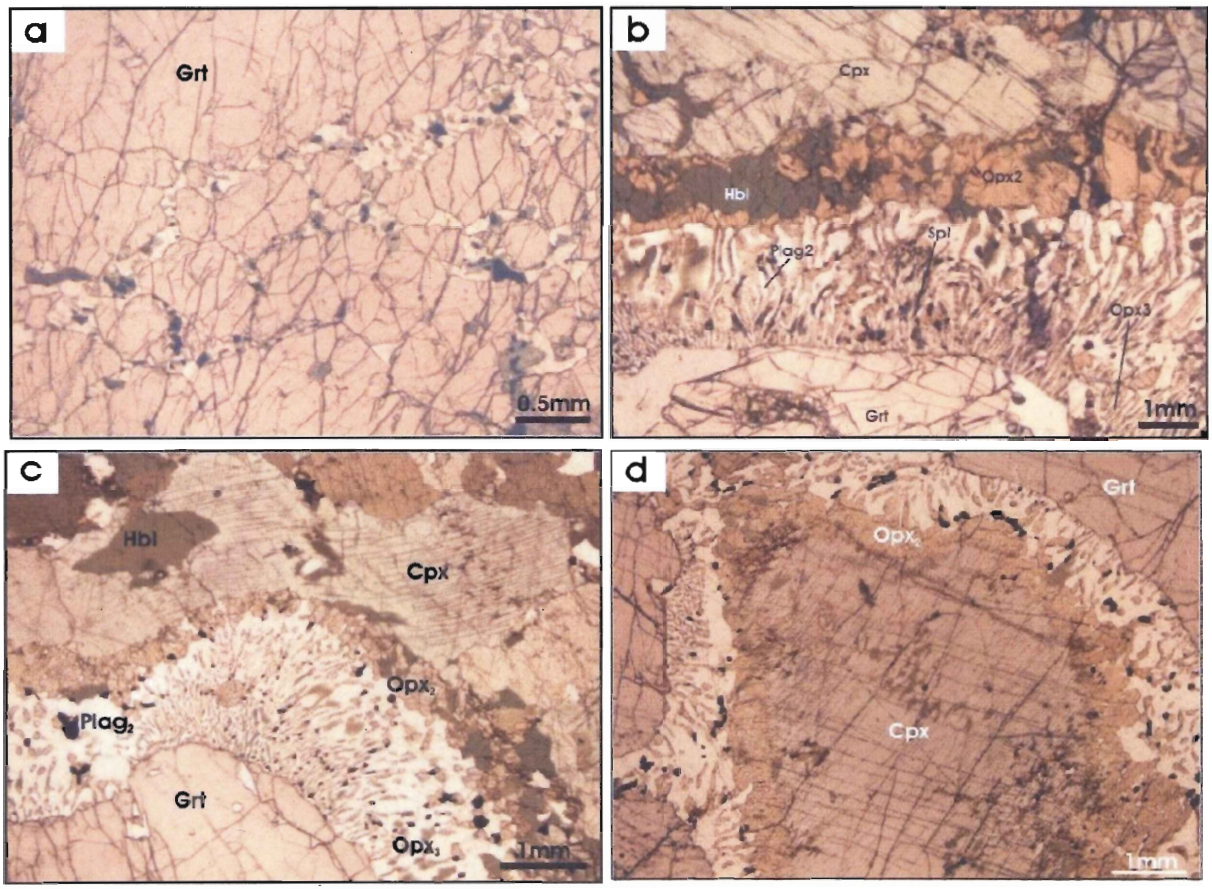

Figure 3.6 Representative textures and mineral assemblages of garnet-pyroxenites. (a) Aggregate texture of garnet (Sample Y105D). (b) Coarse grained Cpx and Grt separated by Type-I and Type-III coronas. Pargasite preferentially replaced Opx (Sample Y108D). (c) Deformed Cpx around garnet with intervening Type-I and Type-II coronas (Y105D). (d) Large Cpx isolated from garnet on all sides by Type-I and Type-II symplectites (Y105D).

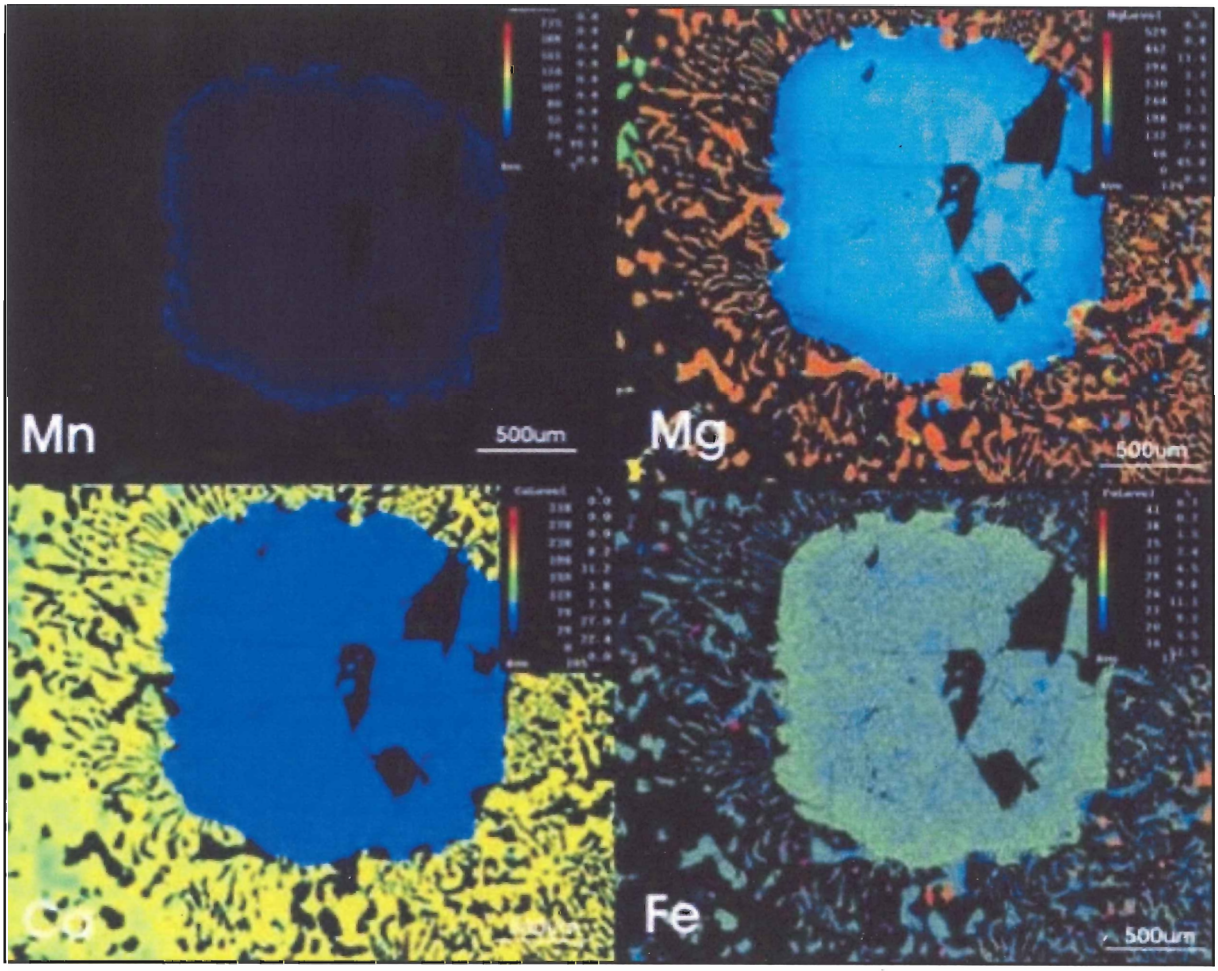

Figure 3.7. Elemental X-ray maps of garnet in garnet pyroxenite. Fe and Mn increase from core to rim and Mg decreases from core to rim. Symplectite orthopyroxene has a higher concentration of Mg than that of the garnet and a similar concentration of Fe to the garnet rim. Mn is preferentially retained in the rim of the garnet in a zone approximately 100 μm wide. Colour scale indicates number of counts obtained from each pixel, with red being the largest and dark blue being the smallest (Sample Y108C).

Clinopyroxene is fine-grained, subhedral and has an average composition of Di_{72}. Orthopyroxene is fine-grained, subhedral and has an average composition of Fs_{42}. Clinopyroxene and orthopyroxene are evenly dispersed throughout the matrix and are commonly isolated within matrix plagioclase.

Layers rich in pargasitic hornblende define a weak S_2 fabric that is parallel to S_2 in the monzogranites in the study area (Fig. 3.8e). Biotite is rare, replaces hornblende, and is preferentially aligned with the S_2 fabric (Fig. 3.8e).

3.4.2 Coronas

Garnet anorthosites contain Type-I, Type-II and Type-III coronas (Fig 3.8b,c). Most garnets have a well developed Type-III symplectite, separating garnet from matrix plagioclase (Fig. 3.8b). Type-II symplectites have partially to totally replaced garnet (Fig. 3.8c,d). Type-III symplectites contain vermicular plagioclase and orthopyroxene grains, separated from the matrix by a nearly continuous corona of magnetite and lesser amounts of ilmenite, indicating the reaction:

$$Grt + Qtz + O_2 \rightarrow Opx_3 + Plag_2 + Mag \quad (3.3)$$

Orthopyroxene-3 and plagioclase-2 show a change in chemical composition from garnet to the matrix. Orthopyroxene becomes coarser and more Fe-rich away from the garnet with Fs changing from 0.37 to 0.45 (Figure 3.9). Plagioclase becomes less calcic towards the matrix with compositions increasing from An_{94} to An_{84}. This compositional variation is attributed to the influence of the chemistry of adjacent minerals, with more sodic plagioclase reflecting proximity to clinopyroxene (0.03-0.04 *cpfu* Na) and Mg-rich orthopyroxene representing proximity to garnet.

3.4.3 Inclusions

Inclusions in garnet contain the assemblage Qtz + Plag ± Ap ± Py ± Ccp. Plagioclase commonly shows an increase in calcium from core (An_{71}) to rim (An_{90}). Unzoned plagioclase inclusions range in composition from An_{65-76}. The average composition of plagioclase as inclusions in garnet is An_{72}.

Garnet shows increasing Pyr and Grs and decreasing Alm from core ($Alm_{58}Prp_{20}Grs_{18}Sps_4$) to rim ($Alm_{50}Prp_{22}Grs_{26}Sps_2$) (Figure 3.10). Manganese enrichment in the rim is the product of preferential retention during garnet dissolution. A slight increase in Mg towards the rim is accompanied by a slight decrease in Fe towards the rim. This may be the product of Fe-Mg exchange between garnet and orthopyroxene-3 during garnet dissolution or Mn substituting for Fe.

3.4 Discussion

All samples in this study display characteristic peak granulite-facies mineral assemblages with retrogression to amphibolite-facies assemblages. This is consistent with the surrounding monzogranites that show retrogression from granulite-facies mineral assemblages (orthopyroxene) to lower-grade assemblages (biotite + magnetite). Several generations of orthopyroxene and plagioclase are present as mono- and polymineralic coronas, as inclusions in garnet, and as matrix minerals. Garnet clinopyroxenites have a characteristic high-pressure granulite-facies mineral assemblage, defined by the absence of orthopyroxene from the peak assemblage. Mafic granulites and garnet anorthosites contain a mid-pressure granulite-facies assemblage, characterised by the presence of orthopyroxene in the peak assemblage. Garnets in every sample are surrounded by symplectites of orthopyroxene + plagioclase ± spinel ± magnetite, indicative of near- isothermal decompression reactions (Engvik *et al.* 2007).

The lack of matrix quartz suggests that all three lithologies are relatively silica-undersaturated. Development of Opx + Plag symplectites in the absence of quartz has been attributed, by some authors, to result from infiltration of fluid or melt from adjacent felsic gneisses, which increased the activity of silica (Harley 1988, 1989; Thost *et al.* 1991). Monzogranites in the study area contain minor leucosome (<5%), which may have increased the activity of silica, which facilitated the dissolution of garnet.

The three textural domains discussed in this chapter correspond to three stages of mineral growth and re-equilibration. Stage 1 is represented by the peak metamorphic assemblage at mid- to high-pressure granulite facies conditions. Stage 2 is represented by the formation of orthopyroxene and plagioclase coronas, indicative of decompression from high- to mid-pressure granulite facies. Stage 3 is characterised by the amphibolite-facies overprint on the granulite-facies assemblages.

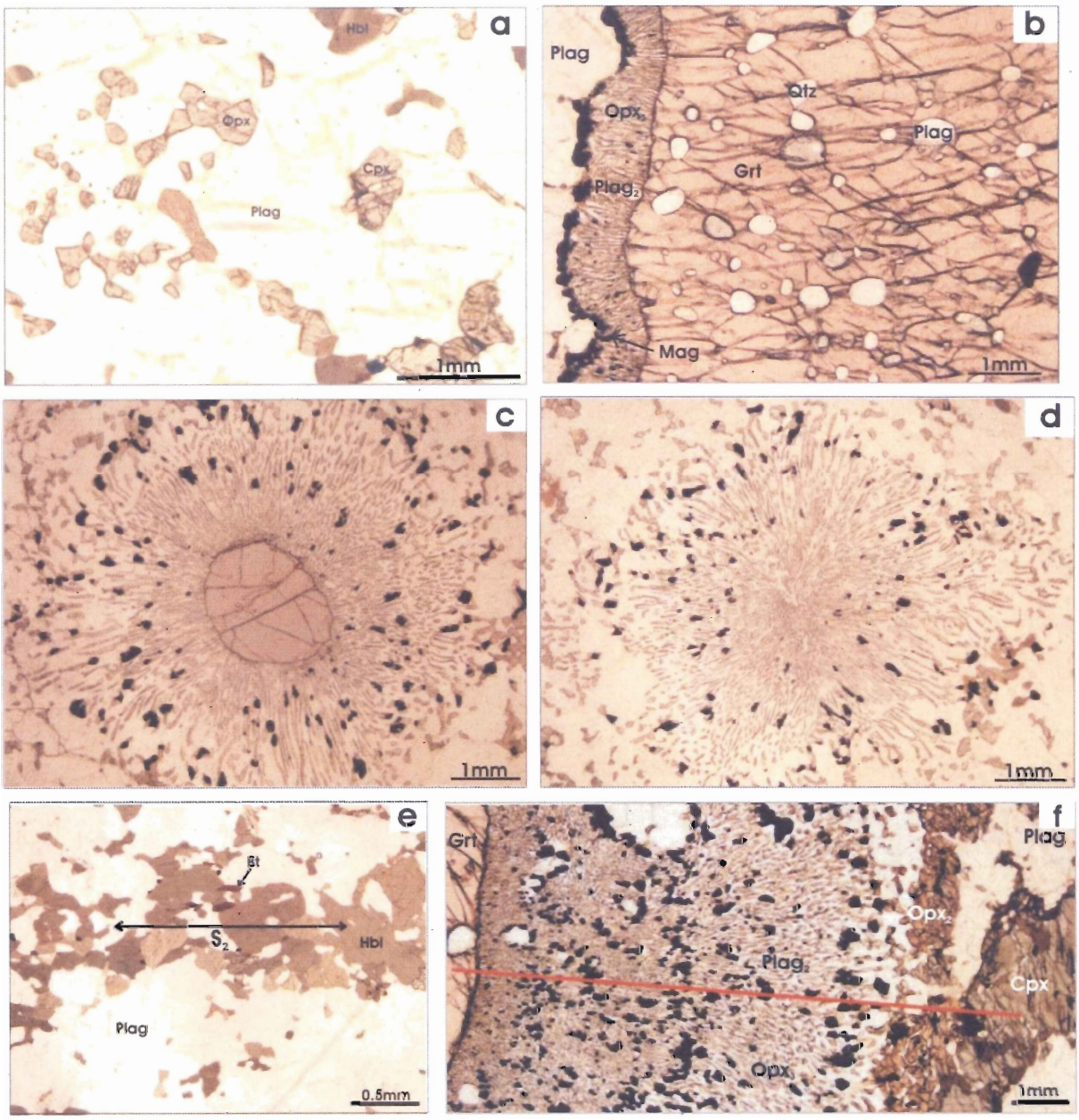

Figure 3.8 Representative textures from garnet anorthosites. (a) Texturally equilibrated matrix assemblage of Plag + Opx + Cpx and replacement of pyroxenes by hornblende, (b) Large garnet porphyroblast with inclusions of plagioclase and quartz and symplectite separating garnet from matrix plagioclase. (c) Garnet porphyroblast surrounded by Type-II symplectite. (d) Type-II symplectite has completely pseudomorphed garnet. (e) S_2 fabric defined by layers rich in hornblende and preferential alignment of biotite.(f) Type-I corona separates the matrix from Type-II symplectite, red line represents transect for mineral analyses in Figure 3.8. (Sample Y107A).

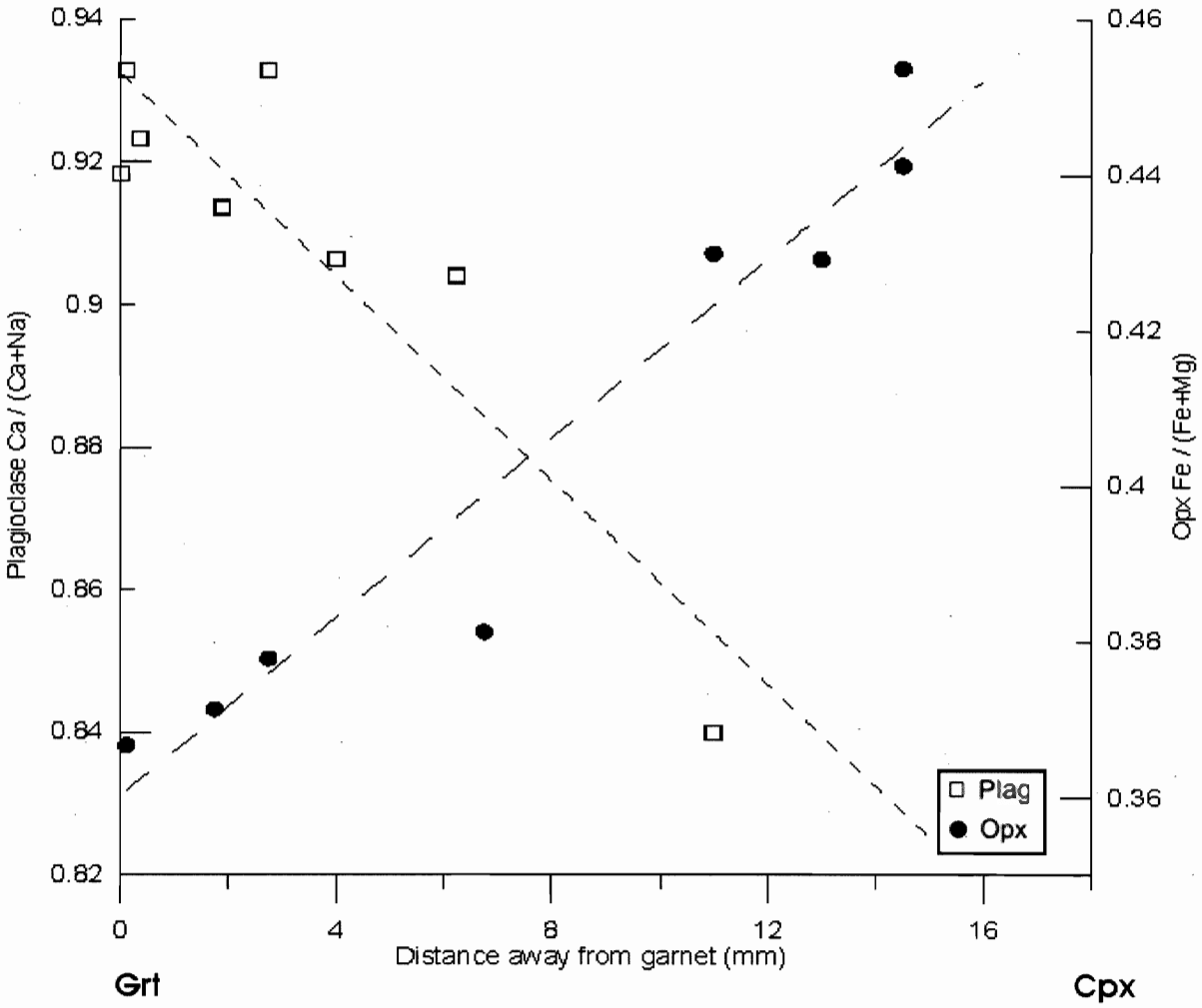

Figure 3.9 Plagioclase and orthopyroxene compositions along a transect (Figure 3.8f) from the garnet rim to matrix clinopyroxene in garnet anorthosite demonstrating *P-T* dependant partitioning of Ca, Mg, and Fe between garnet, clinopyroxene, orthopyroxene, and plagioclase. (Sample Y107A).

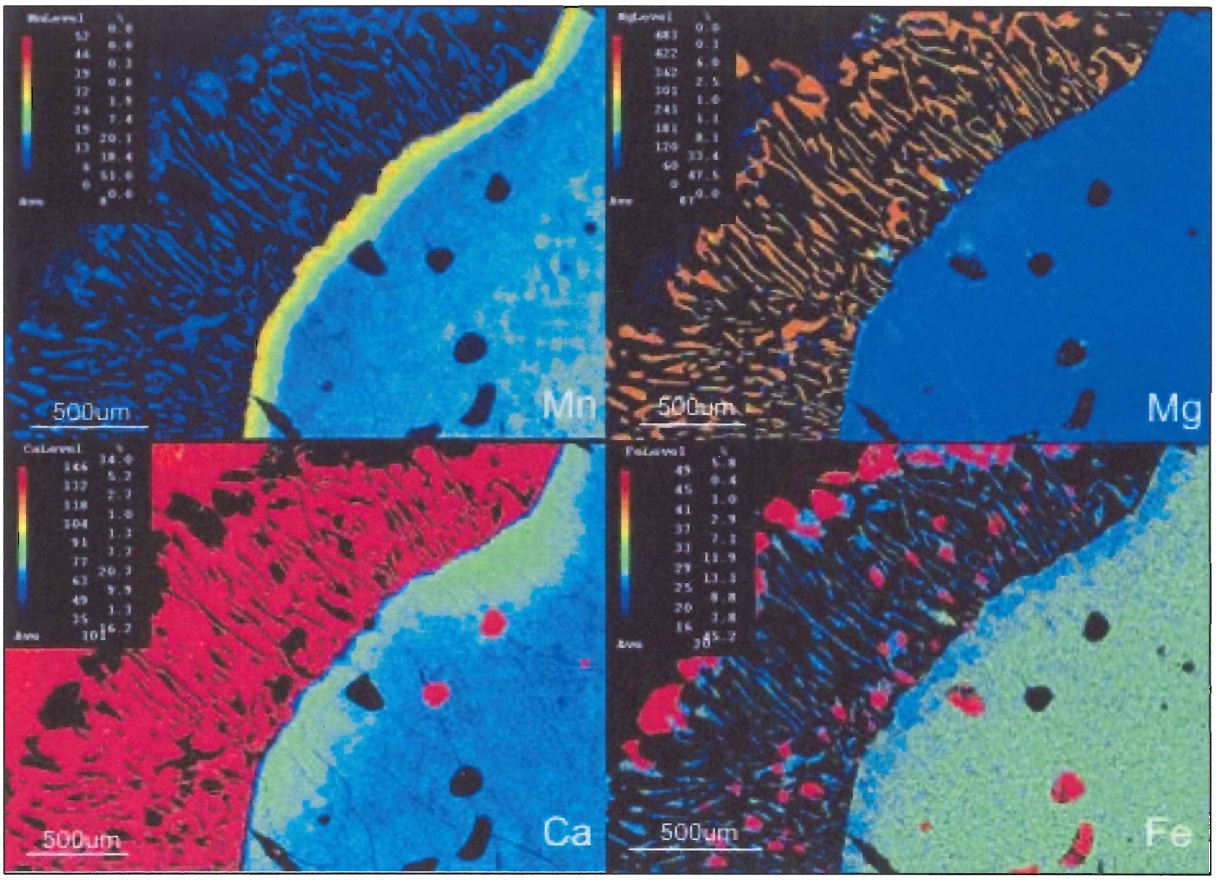

Figure 3.10 Elemental X-ray maps of garnet in garnet anorthosite. Preferential retention of Mn is restricted to a 100 μm zone in the rim of the garnet. Symplectite orthopyroxene has a higher concentration of Mg than that of the garnet and a similar concentration of Fe of the garnet rim. Zoning in the garnet is most likely the product of preferential retention and donation of Fe and Mg, respectively. Ca shows a subtle increase from core to rim, but is restricted to discontinuous patchy zones of Ca enrichment. Colour scale indicates number of counts obtained from each pixel, with red being the largest and dark blue being the smallest (Sample Y107A).

CHAPTER 4
THERMOBAROMETERY

4.1 Introduction

Texturally complex rocks have been shown to be an invaluable tool for the estimation of multiple *P-T* conditions from a single sample (St-Onge *et al.* 1996; Engvik *et al.* 2007). The acquisition of reliable thermobarometric estimates relies heavily on the assumption of chemical equilibrium between co-existing phases. Mineral chemistry in mafic granulites is a function of temperature, pressure, bulk composition and the presence of fluids. Minerals can be chemically homogeneous, or display heterogeneities such as zoning. Zoned minerals represent at least 2 different stages of chemical equilibration (typically in the core and rim), which may correspond to different metamorphic stages.

Local chemical equilibrium between minerals can be preserved in specific textural domains within a sample, in this case:

1. Inclusions in garnets
2. Coronas and symplectites
3. Matrix assemblages

This chapter will assess chemical equilibration between minerals in the different samples and produce *P-T* estimates from targeted textural domains. Combining *P-T* estimates from these domains produces a *P-T* path, which will be interpreted at the end of the chapter.

4.2 Mineral Zoning

Accurate *P-T* estimates in granulites are heavily influenced by zoning within certain minerals that may result from multiple metamorphic events or retrograde diffusion. The rims of zoned minerals are considered to be in chemical equilibrium with adjacent matrix minerals,

reflecting exchange reactions between them. The cores of zoned minerals are the least likely to have been affected by late-stage cation exchange, indicating the closest approximation to peak *P-T* chemistry.

Garnet cores in these samples show little significant zoning of almandine, grossular and pyrope. All garnets show a ~50-100 μm zone of significant spessartine enrichment around the rim, most likely the result of preferential retention of Mn during garnet resorption reactions (Ch.3). Some garnets show an increase in almandine from core to rim, most likely the result of retrograde volume diffusion and not a remnant of prograde metamorphic zoning (Engvik *et al.* 2007).

Elemental maps of garnets (Ch. 3) were used to quantify zoning in garnets in order to select points for chemical analyses that represent near-peak metamorphic conditions. Given homogenous core compositions, all zoning in garnet is interpreted to be retrograde, indicating that any prograde zoning would have been obliterated at peak metamorphic conditions (Ch. 3).

4.3 Methods

4.3.1 TWEEQU

This study uses the Thermobarometery With Estimation of Equilibrium State (TWEEQU) method for *P-T* calculations. TWEEQU uses an internally consistent thermodynamic database to test the assumption that all mineral compositions used in a calculation last equilibrated at the same *P-T* conditions. Mixing properties and chemical analyses are used to produce a phase diagram, with a set of univariant reaction lines. If all plotted reactions intersect at a point, perfect equilibration between minerals can be assumed. If reactions do not intersect at a single point, the degree of scatter of the intersection points provides a qualitative estimate of equilibrium and

uncertainties in the assemblage (Berman 1991). This study uses winTWQ version 2.34 for equilibria calculations and the 2006 database (Berman 2007).

The winINTERSX program, accompanying winTWQ, was used to obtain quantitative estimates of the intersection of metastable univariant reactions in *P-T* space. Optimal results are obtained from a minimum of three independent reactions, in which two define a point in *P-T* space and the third provides an independent test of the results. For Cpx + Grt + Plag + Qtz equilibria, only two independent reactions could be obtained from the samples, which provide a *P-T* estimate without an independent test of equilibrium. Textural relationships were used to determine which domains of clinopyroxene and garnets may have been in chemical equilibrium at near-peak metamorphic conditions. Cumulative errors from the application of the TWEEQU method, solution models, and microprobe errors are considered to be ± 50°C and ± 1 kbar, respectively (Berman, 1991). The solution models used for all phases in this study are summarised in Table 4.1.

Table 4.1 Solution models for minerals

Mineral	v.2.34 Solution Models
Orthopyroxene	Berman and Aranovich (2007)
Garnet	Berman and Aranovich (2007)
Clinopyroxene	Berman *et al.* (1995)
Plagioclase	Fuhrman and Lindsley (1988)

4.3.2 Recalculation software (RCLC)

The TWQ version 2.34 program does not take into account late stage Fe-Mg-Al exchange reactions, which need to be considered for *P-T* estimates from orthopyroxene and garnet. Intermediate to felsic granulites, such as the garnet anorthosites, are particularly susceptible to this, which is related to the difference in the diffusivity of Fe and Mg in garnet, based on the

amount of Ca present. The program recalculation (RCLC) from Pattison *et al.* (2003) can be used to correct for the late-stage cation-exchange. The program assumes that Al is not susceptible to late exchange reactions, but that Fe and Mg are. The program adjusts the Mg-Fe ratio to coincide with the Al-equilibria, and recalculates the position of the equilibria in *P-T* space until all reactions converge. For a detailed description of the method, refer to Pattison *et al.* (2003). When calculating *P-T* estimates using Grt-Opx-Plag-Qtz equilibria, winTWQ reactions were plotted and RCLC was used to obtain corrected *P-T* estimates, which were plotted on the corresponding diagram. RCLC was applied to all calculations of Grt + Opx + Plag + Qtz equilibria.

RCLC is considered to have cumulative errors for pressure and temperature estimates of ±1 kbar and ± 50°C, respectively (D. Pattison *pers. comm.* 2008).

4.4 Activity of Quartz

As discussed in chapter 3, there is very little, if any, quartz in the matrix or coronas of the garnet anorthosites, garnet clinopyroxenites, and mafic granulites. The activity of quartz significantly affects the pressure estimates from garnet-orthopyroxene-plagioclase and garnet-clinopyroxene-plagioclase barometers. The presence of quartz in the samples during peak equilibration can be inferred based on the following criteria:

1) The breakdown of garnet to plagioclase and orthopyroxene cannot proceed in the absence of quartz (Reactions (3) and (6), below);
2) Quartz is present as inclusions in garnet in all samples

A possible explanation for the absence of quartz is that all of it was consumed during retrograde reactions. In the absence of solid quartz, the reaction could have proceeded because migmatitic monzogranites were present in adjacent localities, which may have contributed silica

as a component in a fluid phase. The activity of quartz in all calculations is assumed to be 1. The activity of quartz has a significant effect on pressure-estimates from net-transfer reactions (3), (4), (5), (6), and (9) below, indicating that a pressure estimate using an activity of 1 for quartz ($a_{SiO_2} = 1$) yields the maximum possible pressure recorded in the mineral assemblage.

4.5 *P-T* estimates

The TWEEQU method calculates all the possible reactions between specified minerals or components, the reactions are plotted in *P-T* space, and the intersection of reactions at a single point identifies the *P-T* conditions based on that set of intersecting reactions. All of the reactions used have been experimentally calibrated and are used as standard thermometers and barometers for granulites (Pattison 2003; Indares 2003; O'Brien and Rötzler 2003). The following sets of reactions were used for the TWEEQU method (all reactions are written with the higher temperature assemblage on the right-hand side):

$$3En + Alm = 3Fs + Pyp \quad (1)$$
$$3Di + Alm = 3Hd + Pyp \quad (2)$$
$$Alm + Grs + \beta Qtz = 6Fs + An \quad (3)$$
$$Alm + 2Grs + 3\beta Qtz = 3Hd + 3An \quad (4)$$
$$2Grs + Prp + 3\beta Qtz = 3Di + 3An \quad (5)$$
$$Grs + 2Prp + 3\beta Qtz = 6En + 3An \quad (6)$$
$$Alm = Al\text{-}Opx + 3Fs \quad (7)$$
$$Py = Al\text{-}Opx + 3En \quad (8)$$
$$3An = Al\text{-}Opx + Grs + \beta Qtz \quad (9)$$

Reactions (1) and (2) represent thermometers based on $Fe^{2+} \leftrightarrow Mg^{2+}$ exchange between garnet and orthopyroxene, and garnet and clinopyroxene, respectively. Reactions (3) and (6) represent net-transfer reactions between garnet, orthopyroxene, plagioclase and quartz. Reactions (4) and (5) represent net-transfer reactions between garnet, clinopyroxene, plagioclase and quartz. Reactions (7), (8) and (9) represent net transfer reactions that involve the relatively minor aluminous-orthopyroxene end-member.

4.6 Garnet clinopyroxenites (Sample Y105D)

Garnet clinopyroxenites contain the *P-T*-sensitive assemblage garnet + clinopyroxene + plagioclase + orthopyroxene + quartz + pargasite. Engvik *et al.* (2007) documented the *P-T* evolution of similar assemblages and separated them into three stages: peak metamorphism at high-pressure granulite conditions (stage 1), near-isothermal decompression to mid-pressure granulite conditions associated with corona formation (stage 2), and retrogression to amphibolite facies conditions (stage 3).

Stage 1 is defined by the assemblage clinopyroxene + garnet + plagioclase. This assemblage is characteristic, but not diagnostic, of high-pressure granulite facies (Pattison 2003); (Fig. 4.1). The absence of quartz in the peak assemblage is common in mid- to high-pressure granulite assemblages, but is more common at high-pressures (Pattison 2003).

Stage 2 is characterised by the stability of orthopyroxene and the breakdown of garnet. Two generations of orthopyroxene are present as fine-grained coronas around clinopyroxene and as symplectites around garnet. The consumption of garnet indicates decompression to pressures below the garnet + orthopyroxene stability field, resulting in the lower pressure assemblage orthopyroxene + plagioclase. The new garnet-free assemblage clinopyroxene + orthopyroxene-3 + plagioclase-2 is characteristic of mid-pressure granulite facies conditions.

Stage 3 corresponds to amphibolite-facies overprinting of granulite facies assemblages by pargasitic hornblende. Pargasite may have grown under lower granulite-facies conditions or in upper amphibolite-facies conditions. Representative mineral compositions for sample Y105D can be found in Table 4.2.

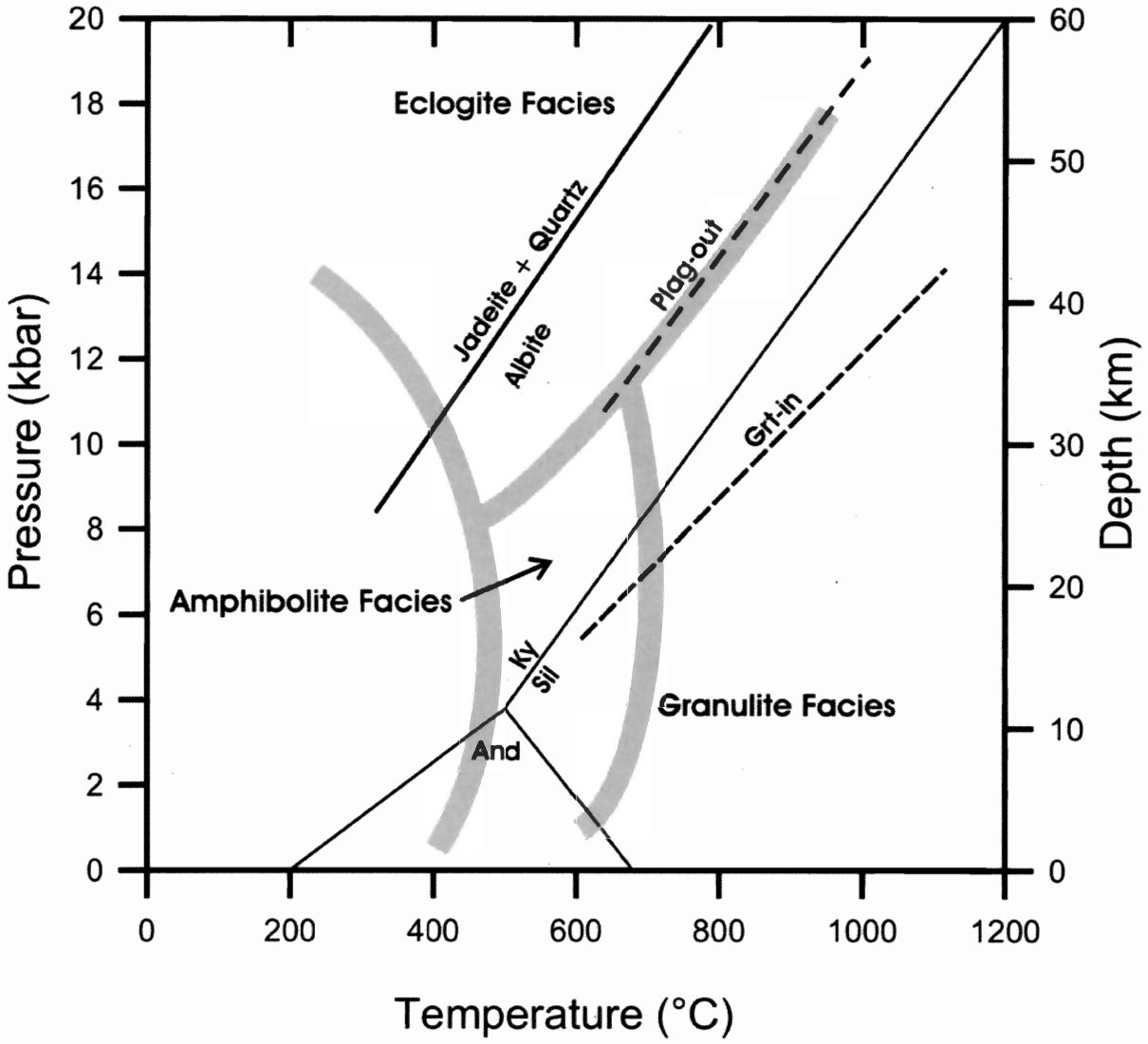

Figure 4.1. Petrogenetic grid showing the amphibolite-, granulite- and eclogite-facies fields and aluminosilicate reactions (after Spear 1995). The 'garnet-in' and 'plag-out' reactions are for a quartz-tholeeite bulk composition (after O'Brien and Rötzler (2003)). The field above the 'Grt-in' reaction in the granulite facies field is considered the high-pressure granulite field (O'Brien and Rötzler 2003).

Table 4.2 Representative mineral analyses from garnet clinopyroxenites (Y105D)

	Grt Core 134	Opx Symp 126	Cpx Core 130	Plag Symp 125	Plag Core 162
SiO_2	38.66	50.99	50.72	44.99	53.66
TiO_2	0.07	0.00	0.08	0.00	0.00
Al_2O_3	21.90	1.69	2.87	35.16	28.88
Cr_2O_3	0.10	0.03	0.06	0.00	0.00
FeO	23.26	24.46	9.40	0.24	0.07
MnO	0.86	0.69	0.30	0.02	0.00
MgO	6.10	19.55	12.12	0.00	0.00
CaO	8.93	0.37	21.89	17.84	11.44
Na_2O	0.00	0.00	0.41	1.22	5.34
K_2O	0.04	0.03	0.03	0.04	0.15
Total	99.93	97.82	97.88	99.50	99.53
Si	2.99	1.97	1.94	2.08	2.44
Ti	0.00	0.00	0.00	0.00	0.00
Al	2.00	0.08	0.13	1.92	1.55
Cr	0.01	0.00	0.00	0.00	0.00
Fe^{2+}	1.50	0.79	0.30	0.01	0.00
Mn	0.06	0.02	0.01	0.00	0.00
Mg	0.70	1.12	0.69	0.00	0.00
Ca	0.74	0.02	0.90	0.89	0.56
Na	0.00	0.00	0.03	0.11	0.47
K	0.00	0.00	0.00	0.00	0.01
Total	8.01	4.00	4.01	5.01	5.03
X_{Mg}		58.75	69.65		
X_{Fe}		41.25	30.35		
Alm	50.08				
Pyp	23.40				
Grs	24.64				
Spss	1.88				
An				88.84	53.78

4.6.1 Prograde

Inclusions of clinopyroxene and plagioclase in garnet provide a possible relict assemblage of prograde metamorphism. An inclusion of clinopyroxene contains abundant exsolution lamellae of orthopyroxene, indicative of chemical disequilibrium. Inclusions of plagioclase show zoning with Ca increasing from core to rim. Core compositions of plagioclase are interpreted to have equilibrated with the growing garnet, and were used for *P-T* estimates.

The assemblage of plagioclase + quartz + garnet is inadequate for quantitative *P-T* estimates because a second Mg-Fe bearing phase is required for cation-exchange or net-transfer reactions. The presence of plagioclase inclusions in garnet indicates that during prograde metamorphism and garnet growth, plagioclase was stable. This indicates that the prograde *P-T* path most likely did not cross the plagioclase-out reaction boundary in Figure 4.2. At very high-pressures, sodium is preferentially partitioned from feldspars into pyroxenes (Spear 1995). The absence of Na-clinopyroxene (jadeite) from the inclusion assemblage indicates that the prograde path did not cross into the eclogite-facies stability field (Fig. 4.2c).

4.6.2 Stage 1

Stage 1 metamorphic conditions can be quantitatively determined by Grt + Cpx + Plag + Qtz equilibria. Garnet analyses were obtained from the cores of large (>1 mm) garnets, away from inclusions and prominent zoning, in order to minimize the effects of retrograde diffusion zoning (O'Brien and Rötzler 2003). Clinopyroxene analyses were obtained from the centre of large (>1 mm) grains, away from exsolution lamellae of orthopyroxene, to avoid areas affected by retrograde exchange reactions. Plagioclase analyses were obtained from the cores of zoned matrix grains that display increasing Ca from core to rim, with the cores representing the best estimates for peak conditions and the rims representing retrograde exchange reactions involving formation of calcic plagioclase at the expense of grossular-rich garnet.

P-T estimates using the winTERSX program from garnet, clinopyroxene and plagioclase place peak metamorphic conditions at 12.1 ± 1 kbar and 841 ± 50°C, using 2 independent reactions: (2) and (6) (Fig. 4.2a). This estimate was derived from the intersection of two

independent reactions, so there is no calculated error on the intersection, so standard errors of ± 50°C and ±1 kbar are applied. This is consistent with high-pressure granulite facies conditions.

4.6.3 Stage 2

Stage 2 metamorphic conditions were determined using Grt + Opx + Plag + Qtz equilibria. All rim analyses of the garnets were inside the Mn-enriched zone, so only core compositions were available. Plagioclase and orthopyroxene analyses were obtained from the adjacent symplectite of the garnet, interpreted to represent local chemical equilibrium.

P-T conditions place stage-2 metamorphic conditions at 8.2 ± 0.3 kbar and 788 ± 18°C using 3 independent reactions: (1), (6) and (9). Recalculation using RCLC yielded 9.2 ±1 kbar and 814 ± 50°C (Figure 4.2b). This is consistent with near-isothermal decompression from high-pressure granulite conditions into mid-pressure granulite facies conditions.

4.6.4 Stage 3

Stage 3 metamorphism corresponds to amphibolite-facies overprinting of granulite-facies assemblages. Retrogression from granulite- to amphibolite-grade is evident from the extensive replacement of matrix and coronitic pyroxenes by pargasite, which post-dates corona and symplectite growth. Quantitative *P-T* estimates could not be determined because pargasite and garnet are never in contact so the equilibration, essential for Grt-Par-Plag-Qtz thermobarometery, could not be assumed. The amphibole-plagioclase thermometer after Holland and Blundy (1994) is an alternative to winTWQ and was calibrated for plagioclase compositions between An_{10} and An_{90}. The Holland and Blundy thermometer was not calibrated for plagioclase composition $An_{>90}$, so it was not used in this study. The *P-T* path has been extrapolated through the

amphibolite-facies field to reflect a retrogression path common to many high-grade terranes after isothermal decompression (Fig. 4.2c); (Spear 1995: Jamieson *et al.* 2004; Engvik *et al.* 2007).

4.7 Mafic granulites (sample Y108A)

Mafic granulites are distinguished from garnet clinopyroxenites by the presence of stable orthopyroxene in the peak assemblage. The *P-T* sensitive assemblage of orthopyroxene + clinopyroxene + plagioclase + garnet is diagnostic of mid-pressure granulite-facies conditions (O'Brien and Rötzler 2003; Pattison 2003). The difference in mineralogy between the samples may be a product of bulk chemical composition, but no bulk analyses were conducted to confirm this. Similar to the garnet clinopyroxenites, the *P-T* evolution of the mafic granulites can be divided into three stages: peak metamorphic conditions (Stage 1), decompression through the garnet stability field (stage 2), and amphibolite facies overprinting (stage 3).

Stage 1 is defined by the peak assemblage Grt + Cpx + Opx +Plag + Qtz, diagnostic of mid-pressure granulite facies conditions. Similar to the garnet clinopyroxenites, the lack of quartz in the assemblage may be attributed to its consumption during prograde metamorphism.

Stage 2 corresponds to the introduction of orthopyroxene-2 into the assemblage by the breakdown of garnet and the product of the reaction between garnet and clinopyroxene. The breakdown of garnet can be attributed to decompression into the mid- to low-pressure granulite fields (Fig. 4.1).

Stage 3 corresponds to the amphibolite-facies overprinting of granulite-facies assemblages. A subtle increase the almandine component of garnet from core to rim is attributed to retrograde diffusion. Representative mineral compositions for samples Y108A can be found in Table 4.2.

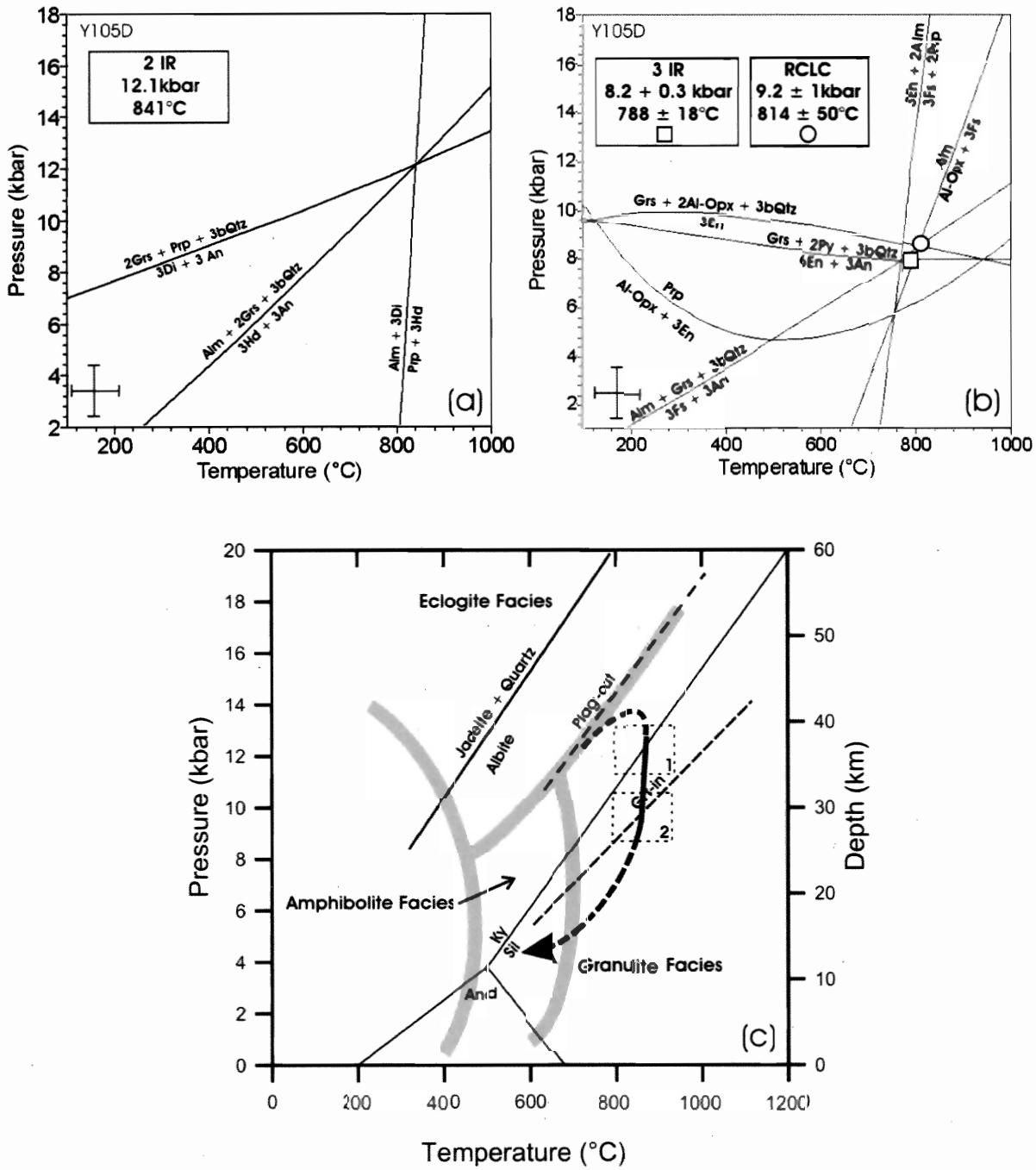

Figure 4.2 Intersection of reactions generated by TWQview for specified reactions in garnet clinopyroxenite sample Y105D. (a) stage 1 (peak) metamorphic conditions, determined from intersection of Grt + Cpx + Plag + Qtz equilibria. (b) stage 2 *P-T* conditions determined from intersection of Grt + Opx + Plag + Qtz equilibria in symplectite, squares represent winTERSX calculated *P-T* estimates and circles represent RCLC recalculated *P-T* estimates. (c) *P-T* path with inferred prograde and retrograde paths. Crosses in lower right hand corner of (a) and (b) represent standard cumulative errors associated with thermobarometric estimates of ± 50°C and ± 1 kbar.

Table 4.3 Representative mineral analyses from mafic granulites (Y108A)

	Grt Core 202	Grt Rim 203	Cpx Core 217	Opx Symp 210	Plag Core 373	Plag Symp 211
SiO_2	38.24	38.48	49.50	51.25	54.44	44.20
TiO_2	0.10	0.06	0.41	0.01	0.00	0.00
Al_2O_3	22.96	21.88	4.58	1.99	28.38	35.96
Cr_2O_3	0.08	0.10	0.04	0.05	0.00	0.00
FeO	22.22	24.35	8.56	22.92	0.13	0.52
MnO	0.65	1.49	0.23	0.50	0.00	0.01
MgO	9.40	7.32	12.70	22.37	0.00	0.00
CaO	7.21	7.03	23.32	0.38	10.69	19.23
Na_2O	0.01	0.02	0.44	0.00	5.49	0.88
K_2O	0.02	0.03	0.02	0.02	0.23	0.02
Total	100.89	100.75	99.79	99.50	99.36	100.83
Si	2.90	2.96	1.86	1.93	2.47	2.03
Ti	0.01	0.00	0.01	0.00	0.00	0.00
Al	2.05	1.98	0.20	0.09	1.52	1.95
Cr	0.00	0.01	0.00	0.00	0.00	0.00
Fe^{2+}	1.41	1.57	0.27	0.72	0.00	0.02
Mn	0.04	0.10	0.01	0.02	0.00	0.00
Mg	1.06	0.84	0.71	1.25	0.00	0.00
Ca	0.59	0.58	0.94	0.02	0.52	0.95
Na	0.00	0.00	0.03	0.00	0.48	0.08
K	0.00	0.00	0.00	0.00	0.01	0.00
Total	8.07	8.05	4.04	4.03	5.02	5.03
X_{Mg}			0.726	63.50		
X_{Fe}			0.274	36.50		
Alm	45.47	50.84				
Pyp	34.29	27.21				
Grs	18.89	18.80				
Spss	1.35	3.15				
An					51.10	92.22

4.7.1 Prograde Metamorphism

Inclusions of plagioclase + quartz ± orthopyroxene provide a relict assemblage probably representing prograde metamorphism. The orthopyroxene is always isolated from the garnet by intervening plagioclase. Several analyses indicate wide variations in plagioclase and orthopyroxene compositions, with no apparent trend, indicative of chemical disequilibrium. To obtain accurate *P-T* estimates, detailed elemental maps of inclusions would be needed to map out

compositional variations in orthopyroxene and plagioclase. The prograde *P-T* path is interpreted to have not passed the 'plagioclase-out' reaction boundary, similar to the garnet clinopyroxenites discussed in section 4.4.1.

4.7.2 Stage 1

Stage 1 peak metamorphic conditions can be determined by the application of Cpx + Grt + Plag + Qtz equilibria. Similar criteria were employed for mineral selection for the mafic granulites as in the garnet clinopyroxenites. Orthopyroxene was not used in the stage 1 *P-T* estimates because all orthopyroxene was relatively fine-grained and extensively replaced by hornblende. Using various orthopyroxene compositions yielded winTERSX generated errors on the order of ± 110°C and ±1.1 kbar, indicative of chemical disequilibrium between these phases. Clinopyroxene and garnet were used due to their larger sizes and lesser susceptibility to late stage Fe-Mg exchange reactions. *P*-T estimates using the winTERSEX program place near-peak metamorphic conditions art 11.8 ± 1 kbar and 773 ± 50°C using 2 independent reactions: (2) and (5) (Figure 4.3a).

4.7.3 Stage 2

Stage 2 metamorphic conditions can be determined in a similar manner to those in garnet clinopyroxenites, by the application of Grt + Opx + Plag + Qtz equilibria. *P-T* conditions determined from the garnet rim, orthopyroxene-3 and plagioclase-2 place stage-2 metamorphism, using the winTERSX program at 8.1 ± 0.3 kbar and 726 ± 18°C using 3 independent reactions: (2), (6) and (9). Recalculation using RCLC places *P-T* estimates at 8.7 ± 1 kbar and 742 ± 50°C. (Figure 4.3b).

4.7.4 Stage 3

Stage 3 corresponds to an amphibolite-facies overprinting the granulite-facies assemblage. Similar to the garnet clinopyroxenites, extensive replacement by brown-green pargasite of matrix and coronitic pyroxenes indicate retrogression from granulite- to amphibolite-grade. *P-T* estimates could not be determined for stage 3 and the *P-T* path was extrapolated into the amphibolite-facies field as discussed in Section 4.6.3.

4.8 Garnet anorthosites

Garnet anorthosites contain the *P-T* sensitive assemblage Grt + Opx + Plag + Hbl ± Qtz. The *P-T* evolution can be summarised as three stages: peak metamorphic conditions (stage 1), near-isothermal decompression through the stability field for garnet (stage 2), and amphibolite facies overprinting of granulite facies assemblages (stage 3). The growth of hornblende during stage 3 created a penetrative fabric that developed post-D_1 and pre-D_2. Representative mineral analyses can be found in Table 4.4.

4.8.1 Prograde Metamorphism

Inclusions of plagioclase + quartz in garnet are possible remnants of a prograde metamorphic path. The presence of plagioclase signifies that the prograde *P-T* path never passed the 'plagioclase-out' reaction prior to the growth of garnet as discussed in section 4.4.1.

4.8.2 Stage 1

Stage 1 metamorphic conditions can be quantified by the application of Grt + Cpx + Plag + Qtz thermobarometery. Representative analyses were taken from the cores of large (>1 mm) garnets away from zones of elemental enrichment/depletion. Analyses were obtained from the core of a large (~5mm long) clinopyroxene, away from areas with exsolution lamellae.

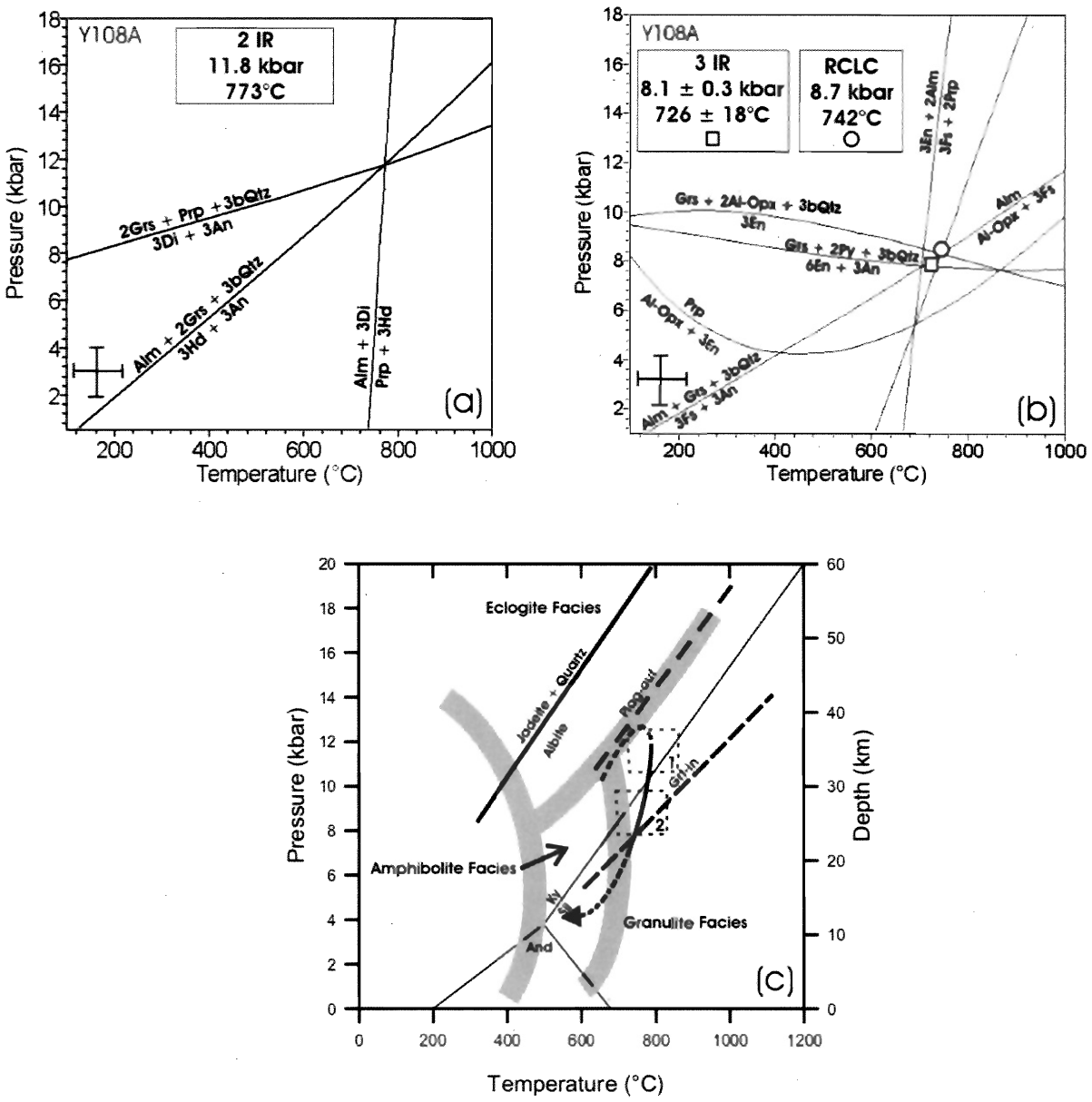

Figure 4.3 Intersection of reactions generated by TWQview for specified reactions in mafic granulite sample Y108A, (a) stage 1 (peak) metamorphic conditions, determined from intersection of Grt + Cpx + Plag + Opx equilibria (c) stage 2 *P-T* conditions determined from intersection of Grt + Opx + Plag + Qtz equilibria in symplectite, with the circle representing recalculated equilibria from RCLC (c) *P-T* path with inferred prograde path retrograde (dotted line). Crosses in lower right hand corner of (a) and (b) represent standard cumulative errors associated with thermobarometric estimates of ± 50°C and ± 1 kbar.

Plagioclase analyses were obtained from the cores of large (>1 mm) grains, adjacent to the large clinopyroxene. *P-T* estimates of near-peak metamorphic conditions are 7.8 ± 1 kbar and 735 ± 50°C, using 2 independent reactions: (2) and (6)

4.8.3 Stage 2

Stage 2 *P-T* conditions were determined in a manner similar to that of the garnet clinopyroxenites and the mafic granulites, using garnet rim compositions and analyses of orthopyroxene and plagioclase from symplectites adjacent to the garnet. The RCLC program was used to correct for late stage Fe-Mg-Al exchange reactions for garnet-orthopyroxene-plagioclase-quartz equilibria. *P-T* estimates using winTERSX for stage 2 are 7.5 ± 0.7 kbar and 675 ± 42°C using 3 independent reactions: (2), (6) and (9). RCLC corrected estimates place stage 2 metamorphic conditions at 8.7 ± 1 kbar and 764 ± 50°C.

These estimates indicate an increase in pressure and temperature during garnet dissolution, which is always considered a decompression reaction (Elevold *et al.* 2003; Engvik *et al.* 2007). An increase in apparent temperature could result from any number or thermal perturbations or unknown mineralogical and textural factors. The calculated variation could be attributed to the lack of quartz in the assemblage, which the RCLC method assumes is present in excess (Pattison 2003). An increase in pressure seems unlikely and is attributed to unknown compositional and/or textural factors or poor analysis selection that influenced the pressure estimate. The errors of the *P-T* estimates overlap, indicating that the assemblages may have equilibrated at the same time.

4.8.4 Stage 3

Stage 3 corresponds to amphibolite facies overprinting of granulite facies assemblages. Similar to the other lithologies, replacement of matrix and coronitic pyroxenes by pargasite is

indicative of retrogression from granulite- to amphibolite-facies. Similar to the mafic granulites and garnet clinopyroxenites, quantitative *P-T* estimates could not be obtained with the observed assemblage. The *P-T* path was extrapolated into the amphibolite-facies field, as discussed in section 4.6.4.

Table 4.4 Representative mineral analyses from garnet anorthosites (sample Y107A)

	Grt Core 119	Grt Rim 57	Cpx Core 112	Opx Symp 85	Plag Core 73	Plag Symp 99
SiO_2	38.09	38.10	50.87	51.34	50.98	44.54
TiO_2	0.04	0.00	0.19	0.06	0.00	0.00
Al_2O_3	22.18	22.20	2.06	1.82	29.67	35.63
Cr_2O_3	0.06	0.00	0.04	0.05	0.00	0.00
FeO	26.61	25.67	9.49	22.94	0.00	0.44
MnO	1.62	1.48	0.39	1.23	0.00	0.00
MgO	5.19	5.71	12.02	21.21	0.00	0.00
CaO	6.46	7.02	21.47	0.40	13.26	18.30
Na_2O	0.00	0.00	0.39	0.00	4.00	1.09
K_2O	0.04	0.00	0.02	0.04	0.13	0.04
Total	100.29	100.17	96.94	99.09	98.05	100.05
Si	2.97	2.97	1.97	1.95	2.36	2.06
Ti	0.00	0.00	0.01	0.00	0.00	0.00
Al	2.04	2.04	0.09	0.08	1.62	1.94
Cr	0.00	0.00	0.00	0.00	0.00	0.00
Fe^{2+}	1.74	1.67	0.31	0.73	0.00	0.02
Mn	0.11	0.10	0.01	0.04	0.00	0.00
Mg	0.60	0.66	0.69	1.20	0.00	0.00
Ca	0.54	0.59	0.89	0.02	0.66	0.91
Na	0.00	0.00	0.03	0.00	0.36	0.10
K	0.00	0.00	0.00	0.00	0.01	0.00
Total	8.01	8.02	4.00	4.01	5.01	5.02
X_{Mg}			69.31	62.22		
X_{Fe}			30.69	37.78		
Alm	58.14	55.39				
Pyp	20.21	21.97				
Grs	43.19	43.53				
Spss	3.58	3.22				
X_{An}					64.15	90.06

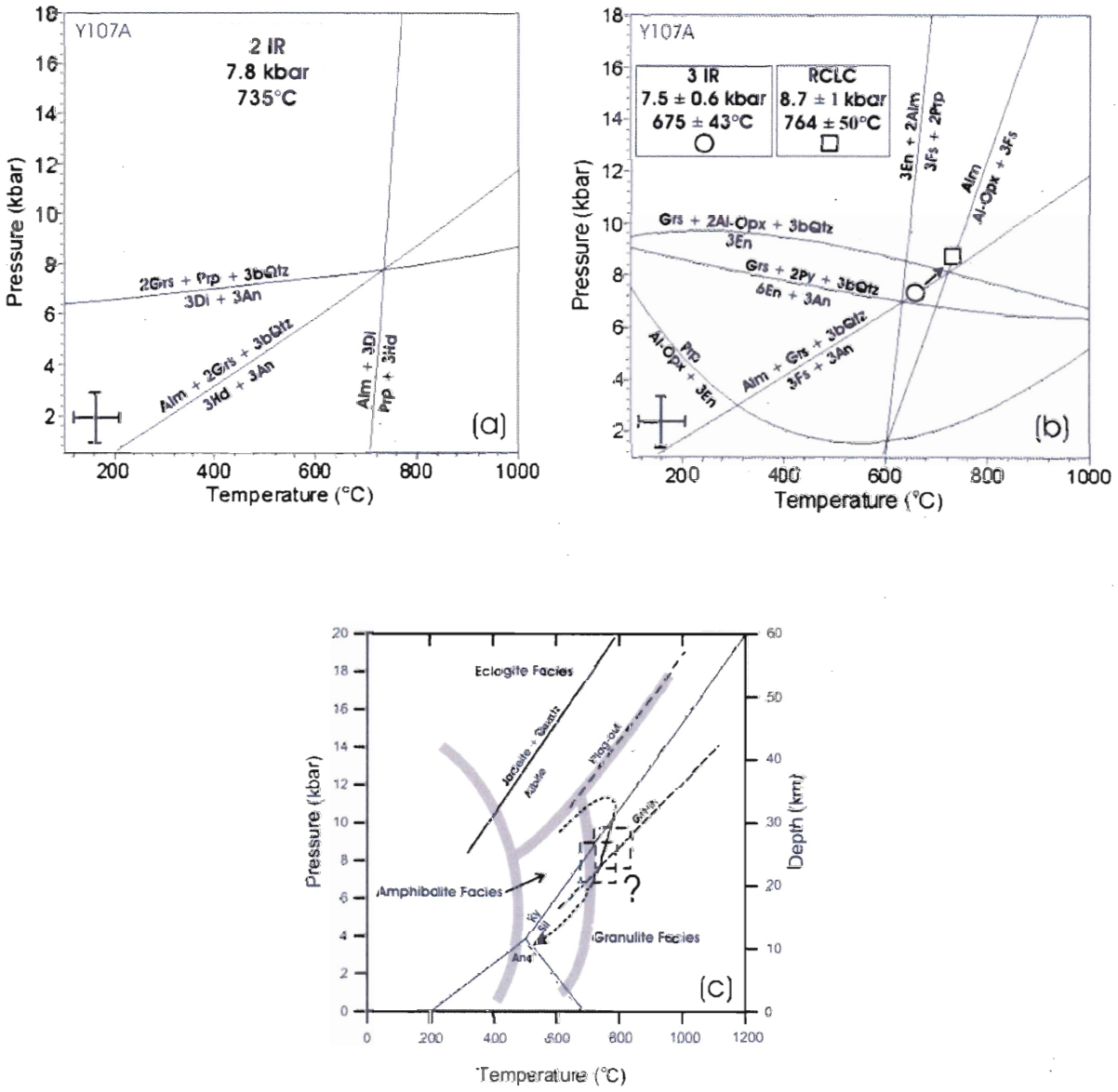

Figure 4.4 Intersection of reactions generated by TWQview for specified reactions in garnet anorthosite sample Y107A, (a) Stage 1 (peak) metamorphic conditions, determined from intersection of garnet + clinopyroxene + plagioclase + quartz equilibria (b) Stage (2) metamorphic conditions determined from intersection of grt + opx + plag + qtz equilibria, correction for late opx-grt Fe and Mg exchange by RCLC (Pattison, 2003), dashed lines show corrected equilibria. (c) Possible *P-T* path of garnet anorthosites with anomalous increase in pressure and temperature between stages 1 and 2. Crosses in lower right hand corner of (a) and (b) represent standard cumulative errors associated with thermobarometric estimates of ± 50°C and ±1 kbar.

4.9 Discussion

Near isothermal decompression paths are common in many granulite belts around the world and can be explained by:

1. Unroofing by thrusting and erosion (Spear, 1995)
2. Unroofing by extension and/or erosion (Spear, 1995)
3. Unroofing by lateral movement from thicker towards thinner crust (Jamieson *et al.*, 2004)
4. Decompression coincident with granite emplacement

High-pressure granulites have been extensively documented in many orogenic belts, ranging in age from Archean to present (Indares 2003; O'Brien and Rötzler 2003; Pattison 2003; Engvik *et al.* 2007). High-pressure granulites exposed at the surface indicate peak-metamorphism at depths >50 km, indicative of tectonically thickened crust (O'Brien and Rötzler 2003).

The *P-T* paths of the samples equilibrated in the high-pressure granulite field most likely represent exhumed lower crust that resulted from crustal thickening, associated with the either Trans-Hudson orogeny or the Paleoproterozoic amalgamation of the western Churchill Province. The similarity of the *P-T* paths obtained from the garnet pyroxenite and mafic granulite samples indicate they are most likely genetically related. They display similar pressures and temperatures along the multistage decompression *P-T* path.

The garnet anorthosite *P-T* path indicates lower peak metamorphic conditions. The anorthosite may have been emplaced at a different depth along the retrograde path of the garnet clinopyroxenites and mafic granulites. Alternatively, the differences in peak *P-T* conditions may simply show that the garnet anorthosite could not preserve peak *P-T* conditions owing to its mineral assemblage. Testing these interpretations will require geochronological data.

CHAPTER 5
THERMOCHRONOLOGY

5.1 Introduction

There are currently no published geochronological data from Southampton Island. This study will provide the first thermochronological dates of samples collected from Southampton Island. U-Pb dating of monazite and zircon is currently in progress by Rob Berman and Nicole Rayner at the Geological Survey of Canada in Ottawa. The combination of dates from U-Pb and $^{40}Ar/^{39}Ar$ geochronology will provide a detailed *T-t* path relating to the tectonic evolution of Southampton Island, essential for comparison with surrounding regions.

This study uses $^{40}Ar/^{39}Ar$ thermochronology in order to provide a date for cooling through the closure temperature of hornblende (~500°C). A single sample from each sampling locality in the study area was collected for $^{40}Ar/^{39}Ar$ analysis, with a preference for hornblende-rich samples. With the exception of Y107, a garnet anorthosite, all other samples are mafic granulites. Mafic granulite samples typically contain >30% hornblende and garnet anorthosite samples typically contain ~5% hornblende.

5.2 $^{40}Ar/^{39}Ar$ Method

The $^{40}Ar/^{39}Ar$ method is a variation on the K-Ar method of thermochronology that overcomes the different chemical affinities of Ar and K. Potassium is a common mineral in the earths crust and is readily partitioned into the crystal structure of hornblende, biotite, muscovite and K-feldspar. A naturally occurring radioactive isotope of potassium, ^{40}K, decays to ^{40}Ca and ^{40}Ar with half lives of ~1.34 Ga and ~11.93 Ga, respectively. Since the decay constants are known, given a closed chemical system, the ratio of parent to daughter isotopes provides a quantitative measure of age (McDougall and Harrison 1999).

$$^{40}Ar_{total} = {}^{40}Ar_{Initial} + (\lambda_e + \lambda_e' / \lambda) \cdot {}^{40}K (e^{\lambda t} - 1) \quad (5.1)$$

In which λ_e and λ_e' are partial decay constants, λ is the decay constant, and t is time (McDougall and Harrison 1999). K-Ar dating assumes that all ^{40}Ar was outgassed at the time of formation and that all ^{40}Ar is radiogenic. Equation 5.1 then simplifies to:

$$^{40}Ar^{*} = (\lambda_{EC} / \lambda_{total}) \cdot {}^{40}K(e^{\lambda total \cdot t} - 1) \quad (5.2)$$

Where $^{40}Ar^{*}$ represents radiogenic argon only.

Measuring the ratio of ^{40}K to ^{40}Ar is difficult, due to the different chemical affinities of the elements. To overcome this difficulty, ^{39}K is converted to ^{39}Ar by the bombardment of neutrons in a nuclear reactor:

$$^{39}_{19}K + n \rightarrow {}^{39}_{18}Ar + p \quad (5.3)$$

Where n is a neutron and p is a proton. The relatively long half-life of ^{39}Ar ($t_{1/2}$ = 269 a) means it can be considered a stable isotope for mass-spectrometry. The ratio of $^{40}Ar^{*}/^{39}Ar$ is proportional to the ratio of $^{40}Ar^{*}/^{40}K$ (used in K-Ar dating), and is easier to measure using a mass spectrometer. The ratio of $^{40}Ar^{*}/^{39}Ar$ can be used to calculate an apparent age using the following equation:

$$T = (1/\lambda) \ln [J (^{40}Ar^{*}/^{39}Ar) + 1] \quad (5.4)$$

$$\text{where } J = {}^{39}K \lambda T \int \varphi(E)\sigma(E)dE / {}^{40}K \lambda_e \quad (5.5)$$

In which J is the irradiation parameter, φ is neutron flux, σ is the cross-sectional area, T was the duration of neutron irradiation, and E is neutron energy.

To evaluate J, standard minerals of known age are irradiated and analyzed with the unknown samples. During irradiation, calcium, potassium, argon, and chlorine produce isotopes of ^{36}Ar, ^{37}Ar, ^{38}Ar, ^{39}Ar and ^{40}Ar. Calcium in particular produces significant amounts of ^{36}Ar and ^{39}Ar, which can considerably influence the uncorrected $^{40}Ar^{*}/^{39}Ar$ date. ^{37}Ar is produced exclusively from ^{40}Ca during irradiation, and can be used to correct from ^{36}Ar and ^{39}Ar from

calcium ($^{39}Ar/^{37}Ar)_{Ca}$. Potassium can produce neutron-induced ^{40}Ar, corrected for by measuring $^{40}Ar/^{39}Ar$ from a sample with a known age. For a detailed description of standard corrections applied to $^{40}Ar/^{39}Ar$ data, the reader is referred to McDougall and Harrison (1999).

In K-bearing minerals, radiogenic ^{40}Ar is produced from ^{40}K at a constant rate within the crystal. At a specific temperature, the mobile daughter products (^{40}Ar) of radioactive decay become completely immobile in a given sample. This is referred to as the 'closure temperature', given by the following formula:

$$T_c = R / [E \ln(A \tau D_0 / a^2)] \quad (5.6)$$

In which R is the gas constant, a is a characteristic diffusion size, A is a numerical constant depending on geometry decay constant of the parent isotope, E is the activation energy, τ is the time constant, interpreted in terms of cooling rate, with which the diffusion coefficient D_0 diminishes (Dodson 1973).

The 'closure temperature' (T_c) of a geochronological system is defined as the temperature at the time corresponding to its apparent age (Dodson 1973). The closure temperature for hornblende varies depending on: 1) the geometry of the crystals, 2) the rate of cooling, and 3) diffusion coefficients in the crystal. In a typical hornblende crystal, the closure temperatures, with diffusion radii of 40-80 μm, vary from 580°C in rapidly cooled bodies (~1000°C / Ma) to 480°C for relatively slowly cooled bodies (~5°C / Ma) (Harrison 1981).

There are two common methods to extract all Ar from a given sample: total fusion and step-heating. Total fusion heats the sample until it is completely degassed, and then the Ar-ratios are measured. Step-heating is more effective than total fusion because it measures the progressive outgassing from a sample and provides a mechanism for determining anomalous mineral species in a mineral separate. It also allows partially disturbed systems, such as the rims

of minerals, which are most susceptible to diffusion to diffuse at a lower temperature. The step-heating technique involves the incremental heating of a sample until the sample becomes completely degassed. An apparent age for each step is calculated and plotted on an age vs. % Ar released diagram.

The determination of the age from a spectrum plot depends on the identification of a 'plateau'. A typical 'plateau' is defined by adjacent steps that comprise more than 50% of the total argon released and yield an age within 2σ of the calculated mean (McDougall and Harrison 1999).

5.3 Sample Preparation

Mafic granulites and garnet anorthosites from this study contain varying quantities of hornblende. Hornblende in these samples readily incorporates K into the 'W' site of its crystal structure; (Deer, Howie, and Zussman 1996) (Table 3.1). EMP analysis of thin-sections from the samples were conducted, and samples containing hornblende with the highest K content (~1 wt%) were selected and prepared for Ar-Ar analysis (Appendix A).

Samples were crushed and hornblende grains were separated by hand under a binocular microscope. Approximately 10 mg of hornblende was collected from each sample. Samples and standards were irradiated at the McMaster University Nuclear Reactor in Hamilton, Ontario in December, 2007. Samples and standards were run at the $^{40}Ar/^{39}Ar$ laboratory at Dalhousie University, Halifax from Jan 28-30.

5.4 Ar-Ar Results

5.4.1 Mafic Granulites

Sample Y105A shows a plateau with an integrated age of 1764 ± 12 Ma (Fig. 5.1a). Sample Y106 has a plateau age of 1748 ± 12 Ma (Fig 5.1b). Sample Y108 has a plateau at 1754

± 12 Ma (Fig 5.1c). None of the mafic granulites show penetrative fabrics. The random orientation and dispersion of hornblende makes it impossible to determine a relationship of mineral growth to fabric development, but the data provide an age for cooling through the closure temperature of hornblende.

5.4.2 Garnet Anorthosite

Sample Y107 yielded a plateau age of 1718 ± 12 Ma (Fig 5.1d). The parallel alignment of hornblende in the garnet anorthosites defines a possible S_2 fabric. Since hornblende grew above its closure temperature, the age gives a minimum age of ~1720 Ma for the development of S_2 and D_2.

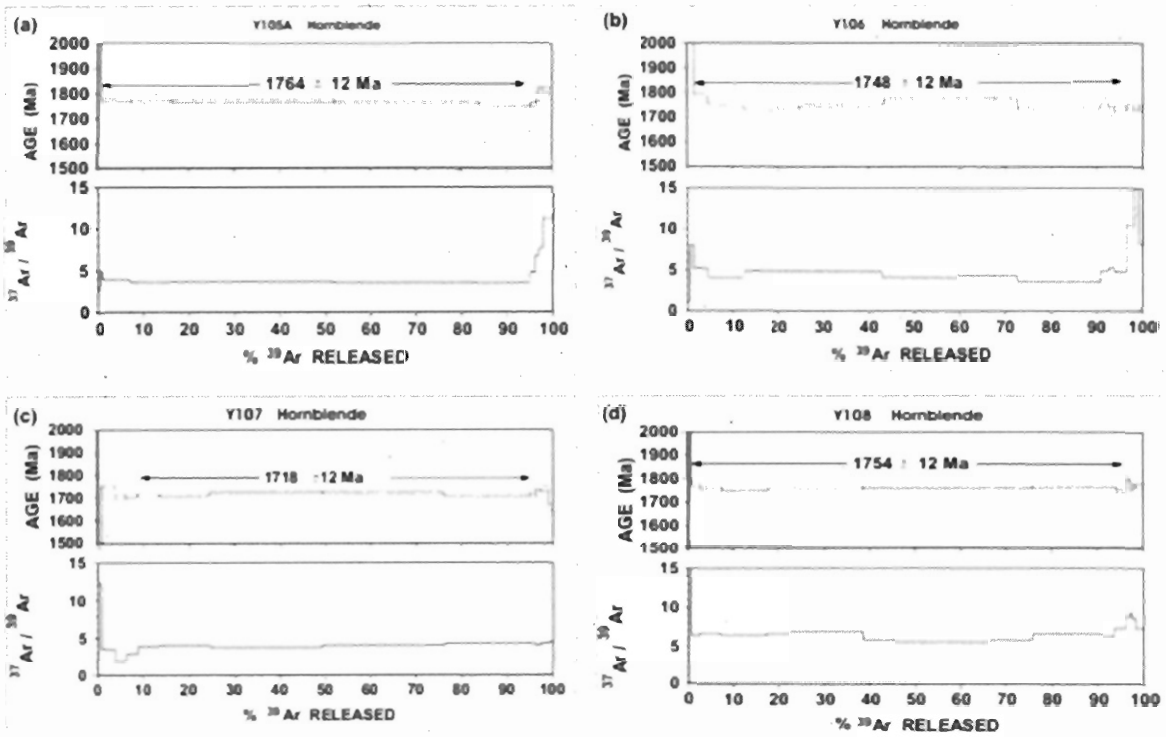

Figure 5.1 Ar-Ar plateaus for selected samples. Ages are given with an error of 2σ. Samples Y105A, Y106, and Y108 are mafic granulites and Y107 is a garnet anorthosite.

5.5 Discussion

Monzogranite in the study area shows evidence of D_1 and D_2 events, indicating that the granite was emplaced prior to D_1. Monazite data from metasediments on Southampton Island yield ages of *ca.* 1880 Ma and *ca.* 1850 Ma for D_1 and D_2, respectively. Inclusions of monazite in garnet are dated at *ca.* 1880 Ma, most likely representing the timing of near-peak metamorphism (N. Rayner, R. Berman, M. Sanborn-Barrie *pers. comm.* 2008). Monzogranite intruded prior to D_1 at granulite-facies conditions, indicating peak metamorphism was pre- or syn-granite intrusion. This places a minimum age of *ca.*1880 Ma for peak metamorphism.

Integration of Ar-Ar data with estimates for the time of peak metamorphism indicates slow cooling from ~850°C to ~580-480°C over at least 100 Ma. This corresponds to a cooling rate of <3.7°C / Ma, suggesting the closure temperature of hornblende in the samples from this study was closer to ~500°C (Harrison 1981). Several tectonic interpretations are possible:

1. Isothermal decompression stops in the mid-crust, where ambient temperatures are relatively high
2. Transit in a channel stops at mid-crustal levels (Jamieson *et al.* 2004)
3. Reheating following initial cooling
4. Intrusion of post-tectonic granites maintained high temperatures

If apparent slow cooling were the product of reheating following the initial cooling, it would be very difficult to detect this and would require a further more detailed study. Based on the evolution of the neighbouring Rae province, the slow cooling may be attributed to case (1), where thrusting stopped during the terminal collision of the THO at ~1820 Ma (St-Onge *et al.* 2007). In this case, isothermal decompression of the units ceased at mid-crustal levels, which remained hot for a relatively long period of time (eg. Jamieson *et al* 2002).

The Committee Bay belt (Fig. 1.1) in the Rae domain contains hornblende with Ar-Ar plateau ages of 1800-1744 Ma from mafic granulites (H. Sandeman *personal communication* 2008). Peak metamorphism at ~1900 Ma indicates that these units cooled relatively slowly, similar to the mafic granulites of this study (Sandeman *et al.* 2004).

Garnet anorthosites display an anomalous younger age, indicating slower cooling than the adjacent mafic granulites. There are several possible explanations to account for a younger age:

1) The garnet-anorthosite resided at lower crustal levels than the mafic granulites and were juxtaposed during a later event;
2) A localized thermal perturbation allowed diffusion of Ar out of the hornblende, resetting the clock;
3) Fluid infiltration from deeper crustal levels brought hot fluids into contact with the amphiboles in the garnet-anorthosite;
4) The hornblende in the garnet anorthosite was more susceptible to diffusion of Ar than the mafic granulites due to unknown compositional or textural factors.

Explanation (1) seems unlikely based on the proximity of the units (within 5km) and there is no field evidence to support this. A localized thermal perturbation (2) also seems unlikely due to the proximity of the samples. There is no field or petrographic evidence to support localized fluid infiltration into the anorthosite (3), and the proximity of the units makes this also unlikely.

The most likely explanation is a difference in diffusion based on the difference in the calculated structural formulae of the garnet anorthosite hornblende and the mafic granulite hornblende (Tab. 3.1). Harrison (1981) demonstrated that the ratio of Fe/Mg had a significant effect on the closure temperature of hornblende. The hornblende in the garnet anorthosite

displays similar Fe/Mg ratios to hornblende in the mafic granulites, but is slightly more K-rich and Al-poor. The organization of the crystal lattice to accommodate these changes may influence the diffusivity of Ar, and could be a possible explanation for the difference in ages. Further study would be needed to confirm this hypothesis.

CHAPTER 6
DISCUSSION

6.1 Introduction

Data from Southampton Island mafic granulites can be used to interpret the tectonic evolution of Southampton Island. Integration of *P-T* and thermochronological data can be combined to produce a pressure-temperature-time (*P-T-t*) path, which can be used to constrain the tectonic evolution of the area. Tectonic processes control the pressures and temperatures experienced by samples from a given region throughout a given time period. *P-T-t* paths are commonly used to determine the sequence and nature of thermal-tectonic processes in a given region (Spear 1995; Jamieson *et al.* 2002, 2004).

6.2 *P-T* estimates

The mafic granulites, garnet clinopyroxenites, and garnet anorthosites show multistage decompression from high- to mid-granulite facies to amphibolite-facies assemblages. The variation in peak metamorphic conditions from samples collected from a small study area can possibly be attributed to the preferential retention of peak-metamorphic compositions by specific mineral assemblages. No quantitative *P-T* estimates of the amphibolite-facies overprint were obtained, however it seems likely that the fluids necessary for retrogression from granulite- to amphibolite-facies assemblages were derived from the crystallization of relatively hot Opx-monzogranite. Polymetamorphic *P-T* conditions, calculated using the TWEEQ method and the RCLC recalculation method (Ch. 4), for various sample types are listed in Table 6.1.

6.3 Peak *P-T*

Peak pressure and temperature conditions suggest mid- to lower-crustal conditions in tectonically thickened orogenic crust. Pressures >12 kbar are equivalent to an approximate depth

Table 6.1 Summary of metamorphic stages and corresponding *P-T* conditions

Lithology	Mafic granulite	Garnet clinopyroxenite	Garnet anorthosite	Relationship to fabrics
Stage 1 Peak *P-T*	11.8 ± 1 kbar 773 ± 50°C	12.1 ± 1 kbar 841 ± 50°C	7.8 ± 1 kbar 735 ± 50°C	≤ 1880 Ma (D_1)
Stage 2 Decompression	8.7 ± 1 kbar 742 ± 50°C	9.2 ± 1 kbar 814 ± 50°C	8.7 ± 1 kbar 764 ± 50°C	≤ 1850 Ma (D_2)
Stage 3 Amphibolite overprint	<742°C	<814°	<735 °C	>1750 Ma or >1720 Ma (pre-syn D_2)

of >36 km, which for temperatures >800°C, are not commonly attained in any setting other than a collisional orogen. Chemically homogenous garnets suggest residence in a high-temperature environment for a sufficient time to erase evidence of growth zoning through volume diffusion (Ch. 3).

6.4 Isothermal Decompression

Isothermal decompression has been documented in a number of granulite terranes (Harley 1988; Elevold *et al.* 2003; Sanborn-Barrie *et al.* 2004; Engvik *et al.* 2007 and *references therein)*. Isothermal decompression can be attributed to several processes:

1. Thrusting and erosion (Spear 1995)
2. Extension with/without erosion (Spear 1995)
3. Lateral flow of mid-orogenic crust from thicker towards thinner crust (Jamieson *et al.* 2004)
4. Decompression with the thermal regime controlled by voluminous post-tectonic granites

The presence of opx-monzogranite as the host of the mafic granulites most likely rules out the possibility of extension facilitating isothermal decompression. Voluminous granitic batholiths in adjacent lithotectonic provinces are typically calc-alkaline, indicating an arc-type

tectonic-affinity. Geochemical analyses, currently in progress, of monzogranite, mafic granulites, and garnet anorthosites will provide a better understanding of the tectonic affinity of these units.

Peak *P-T* conditions >12kbar (~36km depth) at the surface above continental crust of normal thickness (35-40 km) suggest that crustal thickness was >70 km at the time of peak metamorphism. Collisional thickening has been documented to the east and the west of Southampton Island in the WCP and the Baffin-Ungava segment of the THO (St-Onge *et al.* 2007; Berman *et al.* 2007).

The most likely explanation for isothermal decompression of the mafic granulites is thrusting and erosion during orogeny, with the thermal regime possibly controlled by the intrusion of granitic plutons. Further regional-scale geochronology is needed to test this hypothesis.

The prograde path of the mafic granulites is poorly constrained due to the lack of a preserved prograde assemblage for *P-T* estimates, but the protolith may have been a shallow- or deep-seated mafic intrusion that was buried beneath an overthrusting terrane. The presence of minor lecucosome throughout the study area (~5%) may have induced melt-weakening of the crust and facilitated the lateral transport of mid-crustal material in an orogenic setting. Testing either of these possibilities will require more regional-scale geochronological data.

6.5 Thermochronology

Preliminary U-Th-Pb (monazite) data based on textural associations of monazite in metasediments from Southampton Island constrains 2 metamorphic events that texturally suggest syn-tectonic metamorphism. D_1 and M_1 at *ca.* 1880 Ma was determined from monazite inclusions in garnet. D_2 and M_2 at *ca.* 1850 Ma was determined from matrix monazite grains (N. Rayner, R. Berman, M. Sanborn-Barrie, *pers. comm.* 2008). Monzogranites from the study areas

and many localities from Southampton Island display S_1 and S_2 fabrics, indicating that most granite intrusion was pre- or syn-D_1.

The mafic granulites cooled through 500°C by *ca.* 1750 Ma (Ch.5). This indicates relatively slow cooling from peak-T (~850°C) at a rate of <3.5°C/ Ma (Fig. 6.1). Slow cooling probably reflects prolonged residence after tectonic transport to mid-crustal levels.

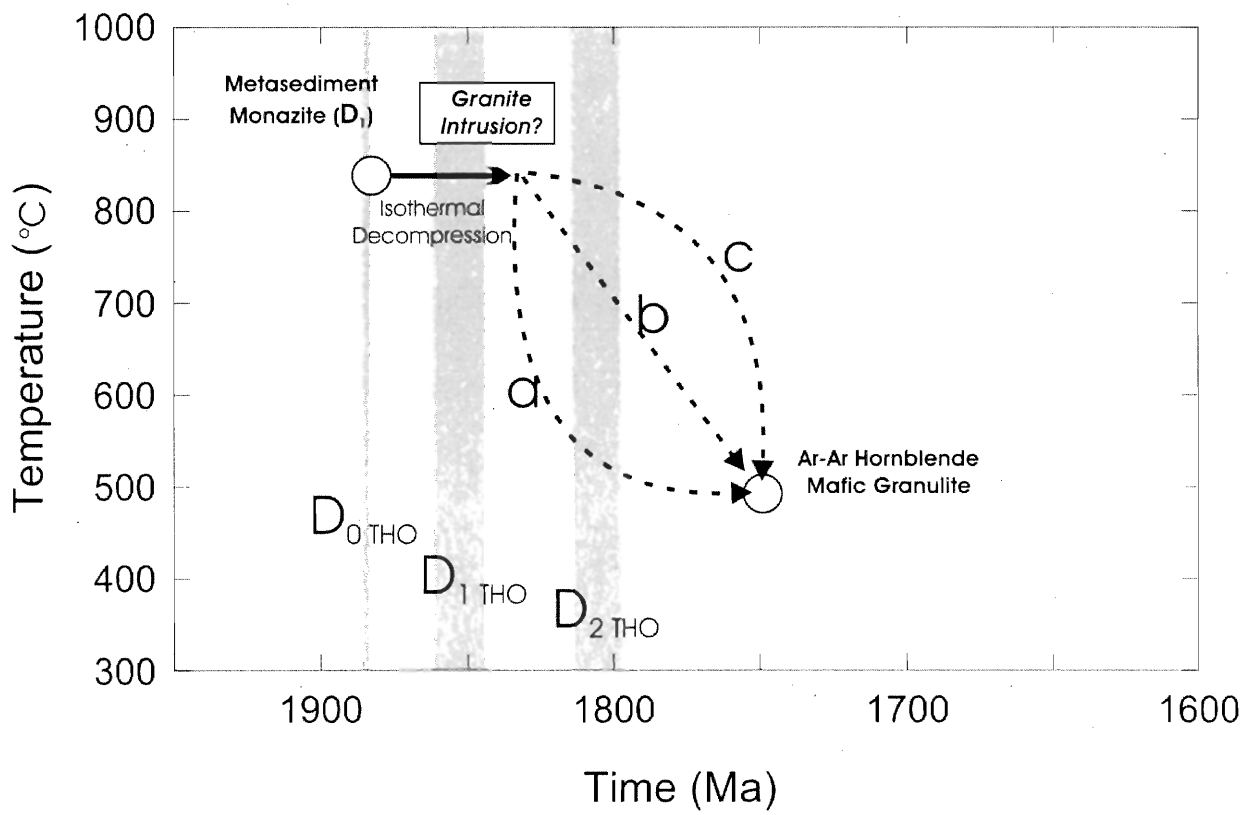

Figure 6.1. Integration of monazite data interpreted to represent D_1 in pelitic metasediments, Ar-Ar from mafic granulites (Ch.5), overlain with deformation episodes of the Trans-Hudson Orogen (St-Onge *et al.* 2007). Multiple cooling paths are inferred and discussed in the text.

Figure 6.1 displays three simple *T-t* paths correspond to different possible cooling histories for the mafic granulites. In case (a), relatively rapid cooling at ~1880 Ma is followed by progressively slower cooling until ~1750 Ma. Case (a) is indicative of thrusting and erosion, which would transport lower-crustal rocks into the upper-crust in a relatively short period of

time. To cool this rapidly, granite intrusion needs to pre-date D_1. This model indicates isothermal decompression at cool conditions, which does not fit the relatively hot near-isothermal decompression data from *P-T* estimates (Ch.4).

Case (b) is the simplest case in which cooling from peak-*T* to ~500°C was at a constant rate. This model also requires the granite intrusion pre-D_2 to produce an unperturbed thermal regime following peak-*T*. This model is consistent with slow cooling at moderate erosion rates in order for cooling to remain constant with time.

In case (c), high temperatures persist followed by relatively late rapid cooling later in the tectonic history. This interpretation is consistent with peak metamorphism pre-dating granite intrusion. This model is consistent with the limited constraints available for isothermal decompression to mid-crustal depths followed by relatively rapid cooling. Relatively rapid cooling could be the product of post-intrusion coeval thrusting and erosion or the lateral movement of mid-orogenic crust to the near-surface coupled with erosion.

6.6 Tectonic setting of metamorphism

The protolith of the Southampton Island mafic granulites is not yet constrained, but the presence of Ti-rich clinopyroxene in a silica-undersaturated matrix may suggest an alkaline mafic intrusion, possibly forming during a period of intracontinental extension (Winter 2001).

The *P-T* histories of the mafic granulites and garnet clinopyroxenites document crustal thickening, a residence period at high temperatures sufficient to homogenize garnets (Ch. 3), isothermal decompression, and relatively slow cooling. The most likely tectonic settings that would induce this sequence of events are a collisional orogen that produced significant crustal

thickening through thrusting and the emplacement of syn- to post-tectonic mid-crustal granites, or the accretion of an arc-type terrane that would produce crustal thickening.

6.7 Analogues

Mineralogical evidence from this study points to a silica-undersaturated protolith, possibly related to intracontinental rifting. Flowers *et al.* (2006) proposed that the Snowbird Tectonic Zone experienced a period of extension at *ca.* 1.9 Ga, based on the presence of mafic intrusions of that age. The extent of the STZ towards Southampton Island is not well constrained, but the emplacement of mafic granulites in the study area may have been associated with a period of extension in the eastward continuation of the STZ. Geochemistry of the mafic units will help test this hypothesis.

Analogous lithologies in the WCP include the Kramanituar Complex (Rae Province), which experienced similar peak *P-T* conditions of 12.5 ± 1.5 kbar and 810 ± 70°C, followed by isothermal decompression and relatively rapid cooling (>450°C / Ma). This sequence of events was attributed to extensional unroofing (± erosion) at *ca.* 1.90 Ga as a far-field response to the collision of the Slave and Churchill provinces ~1.97-1.90 Ga (Sanborn-Barrie *et al.* 2001).

In contrast with this study, rapid cooling of the Kramanituar Complex at *ca.* 1908-1898 Ma at rates >450°C / Ma has been documented (Sanborn-Barrie *et al.* 2001). Along-strike variations in cooling rates are not uncommon in many orogenic belts, and may be responsible for the observed differences. Despite the inferred difference in cooling rates, the overall similarity between the tectonometamphic evolution of the mafic granulites from the Kramanituar Complex and from this study indicates that Southampton Island may be an eastward continuation of the Rae Province.

Ar-Ar ages of hornblende from the Committee Bay region (Rae province) (Fig. 1.1) show slow cooling through ~500°C at *ca.* 1750 Ma (H. Sandeman *pers comm.* 2008). This indicates a possible correlation in cooling histories from part of the Rae province and Southampton Island.

On Baffin Island, the Cumberland batholith was emplaced at *ca.* 1865-1848 Ma in response to north-vergent subduction beneath Meta-Incognita. Similar voluminous monzogranites to granodiorites comprise most of Southampton Island, although there are currently no crystallization ages. If the Soper River suture transects southwestern Southampton Island (Fig. 1.1), it seems reasonable that the granitoids that comprise most of the island are analogous to the Cumberland Batholith. This indicates that Southampton Island may lie in the centre of a Paleoproterozoic arc that extends for >10 000 km from the Wathman Batholith in the southwest to the Cumberland Batholith in the northeast.

Units from Baffin-Ungava segment of the THO show peak metamorphism <10 kbar and <750°C at ~1850 Ma (St-Onge *et al* 2007), significantly less than peak estimates from this study. This indicates that Southampton Island is most likely not part of the Meta-Incognita microcontinent, or that there were significant along-strike variations in peak *P-T* conditions.

Southampton Island may also be a remnant of a microcontinent that shared a similar tectonometamorphic history to the Rae Province. Berman *et al.* (2007) allude to the possibility a Hudsonian proto-continent that may have been involved in THO but was subsequently been rifted off. U-Pb geochronology of the basement units of Southampton Island would test this hypothesis.

Later subduction-driven tectonic thickening in response to the collision between the Chesterfield and Hearne blocks at *ca.* 1.90 Ga (Berman *et al.* 2007) may be responsible for D_2 or the 1.88-1.865 Ga collision between Meta-Incognita and the Rae Province (St-Onge *et al.* 2007).

D_3 on Southampton Island is characterized by km-scale open folds that strongly resembles similar structures from southwest Baffin Island, probably attributed to the terminal collision of the THO at *ca.* 1820-1795 (St-Onge *et al.* 2007).

6.8 Conclusions

Integrating possible analogues from adjacent provinces, it seems likely that Southampton Island is a southeastern extension of the Rae Province of the WCP that was subsequently affected by regional tectonic processes associated with the THO. It shares a similar cooling history to the Committee Bay region and similar peak *P-T* conditions to the Kramanituar complex, Rae province. The voluminous orthopyroxene-bearing granitoids that comprise most of Southampton Island are analogous to the Cumberland Batholith of Baffin Island, indicating an arc-type setting associated with north-vergent subduction beneath Meta-Incognita and the Rae Province (Fig. 6.2). The polydeformational history of Southampton Island and the tectonic setting will be further constrained by in progress U-Pb geochronology of various lithologies.

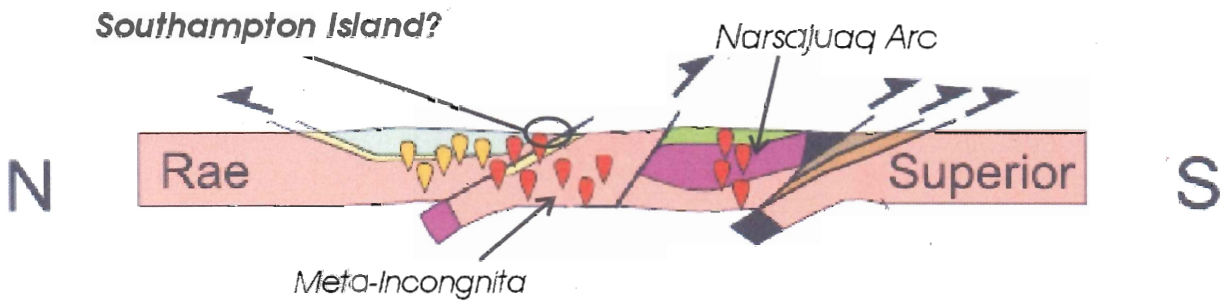

Figure 6.2. Possible tectonic setting of Southampton Island as the leading edge of the Rae Province (after St-Onge *et al.* 2007). Post-tectonic calc-alkaline magmatism abundant in Meta-Incognita and possibly on Southampton Island.

CHAPTER 7
CONCLUSIONS

7.1 Conclusions

1. Mafic granulites, which represent a small proportion (<1%) of the total rocks on Southampton Island, intruded metasediments of unknown age, and are intruded by orthopyroxene-bearing monzogranites.
2. Equilibrated assemblages in specific textural domains preserve a polymetamorphic history of the mafic granulties characterised by: (i) peak metamorphism at 12-14 kbar and 750-850°C, (ii) near-isothermal decompression from high- to mid-pressure granulite facies at 8-10 kbar and 750-800°C, and (iii) amphibolite facies overprinting at < 750°C
3. $^{40}Ar/^{39}Ar$ step-heating of hornblende yielded an age of 1750 ± 12 Ma for mafic granulites and 1720 ± 12 Ma for garnet anorthosites, indicating relatively slow cooling from peak metamorphic conditions.
4. *P-T-t* evolution is consistent with: (i) crustal thickening, (ii) extended residence at mid-crustal depths with the thermal regime facilitated by granite emplacement and peak-metamorphism, and (iii) exhumation facilitated by thrusting and erosion.
5. *P-T* estimates from mafic granulites are similar to the Kramanituar Complex in the Rae craton to the west, indicating Southampton Island may be part of the southeastern continuation of the Rae craton

7.2 Recommendations for further study

Improved understanding of the tectonostratigraphic significance of coronitic mafic granulites from Southampton Island will require a combination of geochronology and geochemistry.

Studies underway using U-Pb geochronology, detrital zircons from metasediments will provide information on the maximum age of deposition, provenance, and provide a maximum age on the intrusion of the mafic granulites. Zircons from surrounding granitoid rocks will provide a minimum age for the mafic granulites and may be chronologically compared with similar granitic batholiths in surrounding terranes. Zircons from the mafic granulites may provide a date of peak metamorphism, age of the protolith, crystallization date, and possibly date metamorphic events that affected the mafic granulites.

Bulk chemical analysis using X-ray Fluorescence or similar methods may be crucial to narrowing the errors in P-T estimates. The construction of a pseudosection using these data will provide a more accurate estimation of the *P-T* path of the mafic granulites. Rare earth element data from the mafic granulites may provide a geochemical signature indicative of a specific tectonic setting and provide an indication of possible protoliths.

REFERENCES

Baldwin, J.A., Bowring, S.A., Williams, M.L. 2003. Petrological and geochronological constraints on high pressure, high temperature metamorphism in the Snowbird Tectonic Zone, Canada. Journal of Metamorphic Geology, **21**: 81-98.

Berman, R.G., 1991. Thermobarometery using multi-equilibrium calculations: a new technique with petrological implications. Canadian Mineralogist **29**: 833-855.

Berman, R.G. 2007. winTWQ (version 2.3): a software package for performing internally-consistant thermobarometric calculations. Geological Survey of Canada, Open File 5462, ed. 2.32.

Berman, R.G. and Aranovich, L.Y. 2007. *In Preperation.* Mixing properties of selected minerals: winTWQ v. 2.34.

Berman, R.G., Aranovich, L.Y., and Pattison. D. 1995. Reassessment of the garnet-clinopyroxene Fe-Mg exchange thermometer: II. Thermodynamic analysis. Contributions to Mineralogy and Petrology, **119**: 30-42.

Berman, R.G., Davis, W.J., Pehrsson, S. 2007. Collisional Snowbird tectonic zone resurrected: Growth of Laurentia during the 1.9 Ga accretionary phase of the Hudsonian orogeny. Geology, **35**: 911-914.

Berman, R.G., Sanborn-Barrie, M., Stern, R.A., and Carson, C.J. 2005. Tectonometamorphism at *ca.* 2.35 and 1.85 Ga in the Rae domain, Western Churchill Province, Nunavut, Canada: Insights from structural, metamorphic and *in situ* geochronological analysis of the southwestern Committee Bay belt. The Canadian Mineralogist, **43**: 409-442.

Cygan, R.T., and Lasaga, A.C. 1985. Self-diffusion of Mg in garnet at 750°C to 900°C. American Journal of Science, **285**: 328-350.

Davis, W.J., Hanmer, S., Tella, S., Sandeman, H., and Ryan, J.J. 2006. U-Pb geochronology of the MacQuoid supracrustal belt and Cross Bay plutonic complex: Key components of the northwestern Hearne subdomain. Western Churchill Province, Nunavut, Canada. Precambrian Research, **145**: 53-80.

Deer, W.A., Howie, R.A., and Zussman, J. 1996. An Introduction to the Rock-Forming minerals (2^{nd} edition). Prentice Hall, New Jersey, 712pp.

Dickin, A.P. 2004. Radiogenic Isotope Geology, 2^{nd} edition. Cambridge University Press, Cambridge, UK.

Dodson, M.H. 1973. Closure temperature in cooling geochronological and petrological systems. Contributions to Mineralogy and Petrology, **40:** 259-274.

Elevold, S., Thrane, K. and Gilotti, J.A. 2003. Metamorphic history of high-pressure granulites in Payer Land, Greenland Caledonides. Journal of Metamorphic Geology, **21**: 49-63.

Engvik, A.K., Tvetem, E., Bingen, B., Viola, G., Erambert, M., Feito, P., and De Azavedo, S. 2007. P-T-t evolution and textural evidence for decompression of Pan-African high-pressure granulites, Lurio Belt, north-eastern Mozambique. Journal of Metamorphic Geology **25**: 935-952.

Flowers, R.M., Bowring, S.A., and Williams, M.L. 2006. Timescales and significance of high-pressure, high-temperature metamorphism and mafic dyke anatexis, Snowbird tectonic zone, Canada. Contributions to Mineralogy and Petrology, **151**: 558-581.

Fuhrman, M.L. and Lindsley, D.H. 1988. Ternary-feldspar modeling and thermometry. The American Mineralogist, **73**: 201-216.

Grant, S.M. 1988. Diffusion models for corona formation in metagabbros from the Western Grenville province, Canada. Contributions to Mineralogy and Petrology, **98**: 49-63.

Harley, S.L. 1988. Proterozoic granulites from the Rauer Group, East Anarctica. I. Decompressional pressure-temperature paths deduced from mafic and felsic gneisses. Journal of Petrology, **29**: 1059-1095.

Harley, S.L. 1989. The origin of granulites: a metamorphic perspective. Geological Magazine, **126**: 215-331.

Harrison, T.M. 1981. Diffusion of ^{40}Ar in hornblende. Contibutions to mineralogy and petrology, **78**: 324-331.

Heywood, W.W. and B.V. Sanford. 1976, Geology of Southampton, Coats, and Mansel Islands, District of Keewatin, Northwest Terretories. Geological Survey of Canada, Memoir 382.

Holland, T., and Blundy, J. 1994. Non-ideal interactions in calcic amphiboles and their bearing on amphibole-plagioclase thermometry. Contributions to Mineralogy and Petrology, **116**: 433-447.

Indares, A. 2003. Metamorphic tectures and *P-T* evolution of high-*P* granulites from the Lelukuau terrane, NE Grenville Province, Journal of metamorphic Geology, **21**: 35-48.

Jamieson, R.A., Beaumont, C., Medvedev, S. and Nguyen, M.H. 2004. Crustal channel flows: 2. Numerical models with implications for metamorphism in the Himalayan-Tibetan orogen. Journal of Geophysical Research, **109**: B06407, doi:10.1029/2003JB002811.

Jamieson, R.A., Beaumont, C., Nguyen, M.H. and Lee, B. 2002. Interaction of metamorphism, deformation, and exhumation in large convergent orogens. Journal of Metamorphic Geology, **20**: 9-24.

Kretz, R. 1983. Abbreviations for rock-forming minerals. American Mineralogist, **68**: 277-279.

Mahan, K.H., and Williams, M.L. 2005. Reconstruction of a large deep-crustal terrane: Implications for the Snowbird Tectonic Zone and early growth of Laurentia. Geology, **33**: 385-388.

Martel, E., van Breemen, O., Berman, R.G., and Pehrsson, S. *In Press*. Geochronology and tectonometamorphic history of the Snowbird Lake area, Northwest Territories, Canada: New insights into the architecture and significance of the Snowbird tectonic zone. Precambrian research, doi: 10.1016/j.precamres.2007.07.007.

McDougall, I. and Harrison, T.M. 1999. Geochronology and Thermochronology by the $^{40}Ar/^{39}Ar$ Method, *second edition.* Oxford University Press, Inc. New York.

Nakano, N., Osanai, Y., Owada, M., Nam, T.N., Tsunogae, T., Toyoshima, T., and Binh, P. 2004. Decompression process of mafic granulite from eclogite to granulite facies under ultrahigh-temperature condition in the Kontum massif, central Vietnam. Journal of Mineralogical and Petrological Sciences, **99**: 242-256.

O'Brien, P.J. and Rötzler, J. 2003. High-pressure granulites: formation, recovery of peak conditions and implications for tectonics. Journal of Metamorphic Geology **21**: 3-20.

Passchier, C.W. and Trouw, R.A.J. 2005. Microtectonics. Springer, Berlin Heidelber New York.

Pattison, D.R.M. 2003. Petrogenetic significance of orthopyroxene-free garnet + clinopyroxene + plagioclase ± quartz-bearing metabasites with respect to amphibolite and granulite facies. Journal of Metamorphic Geology, **21**: 21-34.

Pattison, D.R.M., Chacko, T., Farquhar, J., and C.R.M. McFarlen. 2003. Temperatures of Granulite-facies metamorphism: constraints from experimental phase equilibria and thermobarometery corrected for retrograde exchange.

Peterson, T.D., Van Breeman, O., Sandeman, H., and Cousens, B. 2002. Proterozoic (1.85-1.75 Ga) igneous suites of the Western Churchill Province: granitoid and ultrapotassic magmatism in t\ a reqorked Archean hinterland. Precambrian Reseacrch, **119**: 73-100.

Roksandic, M.M., Beaumont, C., and Tankard, A.J. 1987. The tectonics and evolution of the Hudson Bay region. Atlantic Geoscience Society Special Publication **5**, 507-518.

Ross G.M., Eaton D.W., Boerner D.E., and Miles, W. 2000 Tectonic entrapment and its role in the evolution of continental lithosphere: an example from the Precambrian of western Canada. Tectonics, **19**:116–134

Sanborn-Barrie, M. and Berman, R.G. 2007. SWBIG in a western Chruchill context. Southwest Baffin Island Integrated Geoscience Project Workshop.

Sanborn-Barrie, M., Carr, S., and Thériault, R. 2001. Geochronological constraints on metamorphism, magmatism and exhumation of deep-crustal rocks of the Kramanituar Complex, with implications for the Paleoproterozoic evolution of the Archean western Churchill Province, Canada. Contributions to Mineralogy and Petrology, **141**. 592-612.

Sanborn-Barrie, M., Chakungal, J., James, D., Whalen, J., Zhang, S., Ross, M., Berman, R., Rayner, N., and Gilbert, C. 2008. A new understanding of Southampton Island, Nunavut, in a Northeast Laurentia Context. Poster presentation at the Mineral Exploration Roundup, 2008.

Sandeman, H.A., Hanmer, S., Davis, W.J., Ryan, J.J., and Peterson, T.D. Neoarchean volcanic rocks, Central Hearne supracrustal belt, Western Churchill Province, Canada: geochemical and isotopic evidence supporting intra-oceanic, supra-subduction zone extension. Journal of Precambrian Research, **134**: 113-141.

Spear, F.S. 1995. Metamorphic phase equilibria and pressure-temperature-time paths. Mineralogical Society of America monograph, Wahington, D.C., 799pp.

St-Onge, Ijewliw, O.J., and Wodicka, N.R. 2007. Polymetamorphic Evolution of the Trans-Hudson Orogen, Baffin Island, Canada: integration of Petrological, Structural, and geochronological data. Journal of Petrology, **48**: 271-302.

St-Onge, M.R., and Ijewliw, O.J. 1996. Mineral corona formation during high-P retrogression of Granulite Rocks, Ungava Orogen, Canada. Journal of Petrology, **37**: 553-582.

St-Onge, M.R., Scott, D.J., and Wodicka, N. 2002. Review of crustal architecture and evolution in the Ungava Peninsula-Baffin Island area: connection to the Lithoprobe ECSOOT transect. Canadian Journal of Earth Sciences, **39**: 589-610.

Thost, D.E., Hensen, B.J., and Motoyoshi, Y. 1991. Two-stage decompression in garnet-bearing mafic granulites from Sostrene Island, Prydz Bay, East Antarctica. Journal of Metamorphic Geology, **9**: 245-256.

van Breeman, O., Harper, C.T., Berman, R.G., and Wodicka, N. 2007. Crustal architecture and Neoarchean assembly of the central-southern Hearne domains: Evidence from U-Pb geochronology and Sm-Nd isotopes of the Phelps Lake area, northeastern Saskatchewan. Precambrian Research, **159**: 33-59.

Winter, J.D. 2001. An Introduction to Igneous and Metamorphic Petrology. Prentice Hall: New Jersey, 697 pp.

APPENDIX A
MINERAL CHEMICAL DATA

Chemical analyses of minerals from selected samples were collected on November 8-11, 2007 at the R.M. MacKay Electron Microprobe Laboratory, Dalhousie University, Halifax, Nova Scotia. Analyses were conducted with a 20nA beam with a 15kV accelerating voltage. A standard counting time of 40s for each point was conducted. Standards were calculated every 50 points using the minerals in table A.1

Table A.1 Mineral standards used for Electron Microprobe Analysis

Element	Standard Name
K_2O	Sanadine
Cr_2O_3	Cr Metal
Na_2O	Jadeite
Al_2O_3	Sanidine
MnO	Pyrolusite
CaO	K Kaersutite
TiO_2	K Kaersutite
MgO	K Kaersutite
SiO_2	Sanidine
FeO	Garnet 12442

Mineral data are organised as follows:

Each mineral data set is organised by sample then by textural association:

C: Corona
I: Inclusion
M: Matrix
S: Symplectite
?: Unsure

Corresponding BSE images can be found in Appendix B.

Mineral	Cpx	Cpx	Cpx	Cpx	Cpx	Cpx	Cpx	Cpx	Cpx	Cpx	Cpx	Cpx	Cpx
Analysis	357	359	177	181	295	307	309	291	313	314	128	129	130
Type	M	M	M?	M?	C	C	C	M	M	M	C	C	C
BSE Image	?	?	5B-2	5B-2	5C-2	5C-3	5C-3	5C-1	5C-4	5C-4	5D-5	5D-5	5D-5
SiO_2	50.62	50.25	49.58	47.40	50.28	47.79	50.23	50.13	50.00	50.13	50.25	51.45	50.72
TiO_2	0.40	0.51	0.44	0.41	0.08	0.05	0.12	0.22	0.14	0.20	0.12	0.05	0.08
Al_2O_3	3.43	3.64	4.28	4.01	2.30	2.08	2.80	3.48	1.94	2.32	3.20	1.32	2.87
FeO	7.75	7.49	7.56	7.56	9.46	9.16	9.66	10.56	9.45	9.90	9.41	9.42	9.40
MgO	13.53	13.55	13.17	13.55	13.19	13.05	12.90	12.86	13.10	12.96	12.19	13.05	12.12
CaO	23.19	23.09	23.48	23.31	22.60	23.43	22.64	21.47	22.94	22.70	21.92	22.36	21.89
Na_2O	0.56	0.55	0.42	0.41	0.39	0.37	0.46	0.60	0.48	0.49	0.41	0.27	0.41
	99.73	99.29	99.17	96.90	98.65	96.27	99.15	99.70	98.28	98.95	97.91	98.21	97.88
Si	1.90	1.89	1.87	1.84	1.92	1.88	1.91	1.90	1.92	1.91	1.92	1.97	1.94
Ti	0.01	0.01	0.01	0.01	0.00	0.00	0.00	0.01	0.00	0.01	0.00	0.00	0.00
Al	0.15	0.16	0.19	0.18	0.10	0.10	0.13	0.16	0.09	0.10	0.14	0.06	0.13
Fe	0.24	0.24	0.24	0.25	0.30	0.30	0.31	0.33	0.30	0.32	0.30	0.30	0.30
Mg	0.76	0.76	0.74	0.78	0.75	0.77	0.73	0.73	0.75	0.74	0.70	0.74	0.69
Ca	0.93	0.93	0.95	0.97	0.92	0.99	0.92	0.87	0.94	0.93	0.90	0.92	0.90
Na	0.04	0.04	0.03	0.03	0.03	0.03	0.03	0.04	0.04	0.04	0.03	0.02	0.03
	4.04	4.04			4.04	4.08	4.04	4.05	4.05	4.05	4.01	4.01	4.01
X_{Di}	75.66	76.30	75.66	76.15	71.32	71.76	70.40	68.46	71.21	70.01	69.80	71.19	69.65
X_{He}	24.34	23.70	24.34	23.85	28.68	28.24	29.60	31.54	28.79	29.99	30.20	28.81	30.35

Structural Formulae calculated on the basis of 6(O)

Type; i: inclusion m: matrix c: corona

X_{Di} = 100Mg/(Mg+Fe) X_{He} = 100Fe/(Mg+Fe)

Mineral	Cpx	Cpx	Cpx	Cpx	Cpx	Cpx	Cpx	Cpx	Cpx	Cpx	Cpx	Cpx	Cpx
Analysis	135	136	165	166	167	168	140	144	112	115	75	411	184
Type	C	C	C	C	C	C?	M	M	C	C	M	M	M
BSE Image	5D-5	5D-5	5D	5D	5D	5D	5D	5D2	7A-9	7A-9	7A-5	?	7B-1
SiO_2	49.91	49.54	50.49	49.67	50.06	49.81	48.64	50.62	50.87	51.01	51.34	51.51	50.00
TiO_2	0.37	0.37	0.17	0.25	0.24	0.31	0.23	0.21	0.19	0.13	0.00	0.16	0.11
Al_2O_3	3.74	3.91	2.61	2.76	2.72	3.24	2.96	3.23	2.06	1.44	1.49	1.59	1.81
FeO	8.49	8.35	10.33	10.10	11.94	10.33	10.10	9.34	9.49	9.63	9.36	9.46	9.65
MgO	12.08	13.14	12.39	12.42	12.88	12.26	12.31	12.90	12.02	12.79	13.14	13.30	12.96
CaO	22.13	23.56	22.85	23.38	20.29	22.74	22.71	23.22	21.47	21.98	22.76	23.29	23.14
Na_2O	0.35	0.80	0.44	0.44	0.38	0.44	0.41	0.40	0.39	0.34	0.35	0.35	0.37
	97.28	99.84	99.53	99.23	98.82	99.42	97.60	100.19	96.94	97.73	98.61	100.03	98.26
Si	1.92	1.87	1.92	1.90	1.91	1.89	1.89	1.90	1.97	1.96	1.95	1.94	1.92
Ti	0.01	0.01	0.00	0.01	0.01	0.01	0.01	0.01	0.01	0.00	0.00	0.00	0.00
Al	0.17	0.17	0.12	0.12	0.12	0.15	0.14	0.14	0.09	0.06	0.07	0.07	0.08
Fe	0.27	0.26	0.33	0.32	0.38	0.33	0.33	0.29	0.31	0.31	0.30	0.30	0.31
Mg	0.69	0.74	0.70	0.71	0.73	0.70	0.71	0.72	0.69	0.73	0.75	0.75	0.74
Ca	0.91	0.95	0.93	0.96	0.83	0.93	0.94	0.93	0.89	0.91	0.93	0.94	0.95
Na	0.03	0.06	0.03	0.03	0.03	0.03	0.03	0.03	0.03	0.03	0.03	0.03	0.03
	4.00	4.07	4.04	4.05	4.03	4.04	4.05	4.04	4.00	4.02	4.03	4.04	4.05
X_{Di}	71.73	73.73	68.10	68.69	65.81	67.94	68.49	71.12	69.31	70.29	71.44	71.48	70.54
X_{He}	28.27	26.27	31.90	31.31	34.19	32.06	31.51	28.88	30.69	29.71	28.56	28.52	29.46

Structural Formulae calculated on the basis of 6(O)

Type; i: inclusion m: matrix c: corona

X_{Di} = 100Mg/(Mg+Fe) X_{He} = 100Fe/(Mg+Fe)

Mineral	Cpx	Cpx	Cpx	Cpx	Cpx	Cpx	Cpx	Cpx	Cpx	Cpx	Cpx	Cpx	Cpx
Analysis	146	148	149	246	248	383	217	194	227	331	316	350	351
Type	M	M	M	I	I	M	C	M	I	C	M	M	M
BSE Image	5D-2	5D-2	5D-2	5D	5D	?	8A-2	8A-1	8A-3	?	8B-1	8C-2	?
SiO_2	50.35	49.81	48.85	50.46	49.89	51.87	49.50	51.36	48.23	49.56	50.27	51.08	50.99
TiO_2	0.13	0.17	0.33	0.25	0.40	0.18	0.41	0.27	0.47	0.39	0.37	0.10	0.11
Al_2O_3	2.60	2.71	3.84	2.63	5.28	1.64	4.58	2.59	4.59	4.71	3.88	2.29	2.32
FeO	9.00	9.19	10.07	9.40	14.01	9.71	8.56	8.28	7.26	8.11	7.95	7.48	7.62
MgO	13.06	12.99	12.00	13.28	14.52	13.31	12.70	14.04	13.75	12.79	13.18	14.11	14.08
CaO	22.98	23.31	22.95	22.92	12.04	22.92	23.32	23.47	23.46	23.27	23.28	23.47	23.50
Na_2O	0.37	0.38	0.44	0.39	0.52	0.38	0.44	0.42	0.43	0.45	0.47	0.36	0.35
	98.78	98.81	98.80	99.54	97.08	100.22	99.79	100.65	98.37	99.52	99.63	99.18	99.28
Si	1.92	1.90	1.87	1.91	1.91	1.95	1.86	1.91	1.84	1.86	1.89	1.92	1.92
Ti	0.00	0.00	0.01	0.01	0.01	0.01	0.01	0.01	0.01	0.01	0.01	0.00	0.00
Al	0.12	0.12	0.17	0.12	0.24	0.07	0.20	0.11	0.21	0.21	0.17	0.10	0.10
Fe	0.29	0.29	0.32	0.30	0.45	0.30	0.27	0.26	0.23	0.26	0.25	0.24	0.24
Mg	0.74	0.74	0.69	0.75	0.83	0.74	0.71	0.78	0.78	0.72	0.74	0.79	0.79
Ca	0.94	0.95	0.94	0.93	0.49	0.92	0.94	0.94	0.96	0.94	0.94	0.95	0.95
Na	0.03	0.03	0.03	0.03	0.04	0.03	0.03	0.03	0.03	0.03	0.03	0.03	0.03
	4.04	4.05	4.05	4.04	3.98	4.03	4.04	4.04	4.06	4.04	4.04	4.04	4.04
X_{Di}	72.12	71.61	67.98	71.60	64.88	70.95	72.56	75.14	77.16	73.78	74.71	77.09	76.70
X_{He}	27.88	28.39	32.02	28.40	35.12	29.05	27.44	24.86	22.84	26.22	25.29	22.91	23.30

Structural Formulae calculated on the basis of 6(O)
Type; i: inclusion m: matrix c: corona
X_{Di} = 100Mg/(Mg+Fe) X_{He} = 100Fe/(Mg+Fe)

Mineral	Cpx
Analysis	354
Type	M
BSE Image	8C-2
SiO_2	49.84
TiO_2	0.31
Al_2O_3	3.91
FeO	7.78
MgO	13.10
CaO	23.42
Na_2O	0.43
	99.06
Si	1.88
Ti	0.01
Al	0.17
Fe	0.25
Mg	0.74
Ca	0.95
Na	0.03
	4.04
X_{Di}	75.00
X_{He}	25.00

Structural Formulae calculated on the basis of 6(O)
Type; i: inclusion m: matrix c: corona
X_{Di} = 100Mg/(Mg+Fe) X_{He} = 100Fe/(Mg+Fe)

Mineral	Opx	Opx	Opx	Opx	Opx	Opx	Opx	Opx	Opx	Opx	Opx
Analysis	15	16	17	18	32	358	360	387	388	35	36
Type	C	C	C	C	M	M	M	M	M	I	I
BSE Image	5A-1	5A-1	5A-1	5A-1	5A-2	5A	5A	5A	5A	5A-3	5A-3
SiO_2	50.43	50.68	50.94	50.53	51.31	52.47	52.74	51.39	51.71	51.20	51.78
TiO_2	0.03	0.08	0.07	0.04	0.05	0.15	0.12	0.04	0.05	0.08	0.09
Al_2O_3	3.26	3.20	2.88	3.35	1.39	1.36	0.95	3.46	2.95	3.42	3.21
FeO	20.51	20.41	20.25	19.82	22.09	21.89	21.93	20.09	19.46	19.47	19.35
MnO	0.45	0.50	0.49	0.45	0.46	0.39	0.42	0.42	0.27	0.26	0.26
MgO	23.31	23.35	23.08	23.59	22.94	23.16	23.49	23.87	24.73	24.33	24.80
CaO	0.34	0.27	0.31	0.32	0.44	0.58	0.51	0.25	0.28	0.17	0.21
	98.42	98.58	98.10	98.18	98.83	100.01	100.21	99.57	99.48	98.98	99.77
Si	1.90	1.90	1.92	1.90	1.94	1.95	1.96	1.90	1.91	1.90	1.91
Ti	0.00	0.00	0.00	0.00	0.00	0.00	0.00	0.00	0.00	0.00	0.00
Al	0.14	0.14	0.13	0.15	0.06	0.06	0.04	0.15	0.13	0.15	0.14
Fe	0.65	0.64	0.64	0.62	0.70	0.68	0.68	0.62	0.60	0.60	0.60
Mn	0.01	0.02	0.02	0.01	0.02	0.01	0.01	0.01	0.01	0.01	0.01
Mg	1.31	1.31	1.30	1.32	1.29	1.28	1.30	1.32	1.36	1.35	1.36
Ca	0.01	0.01	0.01	0.01	0.02	0.02	0.02	0.01	0.01	0.01	0.01
	4.03	4.03	4.02	4.03	4.03	4.02	4.02	4.02	4.02	4.02	4.02
X_{En}	66.95	67.10	67.00	67.96	64.93	65.35	65.65	67.92	69.38	69.01	69.54
X_{Fe}	33.05	32.90	33.00	32.04	35.07	34.65	34.35	32.08	30.62	30.99	30.46

Structural Formulae calculated on the basis of 6(O)
Type; i: inclusion m: matrix c: corona
X_{En} = 100Mg/(Mg+Fe) X_{Fe} = 100Fe/(Mg+Fe)

Mineral	Opx	Opx	Opx	Opx	Opx	Opx	Opx	Opx	Opx	Opx	Opx
Analysis	377	379	170	175	179	180	271	274	277	278	282
Type	I	I	C	C	C	C	C	C	C	C	C
BSE Image	5A-4	5A-4	5B-1	5B-1	5B-2	5B-2	5B-5	5B-5	5B-5	5B-6	5B-6
SiO_2	51.39	51.71	46.78	49.34	46.83	48.40	50.66	51.36	51.11	50.99	50.48
TiO_2	0.04	0.05	0.02	0.03	0.00	0.05	0.02	0.02	0.03	0.03	0.00
Al_2O_3	3.46	2.95	3.70	3.51	3.59	2.35	3.33	3.41	3.58	3.62	3.64
FeO	20.09	19.46	20.30	21.19	20.44	21.86	20.33	20.71	20.84	20.01	20.74
MnO	0.42	0.27	0.49	0.51	0.51	0.60	0.47	0.57	0.51	0.47	0.55
MgO	23.87	24.73	23.15	22.66	22.66	22.06	23.66	23.39	23.43	23.75	23.48
CaO	0.25	0.28	0.29	0.42	0.36	0.46	0.34	0.27	0.32	0.34	0.32
	99.57	99.48	94.75	97.72	94.43	95.81	98.84	99.94	99.84	99.29	99.25
Si	1.90	1.91	1.84	1.88	1.85	1.90	1.90	1.90	1.90	1.90	1.89
Ti	0.00	0.00	0.00	0.00	0.00	0.00	0.00	0.00	0.00	0.00	0.00
Al	0.15	0.13	0.17	0.16	0.17	0.11	0.15	0.15	0.16	0.16	0.16
Fe	0.62	0.60	0.67	0.68	0.68	0.72	0.64	0.64	0.65	0.62	0.65
Mn	0.01	0.01	0.02	0.02	0.02	0.02	0.02	0.02	0.02	0.01	0.02
Mg	1.32	1.36	1.36	1.29	1.34	1.29	1.32	1.29	1.30	1.32	1.31
Ca	0.01	0.01	0.01	0.02	0.02	0.02	0.01	0.01	0.01	0.01	0.01
	4.02	4.02	4.07	4.04	4.07	4.05	4.03	4.03	4.03	4.02	4.03
X_{En}	67.92	69.38	67.01	65.59	66.42	64.27	67.46	66.81	66.70	67.90	66.87
X_{Fe}	32.08	30.62	32.99	34.41	33.58	35.73	32.54	33.19	33.30	32.10	33.13

Structural Formulae calculated on the basis of 6(O)
Type; i: inclusion m: matrix c: corona
X_{En} = 100Mg/(Mg+Fe) X_{Fe} = 100Fe/(Mg+Fe)

Mineral	Opx	Opx	Opx	Opx	Opx	Opx	Opx	Opx	Opx	Opx	Opx
Analysis	232	234	412	239	296	300	303	305	308	290	310
Type	M	M	M	I?	C	C	C	C	C	M	M
BSE Image	5B-3	5B-3	5B	5B	5C-2	5C-2	5C-3	5C-3	5C-3	5C-1	5C-4
SiO_2	49.48	52.32	50.83	50.95	51.03	50.76	50.16	47.57	50.83	51.03	50.21
TiO_2	0.07	0.06	0.06	0.02	0.00	0.00	0.00	0.01	0.00	0.00	0.03
Al_2O_3	2.83	1.73	2.32	3.65	1.09	1.59	1.64	1.58	1.26	1.04	0.94
FeO	21.59	21.99	21.23	19.77	25.45	25.23	25.13	25.49	26.03	27.32	26.63
MnO	0.57	0.59	0.56	0.41	0.85	0.86	0.86	0.86	0.86	0.65	0.68
MgO	23.05	23.20	22.71	24.11	20.38	20.20	20.16	19.78	19.96	19.31	19.53
CaO	0.47	0.46	0.48	0.28	0.48	0.51	0.56	0.54	0.58	0.51	0.57
	98.10	100.41	98.29	99.24	99.30	99.23	98.54	95.88	99.55	99.90	98.63
Si	1.88	1.94	1.92	1.89	1.95	1.94	1.93	1.90	1.95	1.95	1.95
Ti	0.00	0.00	0.00	0.00	0.00	0.00	0.00	0.00	0.00	0.00	0.00
Al	0.13	0.08	0.10	0.16	0.05	0.07	0.07	0.07	0.06	0.05	0.04
Fe	0.69	0.68	0.67	0.61	0.81	0.81	0.81	0.85	0.83	0.88	0.86
Mn	0.02	0.02	0.02	0.01	0.03	0.03	0.03	0.03	0.03	0.02	0.02
Mg	1.31	1.28	1.28	1.34	1.16	1.15	1.16	1.18	1.14	1.10	1.13
Ca	0.02	0.02	0.02	0.01	0.02	0.02	0.02	0.02	0.02	0.02	0.02
	4.05	4.02	4.02	4.03	4.02	4.02	4.03	4.06	4.03	4.02	4.03
X_{En}	65.56	65.29	65.59	68.50	58.79	58.81	58.84	58.05	57.76	55.75	56.66
X_{Fe}	34.44	34.71	34.41	31.50	41.21	41.19	41.16	41.95	42.24	44.25	43.34

Structural Formulae calculated on the basis of 6(O)
Type; i: inclusion m: matrix c: corona
X_{En} = 100Mg/(Mg+Fe) X_{Fe} = 100Fe/(Mg+Fe)

Mineral	Opx	Opx	Opx	Opx	Opx	Opx	Opx	Opx	Opx	Opx	Opx
Analysis	391	392	126	127	131	154	157	158	159	163	143
Type	M	M	C	C	C	C	C	C	C	C	M
BSE Image	5C	5C	5D-1	5D-1	5D-1	5D-3	5D-3	5D-3	5D-3	5D-3	5D-3
SiO_2	51.46	50.90	50.99	50.91	50.81	51.29	51.46	51.55	51.52	50.96	50.88
TiO_2	0.08	0.08	0.00	0.01	0.00	0.01	0.02	0.04	0.00	0.02	0.05
Al_2O_3	1.04	1.03	1.69	1.79	1.96	1.19	1.13	1.59	1.76	2.25	1.20
FeO	25.84	25.81	24.46	25.19	24.82	24.62	24.68	24.68	24.55	23.47	26.21
MnO	0.62	0.61	0.69	0.70	0.68	0.64	0.56	0.59	0.57	0.50	0.55
MgO	19.89	19.88	19.55	19.22	19.06	20.66	20.86	20.91	20.74	20.96	19.52
CaO	0.57	0.56	0.37	0.54	0.40	0.40	0.37	0.41	0.43	0.40	0.61
	99.62	98.96	97.82	98.47	97.80	98.87	99.14	99.86	99.68	98.61	99.09
Si	1.96	1.96	0.33	0.33	0.33	0.33	0.33	0.32	0.32	0.32	0.33
Ti	0.00	0.00	0.00	0.00	0.00	0.00	0.00	0.00	0.00	0.00	0.00
Al	0.05	0.05	0.01	0.01	0.01	0.01	0.01	0.01	0.01	0.02	0.01
Fe	0.82	0.83	0.13	0.14	0.13	0.13	0.13	0.13	0.13	0.12	0.14
Mn	0.02	0.02	0.00	0.00	0.00	0.00	0.00	0.00	0.00	0.00	0.00
Mg	1.13	1.14	0.19	0.18	0.18	0.20	0.20	0.20	0.19	0.20	0.19
Ca	0.02	0.02	0.00	0.00	0.00	0.00	0.00	0.00	0.00	0.00	0.00
	4.01	4.02	0.67	0.67	0.67	0.67	0.67	0.67	0.67	0.67	0.67
X_{En}	57.84	57.87	58.75	57.62	57.79	59.94	60.10	60.16	60.10	61.41	57.02
X_{Fe}	42.16	42.13	41.25	42.38	42.21	40.06	39.90	39.84	39.90	38.59	42.98

Structural Formulae calculated on the basis of 6(O)
Type; i: inclusion m: matrix c: corona
X_{En} = 100Mg/(Mg+Fe) X_{Fe} = 100Fe/(Mg+Fe)

Mineral	Opx	Opx	Opx	Opx	Opx	Opx	Opx	Opx	Opx	Opx	Opx
Analysis	147	151	249	44	51	83	84	85	86	104	107
Type	M	M	I	C	C	C	C	C	C	C	C?
BSE Image	5D-2	5D-2	5D	7A-1	7A-1	7A-6	7A-6	7A-6	7A-6	7A-8	7A-8
SiO_2	50.74	47.59	51.12	51.09	50.94	51.06	50.94	51.34	51.02	50.10	50.33
TiO_2	0.03	0.15	0.06	0.00	0.00	0.06	0.05	0.06	0.05	0.00	0.01
Al_2O_3	1.59	1.98	2.11	2.12	2.37	1.89	1.84	1.82	1.70	1.63	1.47
FeO	24.83	26.08	24.01	22.18	22.65	23.31	22.98	22.94	23.39	22.81	24.74
MnO	0.48	0.53	0.31	0.83	0.98	1.02	1.17	1.23	1.17	1.08	1.06
MgO	20.43	17.85	21.70	21.48	21.52	20.91	20.76	21.21	21.03	20.77	18.41
CaO	0.50	1.28	0.55	0.32	0.30	0.46	0.36	0.40	0.39	0.43	0.39
	98.67	95.70	99.99	98.02	98.77	98.82	98.18	99.09	98.85	96.86	96.49
Si	0.32	0.32	0.32	1.95	1.93	1.94	1.95	1.95	1.94	1.95	1.98
Ti	0.00	0.00	0.00	0.00	0.00	0.00	0.00	0.00	0.00	0.00	0.00
Al	0.01	0.02	0.02	0.10	0.11	0.08	0.08	0.08	0.08	0.08	0.07
Fe	0.13	0.15	0.13	0.71	0.72	0.74	0.74	0.73	0.75	0.74	0.81
Mn	0.00	0.00	0.00	0.03	0.03	0.03	0.04	0.04	0.04	0.04	0.04
Mg	0.19	0.18	0.20	1.22	1.22	1.19	1.18	1.20	1.19	1.20	1.08
Ca	0.00	0.01	0.00	0.01	0.01	0.02	0.01	0.02	0.02	0.02	0.02
	0.67	0.67	0.67	4.01	4.02	4.01	4.01	4.01	4.02	4.02	3.99
X_{En}	59.46	54.97	61.70	63.33	62.87	61.51	61.69	62.22	61.57	61.88	57.02
X_{Fe}	40.54	45.03	38.30	36.67	37.13	38.49	38.31	37.78	38.43	38.12	42.98

Structural Formulae calculated on the basis of 6(O)
Type; i: inclusion m: matrix c: corona
X_{En} = 100Mg/(Mg+Fe) X_{Fe} = 100Fe/(Mg+Fe)

Mineral	Opx	Opx	Opx	Opx	Opx	Opx	Opx	Opx	Opx	Opx	Opx
Analysis	109	111	113	116	64	68	70	72	74	407	408
Type	C	C	C	C?	M	M	M	M	M	M	M
BSE Image	7A-9	7A-9	7A-9	7A-9	7A-4	7A-4	7A-4	7A-5	7A-5	7A	7A
SiO_2	51.08	46.11	50.75	51.14	50.82	50.85	51.12	50.33	51.21	50.44	50.46
TiO_2	0.06	0.08	0.08	0.08	0.00	0.00	0.00	0.00	0.00	0.10	0.09
Al_2O_3	1.13	3.51	1.10	1.00	1.29	1.33	1.20	0.97	0.89	1.21	0.97
FeO	25.55	26.58	26.44	26.88	25.61	25.23	24.92	26.50	26.12	25.10	25.92
MnO	1.00	0.75	0.95	0.98	0.91	0.85	0.86	0.82	0.65	0.86	1.10
MgO	19.07	16.92	18.79	18.16	19.46	19.61	20.00	18.60	19.05	19.78	19.26
CaO	0.59	0.64	0.59	0.54	0.36	0.39	0.39	0.48	0.44	0.69	0.63
	98.50	94.68	98.76	98.87	98.46	98.26	98.49	97.70	98.35	98.35	98.57
Si	1.97	1.88	1.96	1.98	1.96	1.96	1.96	1.97	1.98	1.95	1.95
Ti	0.00	0.00	0.00	0.00	0.00	0.00	0.00	0.00	0.00	0.00	0.00
Al	0.05	0.17	0.05	0.05	0.06	0.06	0.05	0.05	0.04	0.06	0.04
Fe	0.82	0.90	0.86	0.87	0.83	0.81	0.80	0.87	0.84	0.81	0.84
Mn	0.03	0.03	0.03	0.03	0.03	0.03	0.03	0.03	0.02	0.03	0.04
Mg	1.10	1.03	1.08	1.05	1.12	1.13	1.15	1.08	1.10	1.14	1.11
Ca	0.02	0.03	0.02	0.02	0.02	0.02	0.02	0.02	0.02	0.03	0.03
	4.00	4.04	4.01	4.00	4.01	4.01	4.01	4.01	4.00	4.02	4.02
X_{En}	57.09	53.15	55.88	54.64	57.54	58.08	58.87	55.58	56.52	58.41	56.96
X_{Fe}	42.91	46.85	44.12	45.36	42.46	41.92	41.13	44.42	43.48	41.59	43.04

Structural Formulae calculated on the basis of 6(O)
Type; i: inclusion m: matrix c: corona
X_{En} = 100Mg/(Mg+Fe) X_{Fe} = 100Fe/(Mg+Fe)

Mineral	Opx	Opx	Opx	Opx	Opx	Opx	Opx	Opx	Opx	Opx	Opx
Analysis	409	284	399	400	183	186	188	190	288	363	195
Type	M	C	C	C	M	M	M	M	M	M	M
BSE Image	7A	7B	7B	7B	7B-1	7B-1	7B-1	7B-1	7B	7B	8A-1
SiO_2	51.36	50.99	50.10	50.78	49.08	50.28	48.47	49.05	51.36	51.15	51.75
TiO_2	0.06	0.00	0.05	0.04	0.02	0.06	0.05	0.06	0.07	0.10	0.04
Al_2O_3	0.93	1.78	1.77	1.85	0.82	0.82	1.12	0.96	1.22	0.98	1.09
FeO	25.48	23.75	23.73	23.71	26.00	25.83	25.43	25.86	26.53	26.03	23.68
MnO	0.82	1.24	1.20	1.24	0.48	0.50	0.47	0.50	0.58	0.93	0.42
MgO	20.12	20.91	20.32	20.67	19.43	19.74	19.57	19.44	19.75	19.93	21.98
CaO	0.56	0.42	0.45	0.38	0.56	0.48	0.53	0.47	0.51	0.49	0.46
	99.44	99.16	97.76	98.80	96.40	97.74	95.69	96.38	100.06	99.65	99.46
Si	1.96	1.94	1.94	1.94	1.95	1.96	1.93	1.94	1.95	1.95	1.95
Ti	0.00	0.00	0.00	0.00	0.00	0.00	0.00	0.00	0.00	0.00	0.00
Al	0.04	0.08	0.08	0.08	0.04	0.04	0.05	0.05	0.05	0.04	0.05
Fe	0.81	0.76	0.77	0.76	0.86	0.84	0.85	0.86	0.84	0.83	0.75
Mn	0.03	0.04	0.04	0.04	0.02	0.02	0.02	0.02	0.02	0.03	0.01
Mg	1.14	1.19	1.17	1.18	1.15	1.15	1.16	1.15	1.12	1.14	1.24
Ca	0.02	0.02	0.02	0.02	0.02	0.02	0.02	0.02	0.02	0.02	0.02
	4.02	4.02	4.02	4.02	4.04	4.02	4.04	4.03	4.02	4.02	4.02
X_{En}	58.46	61.08	60.41	60.84	57.12	57.66	57.83	57.26	57.03	57.72	62.32
X_{Fe}	41.54	38.92	39.59	39.16	42.88	42.34	42.17	42.74	42.97	42.28	37.68

Structural Formulae calculated on the basis of 6(O)
Type; i: inclusion m: matrix c: corona
X_{En} = 100Mg/(Mg+Fe) X_{Fe} = 100Fe/(Mg+Fe)

Mineral	Opx	Opx	Opx	Opx	Opx	Opx	Opx	Opx	Opx	Opx	Opx
Analysis	205	208	210	212	214	219	225	228	267	263	330
Type	C	C	C	C	C	I	I	I	C	C	C
BSE Image	8A-2	8A-2	8A-2	8A-2	8A-2	8A-3	8A-3	8A-3	8A-4	8A-4	8B
SiO_2	51.03	50.84	51.25	51.61	51.26	53.86	50.19	49.29	51.20	51.46	51.04
TiO_2	0.03	0.02	0.01	0.04	0.03	0.01	0.08	0.06	0.04	0.02	0.05
Al_2O_3	2.15	2.21	1.99	1.62	1.85	1.47	2.99	3.65	2.14	2.06	2.62
FeO	21.78	22.38	22.92	22.85	23.41	15.10	20.04	20.30	23.22	22.73	22.45
MnO	0.50	0.53	0.50	0.50	0.52	0.09	0.30	0.30	0.56	0.52	0.50
MgO	22.43	22.21	22.37	22.10	21.65	28.49	24.23	23.46	21.75	22.37	22.12
CaO	0.43	0.42	0.38	0.49	0.52	0.29	0.35	0.69	0.41	0.35	0.34
	98.44	98.65	99.50	99.22	99.25	99.34	98.23	97.78	99.35	99.59	99.19
Si	1.93	1.93	1.93	1.95	1.94	1.95	1.89	1.87	1.93	1.93	1.92
Ti	0.00	0.00	0.00	0.00	0.00	0.00	0.00	0.00	0.00	0.00	0.00
Al	0.10	0.10	0.09	0.07	0.08	0.06	0.13	0.16	0.10	0.09	0.12
Fe	0.69	0.71	0.72	0.72	0.74	0.46	0.63	0.64	0.73	0.71	0.71
Mn	0.02	0.02	0.02	0.02	0.02	0.00	0.01	0.01	0.02	0.02	0.02
Mg	1.27	1.25	1.25	1.24	1.22	1.54	1.36	1.33	1.22	1.25	1.24
Ca	0.02	0.02	0.02	0.02	0.02	0.01	0.01	0.03	0.02	0.01	0.01
	4.02	4.03	4.03	4.02	4.02	4.02	4.04	4.05	4.02	4.02	4.02
X_{En}	64.73	63.89	63.50	63.28	62.25	77.07	68.30	67.32	62.55	63.69	63.72
X_{Fe}	35.27	36.11	36.50	36.72	37.75	22.93	31.70	32.68	37.45	36.31	36.28

Structural Formulae calculated on the basis of 6(O)
Type; i: inclusion m: matrix c: corona
X_{En} = 100Mg/(Mg+Fe) X_{Fe} = 100Fe/(Mg+Fe)

Mineral	Opx	Opx	Opx	Opx	Opx	Opx	Opx	Opx	Opx	Opx	Opx
Analysis	366	367	317	320	322	333	338	342	353	355	364
Type	C	C	M	M	M	I	I	I	M	M	C
BSE Image	8B-2	8B-2	8B-1	8B-1	8B-2	8B-3	8C-1	8C-1	8C-2	8C-2	8C-1
SiO_2	51.44	51.56	52.14	50.89	50.42	52.27	52.37	51.98	50.38	51.63	51.23
TiO_2	0.03	0.03	0.05	0.04	0.05	0.07	0.04	0.02	0.03	0.02	0.00
Al_2O_3	2.67	2.47	1.52	1.94	3.29	3.40	1.18	1.87	2.96	1.55	2.88
FeO	21.99	22.14	22.77	22.47	22.36	17.19	20.34	20.48	22.60	22.90	20.52
MnO	0.54	0.54	0.46	0.44	0.50	0.18	0.35	0.39	0.49	0.50	0.50
MgO	22.60	22.68	22.08	21.79	21.99	25.82	24.33	24.21	21.24	22.10	23.59
CaO	0.41	0.29	0.60	0.45	0.40	0.27	0.39	0.32	0.54	0.41	0.42
	99.77	99.78	99.65	98.07	99.08	99.21	99.05	99.36	98.32	99.17	99.20
Si	1.92	1.92	1.95	1.94	1.90	1.91	1.95	1.93	1.92	1.95	1.91
Ti	0.00	0.00	0.00	0.00	0.00	0.00	0.00	0.00	0.00	0.00	0.00
Al	0.12	0.11	0.07	0.09	0.15	0.15	0.05	0.08	0.13	0.07	0.13
Fe	0.69	0.69	0.71	0.72	0.71	0.53	0.63	0.64	0.72	0.72	0.64
Mn	0.02	0.02	0.01	0.01	0.02	0.01	0.01	0.01	0.02	0.02	0.02
Mg	1.26	1.26	1.23	1.24	1.24	1.41	1.35	1.34	1.20	1.24	1.31
Ca	0.02	0.01	0.02	0.02	0.02	0.01	0.02	0.01	0.02	0.02	0.02
	4.02	4.02	4.01	4.02	4.03	4.01	4.02	4.02	4.02	4.02	4.03
X_{En}	64.70	64.62	63.34	63.34	63.68	72.81	68.08	67.82	62.61	63.25	67.21
X_{Fe}	35.30	35.38	36.66	36.66	36.32	27.19	31.92	32.18	37.39	36.75	32.79

Structural Formulae calculated on the basis of 6(O)
Type; i: inclusion m: matrix c: corona
X_{En} = 100Mg/(Mg+Fe) X_{Fe} = 100Fe/(Mg+Fe)

Mineral	Opx	Opx
Analysis	397	398
Type	C	C
BSE Image	8C	8C
SiO_2	51.40	50.39
TiO_2	0.06	0.05
Al_2O_3	2.79	2.94
FeO	20.12	20.41
MnO	0.51	0.54
MgO	23.53	23.24
CaO	0.45	0.41
	99.06	98.11
Si	1.92	1.90
Ti	0.00	0.00
Al	0.12	0.13
Fe	0.63	0.65
Mn	0.02	0.02
Mg	1.31	1.31
Ca	0.02	0.02
	4.02	4.03
X_{En}	67.59	66.98
X_{Fe}	32.41	33.02

Structural Formulae calculated on the basis of 6(O)
Type; i: inclusion m: matrix c: corona
X_{En} = 100Mg/(Mg+Fe) X_{Fe} = 100Fe/(Mg+Fe)

Mineral	Plag	Plag	Plag	Plag	Plag	Plag	Plag	Plag	Plag	Plag	Plag
Analysis	19	20	21	22	23	24	25	33	361	374	375
Type	C	C	C	C	C	C	C	C	M	M	M
BSE Image	5A-1	5A-1	5A-1	5A-1	5A-1	5A-1	5A-1	5A-2	5A	5A	5A
SiO_2	43.36	43.46	43.17	43.52	43.31	43.57	43.76	46.46	52.58	51.87	48.46
Al_2O_3	35.64	35.81	35.83	35.77	35.74	35.79	35.87	34.23	28.96	30.32	33.14
CaO	19.52	19.60	19.66	19.63	19.42	19.67	19.53	17.63	12.38	12.53	15.86
Na_2O	0.78	0.77	0.69	0.76	0.74	0.71	0.74	1.95	4.81	4.61	2.90
K_2O	0.02	0.04	0.03	0.02	0.03	0.02	0.02	0.06	0.08	0.13	0.06
	99.49	99.83	100.01	99.82	99.40	99.98	100.07	100.54	99.28	99.52	100.60
Si	2.02	2.02	2.01	2.02	2.02	2.02	2.03	2.13	2.41	2.37	2.21
Al	1.96	1.96	1.96	1.96	1.97	1.96	1.96	1.85	1.56	1.63	1.78
Ca	0.98	0.98	0.98	0.98	0.97	0.98	0.97	0.87	0.61	0.61	0.77
Na	0.07	0.07	0.06	0.07	0.07	0.06	0.07	0.17	0.43	0.41	0.26
K	0.00	0.00	0.00	0.00	0.00	0.00	0.00	0.00	0.00	0.01	0.00
	5.04	5.04	5.04	5.03	5.03	5.03	5.03	5.03	5.03	5.03	5.03
X_{An}	93.27	93.34	94.01	93.43	93.52	93.86	93.59	83.31	58.70	60.08	75.10
X_{Ab}	6.73	6.66	5.99	6.57	6.48	6.14	6.41	16.69	41.30	39.92	24.90
X_{Or}	2.22	3.33	2.50	1.15	2.33	2.44	2.35	1.81	1.11	1.74	1.23

Structural Formulae calculated on the basis of 8(O)
Type; i: inclusion m: matrix c: corona
X_{An} = 100Ca/(Ca+Na+K) X_{Ab} =100Na/(Ca+Na+K) X_{Or} = 100K/(Ca+Na+K)

Mineral	Plag	Plag	Plag	Plag	Plag	Plag	Plag	Plag	Plag	Plag	Plag
Analysis	384	385	386	37	376	171	176	269	276	279	243
Type	M	M	M	I	I	C	C	C	C	C	I?
BSE Image	5A	5A	5A	5A-2	5A-4	5B-1	?	5B-5	5B-5	5B-6	5B-4
SiO_2	53.48	53.50	52.45	43.95	44.03	40.04	41.53	43.52	43.78	43.73	43.35
Al_2O_3	29.44	29.35	29.58	36.02	35.75	35.86	35.63	35.49	35.88	35.57	34.68
CaO	11.76	11.29	11.73	19.67	19.44	19.10	19.49	19.72	19.85	19.64	18.86
Na_2O	5.16	5.30	5.11	0.81	0.72	0.91	0.76	0.66	0.70	0.70	0.80
K_2O	0.19	0.17	0.14	0.02	0.01	0.01	0.03	0.02	0.03	0.03	0.03
	100.13	99.70	99.13	100.94	100.21	96.11	97.50	99.53	100.54	99.92	98.12
Si	2.42	2.43	2.40	2.02	2.04	1.94	1.98	2.03	2.02	2.03	2.05
Al	1.57	1.57	1.59	1.95	1.95	2.05	2.00	1.95	1.95	1.95	1.93
Ca	0.57	0.55	0.58	0.97	0.96	0.99	1.00	0.98	0.98	0.98	0.95
Na	0.45	0.47	0.45	0.07	0.06	0.09	0.07	0.06	0.06	0.06	0.07
K	0.01	0.01	0.01	0.00	0.00	0.00	0.00	0.00	0.00	0.00	0.00
	5.03	5.02	5.04	5.04	5.02	5.08	5.05	5.03	5.03	5.03	5.03
X_{An}	55.79	54.06	55.95	93.02	93.77	92.06	93.47	94.33	93.96	93.93	92.84
X_{Ab}	44.21	45.94	44.05	6.98	6.23	7.94	6.53	5.67	6.04	6.07	7.16
X_{Or}	2.42	2.02	1.74	2.15	1.23	0.07	0.15	0.15	0.15	0.15	0.16

Structural Formulae calculated on the basis of 8(O)
Type; i: inclusion m: matrix c: corona
X_{An} = 100Ca/(Ca+Na+K) X_{Ab} =100Na/(Ca+Na+K) X_{Or} = 100K/(Ca+Na+K)

Mineral	Plag	Plag	Plag	Plag	Plag	Plag	Plag	Plag	Plag	Plag	Plag
Analysis	238	240	297	299	302	304	306	292	293	311	312
Type	C	I?	C	C	C	C	C	M	M	M	M
BSE Image	5B	5B-4	5C-2	5C-02	5C-3	5C-3	5C-3	5C-1	5C-1	5C-4	5C-4
SiO_2	43.91	43.35	44.12	43.85	44.18	44.19	41.87	53.93	47.78	53.89	53.59
Al_2O_3	35.86	34.58	34.78	35.36	35.37	35.24	34.97	29.00	32.59	28.06	28.30
CaO	19.37	19.12	18.22	18.63	18.86	18.49	18.68	10.92	15.91	10.12	10.20
Na_2O	0.75	0.78	1.19	1.16	1.14	1.33	1.27	5.42	2.69	5.85	5.79
K_2O	0.02	0.01	0.01	0.02	0.02	0.02	0.02	0.21	0.08	0.23	0.23
	100.05	98.35	99.46	99.28	99.81	99.56	97.10	99.58	99.32	98.21	98.25
Si	2.03	2.05	2.06	2.04	2.05	2.06	2.00	2.45	2.21	2.48	2.46
Al	1.96	1.92	1.91	1.94	1.93	1.93	1.97	1.55	1.78	1.52	1.53
Ca	0.96	0.97	0.91	0.93	0.94	0.92	0.96	0.53	0.79	0.50	0.50
Na	0.07	0.07	0.11	0.11	0.10	0.12	0.12	0.48	0.24	0.52	0.52
K	0.00	0.00	0.00	0.00	0.00	0.00	0.00	0.01	0.00	0.01	0.01
	5.02	5.03	5.04	5.04	5.03	5.04	5.07	5.02	5.03	5.03	5.04
X_{An}	93.46	93.14	89.40	89.74	90.02	88.33	88.94	52.04	76.22	48.26	48.72
X_{Ab}	6.54	6.86	10.53	10.19	9.83	11.51	10.99	46.78	23.32	50.43	50.04
X_{Or}	0.08	0.08	0.08	0.08	0.15	0.15	0.07	1.18	0.46	1.32	1.24

Structural Formulae calculated on the basis of 8(O)
Type; i: inclusion m: matrix c: corona
X_{An} = 100Ca/(Ca+Na+K) X_{Ab} =100Na/(Ca+Na+K) X_{Or} = 100K/(Ca+Na+K)

Mineral	Plag	Plag	Plag	Plag	Plag	Plag	Plag	Plag	Plag	Plag	Plag
Analysis	369	370	125	132	137	138	152	153	160	161	162
Type	M	M	C	C	C	C	C	C	C	C	M?
BSE Image	5C-2	5C-2	5D-1	5D-1	5D-1	5D-1	5D-3	5D-3	5D-3	5D-3	5D-3
SiO_2	54.41	51.56	44.99	44.70	44.15	44.11	44.30	44.47	43.91	45.04	53.66
Al_2O_3	28.42	30.38	35.16	35.70	35.03	35.55	35.23	35.07	34.58	35.13	28.88
CaO	10.69	13.20	17.84	17.95	19.16	19.14	19.38	19.16	18.47	18.89	11.44
Na_2O	5.47	4.26	1.22	1.07	0.82	0.87	0.89	0.95	0.99	1.19	5.34
K_2O	0.23	0.13	0.04	0.04	0.02	0.02	0.01	0.01	0.03	0.03	0.15
	99.32	99.75	99.50	99.85	99.61	100.11	100.38	100.02	99.97	100.56	99.53
Si	2.47	2.35	2.08	2.07	2.05	2.04	2.05	2.06	2.05	2.07	2.44
Al	1.52	1.63	1.92	1.94	1.92	1.94	1.92	1.91	1.90	1.91	1.55
Ca	0.52	0.64	0.89	0.89	0.96	0.95	0.96	0.95	0.92	0.93	0.56
Na	0.48	0.38	0.11	0.10	0.07	0.08	0.08	0.09	0.09	0.11	0.47
K	0.01	0.01	0.00	0.00	0.00	0.00	0.00	0.00	0.00	0.00	0.01
	5.02	5.02	5.01	5.01	5.02	5.03	5.03	5.03	5.05	5.03	5.03
X_{An}	51.22	62.63	88.84	90.03	92.63	92.37	92.24	91.67	91.01	89.61	53.78
X_{Ab}	47.44	36.60	10.91	9.72	7.21	7.55	7.69	8.25	8.83	10.24	45.37
X_{Or}	1.34	0.78	0.24	0.24	0.16	0.08	0.08	0.08	0.16	0.15	0.85

Structural Formulae calculated on the basis of 8(O)
Type; i: inclusion m: matrix c: corona
X_{An} = 100Ca/(Ca+Na+K) X_{Ab} =100Na/(Ca+Na+K) X_{Or} = 100K/(Ca+Na+K)

Mineral	Plag	Plag	Plag	Plag	Plag	Plag	Plag	Plag	Plag	Plag	Plag
Analysis	164	141	247	251	46	80	81	82	76	77	99
Type	C	M	I	I	C	C	C	C	C	C	C
BSE Image	5D-3	5D-2	5D	5D	7A-1	7A-6	7A-6	7A-6	7A-6	7A-6	7A
SiO_2	44.52	44.42	47.23	47.58	44.68	44.94	44.59	45.39	44.77	44.54	44.54
Al_2O_3	34.79	33.57	33.22	33.28	34.30	34.42	34.78	35.09	34.97	34.89	35.63
CaO	18.82	18.16	16.66	16.46	18.62	18.28	18.68	18.65	18.48	18.51	18.30
Na_2O	1.15	1.42	2.25	2.53	1.13	1.13	0.96	1.31	1.17	1.12	1.09
K_2O	0.02	0.05	0.04	0.02	0.00	0.00	0.00	0.06	0.00	0.00	0.04
	99.48	98.14	99.65	100.07	98.85	98.80	99.10	100.76	99.68	99.32	100.05
Si	2.07	2.10	2.18	2.18	2.09	2.10	2.08	2.08	2.08	2.07	2.06
Al	1.91	1.87	1.81	1.80	1.89	1.89	1.91	1.90	1.91	1.91	1.94
Ca	0.94	0.92	0.82	0.81	0.93	0.91	0.93	0.92	0.92	0.92	0.91
Na	0.10	0.13	0.20	0.23	0.10	0.10	0.09	0.12	0.10	0.10	0.10
K	0.00	0.00	0.00	0.00	0.00	0.00	0.00	0.00	0.00	0.00	0.00
	5.03	5.04	5.02	5.03	5.02	5.01	5.01	5.03	5.02	5.02	5.02
X_{An}	89.89	87.30	80.20	78.09	90.11	89.92	91.52	88.43	89.76	90.09	90.06
X_{Ab}	9.96	12.40	19.56	21.76	9.89	10.08	8.48	11.27	10.24	9.91	9.70
X_{Or}	0.15	0.30	0.23	0.15	0.00	0.00	0.00	0.31	0.00	0.00	0.24

Structural Formulae calculated on the basis of 8(O)
Type; i: inclusion m: matrix c: corona
X_{An} = 100Ca/(Ca+Na+K) X_{Ab} =100Na/(Ca+Na+K) X_{Or} = 100K/(Ca+Na+K)

Mineral	Plag	Plag	Plag	Plag	Plag	Plag	Plag	Plag	Plag	Plag	Plag
Analysis	100	102	103	105	108	122	123	61	62	63	69
Type	C	C	C	C	C	C(I)	C(I)	M	M	M	M
BSE Image	7A	7A	7A	7A-8	7A-8	7A	7A	7A-3	7A-3	7A-3	7A-4
SiO_2	44.95	44.91	45.15	44.41	45.03	49.27	45.19	49.53	48.30	49.49	47.79
Al_2O_3	35.72	35.69	35.40	35.55	34.42	32.46	35.63	31.30	32.23	31.45	32.26
CaO	18.20	18.19	17.97	18.21	16.72	14.51	17.80	14.53	15.79	14.86	15.91
Na_2O	1.06	1.06	1.20	1.17	1.57	3.18	1.18	3.34	2.77	3.27	2.59
K_2O	0.04	0.04	0.03	0.04	0.04	0.12	0.03	0.09	0.06	0.06	0.03
	100.52	100.26	100.01	99.88	98.10	99.67	100.22	98.79	99.30	99.13	98.57
Si	2.07	2.07	2.08	2.06	2.11	2.26	2.08	2.29	2.23	2.28	2.22
Al	1.94	1.94	1.92	1.94	1.90	1.75	1.93	1.70	1.75	1.71	1.77
Ca	0.90	0.90	0.89	0.90	0.84	0.71	0.88	0.72	0.78	0.73	0.79
Na	0.09	0.10	0.11	0.10	0.14	0.28	0.11	0.30	0.25	0.29	0.23
K	0.00	0.00	0.00	0.00	0.00	0.01	0.00	0.01	0.00	0.00	0.00
	5.02	5.01	5.01	5.03	5.01	5.01	5.01	5.01	5.02	5.02	5.01
X_{An}	90.25	90.19	89.09	89.40	85.23	71.09	89.11	70.29	75.60	71.31	77.16
X_{Ab}	9.51	9.57	10.75	10.36	14.53	28.19	10.72	29.16	24.01	28.38	22.68
X_{Or}	0.24	0.24	0.16	0.24	0.24	0.72	0.16	0.55	0.39	0.31	0.16

Structural Formulae calculated on the basis of 8(O)
Type; i: inclusion m: matrix c: corona
X_{An} = 100Ca/(Ca+Na+K) X_{Ab} =100Na/(Ca+Na+K) X_{Or} = 100K/(Ca+Na+K)

Mineral	Plag	Plag	Plag	Plag	Plag	Plag	Plag	Plag	Plag	Plag	Plag
Analysis	71	73	110	114	403	404	405	406	47	48	50
Type	M	M	M	M	M	M	M	M	I	I	I
BSE Image	7A-4	7A-5	7A-9	7A-9	7A	7A	7A	7A	7A-1	7A-1	7A-1
SiO_2	49.00	50.98	46.93	47.94	50.01	49.54	49.07	49.60	47.86	48.26	48.30
Al_2O_3	31.70	29.67	34.26	33.15	31.99	32.08	32.50	31.46	30.06	32.16	32.01
CaO	14.84	13.26	16.69	15.54	14.93	15.04	15.32	14.50	13.21	15.73	15.65
Na_2O	3.12	4.00	1.99	2.58	3.36	3.25	3.07	3.42	2.52	2.71	2.75
K_2O	0.09	0.13	0.08	0.09	0.14	0.14	0.14	0.18	0.05	0.06	0.07
	98.76	98.05	100.24	99.71	100.55	100.21	100.27	99.30	98.82	99.11	98.78
Si	2.27	2.36	2.15	2.20	2.27	2.26	2.24	2.28	2.24	2.23	2.24
Al	1.73	1.62	1.85	1.80	1.71	1.73	1.75	1.71	1.66	1.75	1.75
Ca	0.74	0.66	0.82	0.76	0.73	0.74	0.75	0.71	0.66	0.78	0.78
Na	0.28	0.36	0.18	0.23	0.30	0.29	0.27	0.31	0.23	0.24	0.25
K	0.00	0.01	0.00	0.01	0.01	0.01	0.01	0.01	0.00	0.00	0.00
	5.01	5.01	5.02	5.02	5.02	5.02	5.02	5.02	5.05	5.02	5.01
X_{An}	72.08	64.15	81.79	76.48	70.52	71.35	72.86	69.33	74.06	76.03	75.56
X_{Ab}	27.45	35.07	17.73	22.96	28.70	27.87	26.36	29.66	25.58	23.65	24.05
X_{Or}	0.47	0.78	0.48	0.56	0.78	0.78	0.78	1.01	0.36	0.31	0.39

Structural Formulae calculated on the basis of 8(O)
Type; i: inclusion m: matrix c: corona
X_{An} = 100Ca/(Ca+Na+K) X_{Ab} =100Na/(Ca+Na+K) X_{Or} = 100K/(Ca+Na+K)

Mineral	Plag	Plag	Plag	Plag	Plag	Plag	Plag	Plag	Plag	Plag	Plag
Analysis	117	118	120	121	285	401	402	185	187	191	193
Type	I	I	I	I	C	C	C	M	M	M	M
BSE Image	7A-1	7A-1	7A-1	7A-1	7B	7B	7B	7B-1	7B-1	7B-1	7B-1
SiO_2	49.17	48.70	48.13	47.80	45.28	44.48	45.15	47.31	46.99	46.50	44.48
Al_2O_3	32.80	32.95	33.03	33.06	34.96	35.09	35.80	31.81	32.34	32.33	32.30
CaO	14.73	14.74	14.96	15.15	18.52	18.79	18.88	14.85	16.33	16.20	15.20
Na_2O	2.88	2.89	2.55	2.58	1.27	1.12	1.06	3.29	2.35	2.56	3.11
K_2O	0.11	0.09	0.12	0.09	0.05	0.04	0.04	0.16	0.06	0.12	0.14
	99.83	99.93	99.16	99.20	100.37	99.82	101.21	97.52	98.74	97.86	95.31
Si	2.25	2.23	2.22	2.21	2.08	2.06	2.06	2.22	2.19	2.19	2.15
Al	1.77	1.78	1.79	1.80	1.90	1.92	1.93	1.76	1.78	1.79	1.84
Ca	0.72	0.72	0.74	0.75	0.91	0.93	0.92	0.75	0.82	0.82	0.79
Na	0.25	0.26	0.23	0.23	0.11	0.10	0.09	0.30	0.21	0.23	0.29
K	0.01	0.01	0.01	0.00	0.00	0.00	0.00	0.01	0.00	0.01	0.01
	5.00	5.02	5.00	5.01	5.02	5.03	5.02	5.05	5.03	5.04	5.08
X_{An}	73.45	73.38	75.86	76.12	88.73	90.12	90.52	70.73	79.01	77.21	72.41
X_{Ab}	25.90	26.06	23.40	23.40	11.03	9.65	9.25	28.37	20.60	22.10	26.78
X_{Or}	0.65	0.57	0.74	0.49	0.23	0.23	0.24	0.91	0.39	0.68	0.81

Structural Formulae calculated on the basis of 8(O)
Type; i: inclusion m: matrix c: corona
X_{An} = 100Ca/(Ca+Na+K) X_{Ab} =100Na/(Ca+Na+K) X_{Or} = 100K/(Ca+Na+K)

Mineral	Plag	Plag	Plag	Plag	Plag	Plag	Plag	Plag	Plag	Plag	Plag
Analysis	382	244	245	207	209	211	264	196	218	371	372
Type	M	I	I	C	C	C	C	M	M	M	M
BSE Image	7B	7B	7B	8A-2	8A-2	8A-2	8A-4	8A-1	8A-1	8A	8A
SiO_2	51.69	50.31	48.76	43.40	44.42	44.20	45.36	54.13	55.91	54.87	56.40
Al_2O_3	29.70	29.33	31.18	35.46	35.66	35.96	35.24	28.97	26.93	27.80	27.06
CaO	12.86	12.56	13.62	19.51	19.20	19.23	18.57	10.97	9.17	10.17	9.12
Na_2O	4.32	3.74	3.88	0.63	1.04	0.88	1.41	5.45	6.42	5.79	6.41
K_2O	0.21	0.13	0.12	0.02	0.01	0.02	0.04	0.16	0.24	0.20	0.27
	98.88	98.69	97.82	99.62	100.52	100.83	100.96	99.73	98.73	98.93	99.29
Si	2.38	2.34	2.28	2.02	2.05	2.03	2.08	2.45	2.55	2.50	2.55
Al	1.61	1.60	1.72	1.95	1.94	1.95	1.90	1.55	1.45	1.49	1.44
Ca	0.63	0.62	0.68	0.97	0.95	0.95	0.91	0.53	0.45	0.50	0.44
Na	0.39	0.34	0.35	0.06	0.09	0.08	0.12	0.48	0.57	0.51	0.56
K	0.01	0.01	0.01	0.00	0.00	0.00	0.00	0.01	0.01	0.01	0.02
	5.02	5.04	5.04	5.03	5.03	5.03	5.04	5.02	5.02	5.02	5.02
X_{An}	61.41	64.44	65.54	94.35	91.08	92.22	87.76	52.24	43.47	48.74	43.41
X_{Ab}	37.42	34.74	33.77	5.50	8.92	7.63	12.01	46.90	55.13	50.16	55.10
X_{Or}	1.16	0.83	0.69	0.15	0.00	0.16	0.23	0.86	1.40	1.10	1.49

Structural Formulae calculated on the basis of 8(O)
Type; i: inclusion m: matrix c: corona
X_{An} = 100Ca/(Ca+Na+K) X_{Ab} =100Na/(Ca+Na+K) X_{Or} = 100K/(Ca+Na+K)

Mineral	Plag	Plag	Plag	Plag	Plag	Plag	Plag	Plag	Plag	Plag	Plag
Analysis	373	221	223	224	226	324	318	393	394	395	396
Type	M	I	I	I	I	C	M	M	M	M	M
BSE Image	8A	8A-3	8A-3	8A-3	8A-3	8B-2	8B-1	8B	8B	8B	8B
SiO_2	54.44	57.93	51.61	43.40	42.82	44.12	45.45	44.86	46.53	46.35	45.64
Al_2O_3	28.38	25.67	30.12	35.97	36.11	35.44	35.02	35.32	34.26	34.50	35.07
CaO	10.69	7.30	12.69	19.40	19.65	19.07	18.02	18.78	17.34	17.69	18.21
Na_2O	5.49	7.51	4.61	0.78	0.59	1.02	1.57	1.21	2.02	1.74	1.50
K_2O	0.23	0.17	0.05	0.00	0.00	0.03	0.02	0.03	0.04	0.05	0.05
	99.36	98.85	99.25	99.78	99.87	99.75	100.29	100.37	100.40	100.49	100.78
Si	2.47	2.62	2.36	2.02	2.00	2.05	2.09	2.07	2.13	2.12	2.09
Al	1.52	1.37	1.63	1.97	1.98	1.94	1.90	1.92	1.85	1.86	1.89
Ca	0.52	0.35	0.62	0.97	0.98	0.95	0.89	0.93	0.85	0.87	0.89
Na	0.48	0.66	0.41	0.07	0.05	0.09	0.14	0.11	0.18	0.15	0.13
K	0.01	0.01	0.00	0.00	0.00	0.00	0.00	0.00	0.00	0.00	0.00
	5.02	5.03	5.03	5.03	5.04	5.03	5.03	5.03	5.03	5.02	5.03
X_{An}	51.10	34.64	60.17	93.28	94.89	91.01	86.32	89.43	82.38	84.71	86.73
X_{Ab}	47.56	64.43	39.60	6.72	5.11	8.83	13.60	10.42	17.39	15.05	12.96
X_{Or}	1.34	0.94	0.23	0.00	0.00	0.15	0.08	0.15	0.23	0.23	0.31

Structural Formulae calculated on the basis of 8(O)
Type; i: inclusion m: matrix c: corona
X_{An} = 100Ca/(Ca+Na+K) X_{Ab} =100Na/(Ca+Na+K) X_{Or} = 100K/(Ca+Na+K)

Mineral	Plag	Plag	Plag	Plag	Plag	Plag	Plag
Analysis	368	345	352	356	339	343	365
Type	I	C	M	M	I	I	I
BSE Image	8B-3	8C-1	8C-2	8C-2	8C-1	8C-1	8C-1
SiO_2	51.21	43.31	44.23	44.87	55.20	51.13	46.89
Al_2O_3	29.76	36.10	35.86	35.26	27.81	30.04	33.25
CaO	12.61	19.45	19.31	18.50	9.91	12.74	16.53
Na_2O	4.23	0.73	0.93	1.28	6.26	4.68	2.22
K_2O	0.18	0.01	0.01	0.02	0.11	0.09	0.02
	99.30	99.77	100.51	100.14	99.65	98.98	99.31
Si	2.35	2.01	2.04	2.07	2.50	2.35	2.17
Al	1.61	1.98	1.95	1.92	1.48	1.63	1.81
Ca	0.62	0.97	0.95	0.92	0.48	0.63	0.82
Na	0.38	0.07	0.08	0.11	0.55	0.42	0.20
K	0.01	0.00	0.00	0.00	0.01	0.00	0.00
	5.03	5.03	5.03	5.03	5.04	5.04	5.02
X_{An}	61.59	93.58	91.90	88.75	46.37	59.79	80.33
X_{Ab}	37.38	6.34	8.02	11.09	53.01	39.76	19.51
X_{Or}	1.03	0.08	0.08	0.16	0.62	0.46	0.16

Structural Formulae calculated on the basis of 8(O)
Type; i: inclusion m: matrix c: corona
X_{An} = 100Ca/(Ca+Na+K) X_{Ab} =100Na/(Ca+Na+K) X_{Or} = 100K/(Ca+Na+K)

Mineral	Grt	Grt	Grt	Grt	Grt	Grt	Grt	Grt	Grt	Grt	Grt	Grt
Analysis	28	40	29	172	173	174	272	280	236	133	134	139
Type	C	C	R	R	R	C?	R	C?	C?	R	C	R
BSE Image	5A-1	5A-3	5A-1	5B-1	5B-1	5B	5B-5	5B-6	5B	5D	5D	5D
SiO_2	38.55	39.23	38.59	35.22	37.58	36.66	37.54	38.92	39.16	38.48	38.66	38.10
Al_2O_3	22.18	22.31	22.00	23.03	22.86	23.15	22.66	23.16	23.31	21.84	21.90	22.09
FeO	22.64	23.22	23.64	23.63	22.95	23.44	23.50	23.16	26.73	24.12	23.26	24.74
MnO	0.91	0.98	1.75	1.91	1.32	1.79	1.76	1.44	1.27	1.45	0.86	2.42
MgO	9.90	9.92	8.78	8.31	8.80	8.69	8.70	9.11	8.46	5.44	6.10	5.23
CaO	5.29	5.05	5.48	5.02	5.73	4.93	5.77	5.57	4.52	8.67	8.93	8.26
	99.69	100.91	100.43	97.20	99.37	98.77	100.06	101.47	103.70	100.20	99.93	101.10
Si	2.95	2.97	2.96	2.81	2.90	2.86	2.90	2.94	2.92	2.99	2.99	2.95
Al	2.00	1.99	1.99	2.17	2.08	2.13	2.06	2.06	2.05	2.00	2.00	2.02
Fe	1.45	1.47	1.52	1.58	1.48	1.53	1.52	1.46	1.67	1.56	1.50	1.60
Mn	0.06	0.06	0.11	0.13	0.09	0.12	0.12	0.09	0.08	0.09	0.06	0.16
Mg	1.13	1.12	1.00	0.99	1.01	1.01	1.00	1.02	0.94	0.63	0.70	0.60
Ca	0.43	0.41	0.45	0.43	0.48	0.41	0.48	0.45	0.36	0.72	0.74	0.69
	8.04	8.03	8.05	8.11	8.06	8.08	8.07	8.03	8.05	8.01	8.01	8.03
X_{Alm}	47.21	48.04	49.16	50.46	48.49	49.79	48.75	48.26	54.68	51.97	50.08	52.54
X_{Py}	36.77	36.55	32.54	31.64	33.15	32.92	32.19	33.80	30.86	20.92	23.40	19.80
X_{Grs}	14.11	13.37	14.60	13.75	15.54	13.43	15.36	14.90	11.83	23.95	24.64	22.47
X_{Sp}	1.91	2.04	3.70	4.15	2.82	3.87	3.71	3.05	2.63	3.15	1.88	5.19

Structural Formulae calculated on the basis of 12(O)
Type; R: rim C: core
X_{Alm}= 100Fe/(Fe+Mg+Ca+Mn) X_{Py} = 100Mg/(Fe+Mg+Ca+Mn) X_{Grs} = 100Ca/(Fe+Mg+Ca+Mn) X_{Sp} = 100Mn/(Fe+Mg+Ca+Mn)

Mineral	Grt	Grt	Grt	Grt	Grt	Grt	Grt	Grt	Grt	Grt	Grt	Grt
Analysis	252	55	56	57	119	286	287	202	203	222	265	266
Type	C	C	R	R	R	?	?	C	R	C	R	C
BSE Image	5D	7A	7A	7A	7A	7B	7B	8A-2	8A-2	8A-3	8A-4	8A-4
SiO_2	38.52	38.22	38.40	38.10	38.09	38.61	32.76	38.24	38.48	38.16	38.53	38.79
Al_2O_3	22.41	22.10	22.26	22.20	22.18	22.51	21.45	22.96	21.88	22.74	22.45	22.89
FeO	25.54	23.75	26.57	25.67	26.61	25.27	26.47	22.22	24.35	22.15	24.76	23.32
MnO	1.04	0.72	1.51	1.48	1.62	2.37	2.14	0.65	1.49	0.56	1.78	0.85
MgO	6.74	5.73	5.64	5.71	5.19	6.20	6.12	9.40	7.32	9.17	7.42	8.55
CaO	7.27	9.52	6.62	7.02	6.46	6.59	5.81	7.21	7.03	7.50	6.49	6.97
	101.76	100.03	100.99	100.17	100.29	101.69	94.89	100.89	100.75	100.48	101.58	101.55
Si	2.94	2.96	2.97	2.97	2.97	2.96	2.75	2.90	2.96	2.91	2.94	2.93
Al	2.02	2.02	2.03	2.04	2.04	2.03	2.12	2.05	1.98	2.04	2.02	2.04
Fe	1.63	1.54	1.72	1.67	1.74	1.62	1.86	1.41	1.57	1.41	1.58	1.47
Mn	0.07	0.05	0.10	0.10	0.11	0.15	0.15	0.04	0.10	0.04	0.12	0.05
Mg	0.77	0.66	0.65	0.66	0.60	0.71	0.77	1.06	0.84	1.04	0.84	0.96
Ca	0.60	0.79	0.55	0.59	0.54	0.54	0.52	8.07	8.05	8.06	8.05	8.04
	8.04	8.03	8.02	8.02	8.01	8.02	8.19	8.07	8.05	8.06	8.05	8.04
X_{Alm}	53.29	50.67	56.98	55.39	58.14	53.57	56.33	45.47	50.84	45.51	51.48	48.23
X_{Py}	25.08	21.78	21.53	21.97	20.21	23.43	23.20	34.29	27.21	33.59	27.50	31.51
X_{Grs}	19.44	26.01	18.19	19.42	18.08	17.91	15.85	18.89	18.80	19.74	17.27	18.49
X_{Sp}	2.19	1.54	3.30	3.22	3.58	5.08	4.62	1.35	3.15	1.16	3.75	1.77

Structural Formulae calculated on the basis of 12(O)

Type; R: rim C: core

X_{Alm}= 100Fe/(Fe+Mg+Ca+Mn) X_{Py} = 100Mg/(Fe+Mg+Ca+Mn) X_{Grs} = 100Ca/(Fe+Mg+Ca+Mn) X_{Sp} = 100Mn/(Fe+Mg+Ca+Mn)

Mineral	Grt	Grt	Grt	Grt	Grt
Analysis	325	326	334	341	344
Type	R	C	C	C	C
BSE Image	8B-2	8B-2	8B-3	8C-1	8C-1
SiO_2	38.71	38.85	39.10	38.65	38.66
Al_2O_3	22.04	21.97	22.67	22.20	22.18
FeO	23.9	22.06	22.41	23.77	23.69
MnO	1.53	0.80	0.79	1.27	1.77
MgO	7.89	9.72	10.54	8.68	7.89
CaO	6.81	6.83	5.16	5.99	6.60
	101.00	100.35	100.73	100.72	100.95
Si	2.96	2.96	2.95	2.95	2.96
Al	1.99	1.97	2.02	2.00	2.00
Fe	1.53	1.40	1.41	1.52	1.52
Mn	0.1	0.05	0.05	0.08	0.12
Mg	0.9	1.10	1.19	0.99	0.90
Ca	0.56	0.56	0.42	0.49	0.54
	8.04	8.05	8.04	8.05	8.04
X_{Alm}	49.55	45.05	46.11	49.30	49.34
X_{Py}	29.13	35.39	38.64	32.09	29.30
X_{Grs}	18.09	17.91	13.61	15.93	17.62
X_{Sp}	3.23	1.66	1.64	2.69	3.75

Structural Formulae calculated on the basis of 12(O)

Type; R: rim C: core

X_{Alm}= 100Fe/(Fe+Mg+Ca+Mn) X_{Py} = 100Mg/(Fe+Mg+Ca+Mn) X_{Grs} = 100Ca/(Fe+Mg+Ca+Mn) X_{Sp} = 100Mn/(Fe+Mg+Ca+Mn)

Mineral	Spl	Spl	Spl	Spl
Analysis	169	275	346	349
BSE Image	5B-1	5B-5	8C-1	8C-1
SiO_2	0.02	0.00	0.64	0.00
TiO_2	0.01	0.05	0.10	0.07
Al_2O_3	61.34	60.39	53.95	54.95
Cr	0.58	0.56	1.79	2.90
FeO	27.22	29.70	33.01	33.10
Mn	0.28	0.29	0.26	0.27
MgO	9.90	9.91	8.56	8.15
Total	99.49	101.04	98.42	99.58
Si	0.00	0.00	0.02	0.00
Ti	0.00	0.00	0.00	0.00
Al	1.97	1.93	1.82	1.84
Cr	0.01	0.01	0.04	0.07
Fe	0.62	0.67	0.79	0.79
Mn	0.01	0.01	0.01	0.01
Mg	0.40	0.40	0.37	0.34
Total	3.01	3.03	3.05	3.05
X_{Sp}	0.393	0.373	0.316	0.305
X_{Hy}	0.607	0.627	0.684	0.895

Structural Formulae calculated on the basis of 4 (O)
X_{Sp} = 100Mg/(Mg+Fe) X_{Hy} = 100Fe/(Mg+Fe)

Mineral	Hbl	Hbl	Hbl	Hbl	Hbl	Hbl	Hbl	Hbl	Hbl	Hbl	Hbl
Analysis	27	34	178	182	270	273	281	283	241	242	413
Type	C	M	M	?	S	C	S	C	I?	I?	?
BSE Image	5A-1	5A-2	5B-2	5B	5B-5	5B-5	5B-6	5B-6	5B-4	5B-4	5B
SiO_2	39.92	41.02	36.99	36.06	39.64	40.48	40.24	40.19	39.62	40.22	40.49
TiO_2	1.68	2.25	1.30	1.89	1.26	1.34	1.31	1.51	1.83	1.71	1.99
Al_2O_3	15.15	13.13	14.14	14.65	15.55	15.58	15.94	15.50	14.83	14.80	14.36
Cr_2O_3	0.03	0.10	0.09	0.00	0.07	0.04	0.11	0.00	0.05	0.01	0.07
FeO	12.36	12.59	12.32	12.04	11.90	12.24	12.08	12.30	12.76	11.78	12.53
MnO	0.16	0.12	0.14	0.15	0.14	0.15	0.17	0.19	0.16	0.17	0.17
MgO	12.38	12.38	12.41	12.22	12.68	12.45	12.54	12.37	12.06	12.50	12.32
CaO	11.66	12.00	11.77	11.70	11.33	11.64	11.64	11.73	11.38	11.52	11.97
Na_2O	2.56	2.23	2.44	2.42	2.55	2.48	2.46	2.47	2.53	2.62	2.45
K_2O	0.92	1.23	0.66	1.01	0.83	0.94	0.90	0.89	0.98	0.69	0.89
Total	96.81	97.04	92.26	92.15	95.95	97.34	97.40	97.16	96.19	96.03	97.24
Si	5.98	6.14	5.85	5.73	5.96	6.01	5.97	5.98	5.98	6.04	6.04
Ti	0.19	0.25	0.15	0.23	0.14	0.15	0.14	0.17	0.21	0.19	0.22
Al	2.67	2.32	2.64	2.74	2.76	2.73	2.79	2.72	2.64	2.62	2.53
Cr	0.00	0.01	0.01	0.00	0.01	0.00	0.01	0.00	0.01	0.00	0.01
Fe	1.55	1.58	1.63	1.60	1.50	1.52	1.50	1.53	1.61	1.48	1.56
Mn	0.02	0.02	0.02	0.02	0.02	0.02	0.02	0.02	0.02	0.02	0.02
Mg	2.76	2.76	2.93	2.89	2.84	2.76	2.77	2.74	2.71	2.80	2.74
Ca	1.87	1.93	2.00	1.99	1.83	1.85	1.85	1.87	1.84	1.85	1.91
Na	0.74	0.65	0.75	0.75	0.75	0.72	0.71	0.71	0.74	0.76	0.71
K	0.18	0.23	0.13	0.20	0.16	0.18	0.17	0.17	0.19	0.13	0.17
Total	15.96	15.88	16.11	16.15	15.96	15.92	15.93	15.93	15.95	15.90	15.91

Structural Formulae calculated on the basis of 23(O)
Type; m: matrix c: corona s: symplectite

Mineral	Hbl	Hbl	Hbl	Hbl	Hbl	Hbl	Hbl	Hbl	Hbl	Hbl	Hbl
Analysis	294	301	315	145	150	155	58	59	60	67	410
Type	M	S?	M	M?	M	C	M	M	M	M	?
BSE Image	5C-1	5C-2	5C-4	5D-2	5D-2	5D-2	7A-3	7A-3	7A-3	7A-4	7A
SiO_2	40.69	40.36	40.59	41.12	40.78	42.13	42.24	41.96	42.05	41.39	41.18
TiO_2	1.48	0.96	2.09	1.05	1.26	0.72	1.20	1.34	1.32	2.03	2.03
Al_2O_3	12.93	13.46	12.46	12.93	11.11	12.82	11.60	11.98	11.53	12.07	12.16
Cr_2O_3	0.03	0.06	0.04	0.07	0.09	0.11	0.00	0.00	0.00	0.00	0.03
FeO	16.10	14.21	15.24	14.36	14.65	13.85	14.12	13.85	13.76	14.13	14.16
MnO	0.14	0.17	0.13	0.10	0.12	0.12	0.11	0.10	0.10	0.09	0.19
MgO	10.70	11.76	11.06	11.66	10.97	12.27	12.16	12.02	11.94	11.47	11.51
CaO	11.83	11.86	12.02	11.93	13.38	12.04	11.71	11.68	11.82	11.74	12.16
Na_2O	1.97	2.04	2.02	1.86	2.10	1.87	1.65	1.64	1.65	1.83	1.68
K_2O	1.43	1.21	1.35	1.22	0.45	1.00	1.36	1.35	1.43	1.57	1.49
Total	97.31	96.09	97.00	96.29	94.90	96.94	96.14	95.93	95.59	96.33	96.59
Si	6.18	6.15	6.17	6.24	6.31	6.31	6.40	6.36	6.40	6.28	6.24
Ti	0.17	0.11	0.24	0.12	0.15	0.08	0.14	0.15	0.15	0.23	0.23
Al	2.31	2.42	2.23	2.31	2.03	2.27	2.07	2.14	2.07	2.16	2.17
Cr	0.00	0.01	0.00	0.01	0.01	0.01	0.00	0.00	0.00	0.00	0.00
Fe	2.04	1.81	1.94	1.82	1.90	1.74	1.79	1.76	1.75	1.79	1.80
Mn	0.02	0.02	0.02	0.01	0.02	0.02	0.01	0.01	0.01	0.01	0.02
Mg	2.42	2.67	2.50	2.64	2.53	2.74	2.75	2.72	2.71	2.60	2.60
Ca	1.93	1.93	1.96	1.94	2.22	1.93	1.90	1.90	1.93	1.91	1.98
Na	0.58	0.60	0.59	0.55	0.63	0.54	0.49	0.48	0.49	0.54	0.49
K	0.28	0.23	0.26	0.24	0.09	0.19	0.26	0.26	0.28	0.30	0.29
Total	15.93	15.95	15.91	15.87	15.88	15.84	15.80	15.78	15.79	15.83	15.83

Structural Formulae calculated on the basis of 23(O)
Type; m: matrix c: corona s: symplectite

Mineral	Hbl	Hbl	Hbl	Hbl	Hbl	Hbl	Hbl	Hbl	Hbl	Hbl	Hbl
Analysis	189	192	289	381	197	198	200	204	213	215	216
Type	M	M	?	?	M	M	M	S	C	C	S
BSE Image	7B-1	7B-1	7B	7B	8A-1	8A-1	8A-1	8A-2	8A-2	8A-2	8A-2
SiO_2	40.97	40.75	41.65	42.25	40.53	43.69	40.73	40.57	41.13	40.97	40.55
TiO_2	1.76	2.15	2.06	1.84	2.50	1.65	2.54	1.00	1.24	1.15	1.37
Al_2O_3	10.71	11.17	11.67	11.40	13.47	10.82	13.47	14.74	13.72	13.90	14.41
Cr_2O_3	0.00	0.00	0.06	0.03	0.05	0.08	0.07	0.24	0.06	0.08	0.12
FeO	13.83	14.48	15.00	14.76	13.70	12.48	13.85	12.61	13.79	13.79	13.15
MnO	0.08	0.12	0.16	0.23	0.09	0.10	0.09	0.13	0.13	0.12	0.12
MgO	12.09	11.42	11.43	11.90	11.61	12.40	11.52	12.38	12.27	12.05	12.04
CaO	12.32	11.97	11.97	12.15	12.00	14.32	12.09	12.03	12.07	12.25	11.89
Na_2O	1.37	1.65	1.60	1.64	2.26	1.94	2.32	2.39	2.49	2.55	2.31
K_2O	1.49	1.61	1.64	1.47	1.20	0.68	1.20	0.83	0.63	0.62	0.93
Total	94.62	95.31	97.25	97.67	97.41	98.17	97.88	96.92	97.53	97.48	96.88
Si	6.34	6.28	6.29	6.34	6.08	6.45	6.08	6.07	6.14	6.12	6.08
Ti	0.20	0.25	0.23	0.21	0.28	0.18	0.29	0.11	0.14	0.13	0.15
Al	1.95	2.03	2.08	2.01	2.38	1.88	2.37	2.60	2.41	2.45	2.55
Cr	0.00	0.00	0.01	0.00	0.01	0.01	0.01	0.03	0.01	0.01	0.01
Fe	1.79	1.87	1.90	1.85	1.72	1.54	1.73	1.58	1.72	1.72	1.65
Mn	0.01	0.02	0.02	0.03	0.01	0.01	0.01	0.02	0.02	0.02	0.02
Mg	2.79	2.62	2.57	2.66	2.59	2.73	2.56	2.76	2.73	2.68	2.69
Ca	2.04	1.98	1.94	1.96	1.93	2.27	1.94	1.93	1.93	1.96	1.91
Na	0.41	0.49	0.47	0.48	0.66	0.55	0.67	0.69	0.72	0.74	0.67
K	0.29	0.32	0.32	0.28	0.23	0.13	0.23	0.16	0.12	0.12	0.18
Total	15.84	15.86	15.83	15.82	15.89	15.76	15.89	15.93	15.93	15.96	15.91

Structural Formulae calculated on the basis of 23(O)

Type; m: matrix c: corona s: symplectite

Mineral	Hbl	Hbl	Hbl	Hbl	Hbl	Hbl	Hbl
Analysis	268	229	319	321	323	329	362
Type	?	I?	M	M	S	S	?
BSE Image	8A-4	8A-3	8B-1	8B-1	8B-2	8B-2	8C
SiO_2	40.15	39.90	40.06	38.68	39.80	39.83	40.53
TiO_2	2.10	1.78	2.03	1.98	1.67	1.74	1.62
Al_2O_3	14.23	15.03	14.36	13.93	15.09	14.99	12.93
Cr_2O_3	0.06	0.12	0.08	0.09	0.16	0.16	0.25
FeO	14.01	10.84	12.86	13.10	12.73	13.18	12.11
MnO	0.13	0.08	0.10	0.11	0.11	0.15	0.16
MgO	11.32	13.34	11.51	11.27	11.91	11.62	13.00
CaO	11.73	12.05	12.01	11.82	11.82	11.84	12.05
Na_2O	2.44	2.78	2.23	2.40	2.36	2.44	2.63
K_2O	0.97	0.49	1.12	1.13	1.13	1.10	0.76
Total	97.14	96.41	96.37	94.51	96.78	97.05	96.03
Si	6.04	5.95	6.05	5.98	5.98	5.98	6.12
Ti	0.24	0.20	0.23	0.23	0.19	0.20	0.18
Al	2.52	2.65	2.55	2.54	2.67	2.65	2.30
Cr	0.01	0.01	0.01	0.01	0.02	0.02	0.03
Fe	1.76	1.35	1.62	1.70	1.60	1.65	1.53
Mn	0.02	0.01	0.01	0.01	0.01	0.02	0.02
Mg	2.54	2.97	2.59	2.60	2.67	2.60	2.93
Ca	1.89	1.93	1.94	1.96	1.90	1.90	1.95
Na	0.71	0.80	0.65	0.72	0.69	0.71	0.77
K	0.19	0.09	0.22	0.22	0.22	0.21	0.14
Total	15.91	15.96	15.88	15.98	15.94	15.95	15.99

Structural Formulae calculated on the basis of 23(O)

Type; m: matrix c: corona s: symplectite

APPENDIX B
BACK-SCATTER ELECTRON MICROGRAPH LABELLED IMAGES

B.1 Electron Microprobe Analysis Conditions

Chemical data of minerals, Backscatter images, and elemental X-ray maps were obtained by Electron Microprobe Analysis (EMPA) at Dalhousie University using a JEOL 8200 electron microprobe.

Analyses were conducted using a 15.0 kV accelerating voltage, 20 nA beam current and a counting time of 40s. Standards were appropriate metals and oxides (Appendix A).


5A-1
20
23
22
24
25
21
19
28
15
16
17
18
29
26
27
14
JEOL COMP 15.0kV ×40 100µm WD11mm

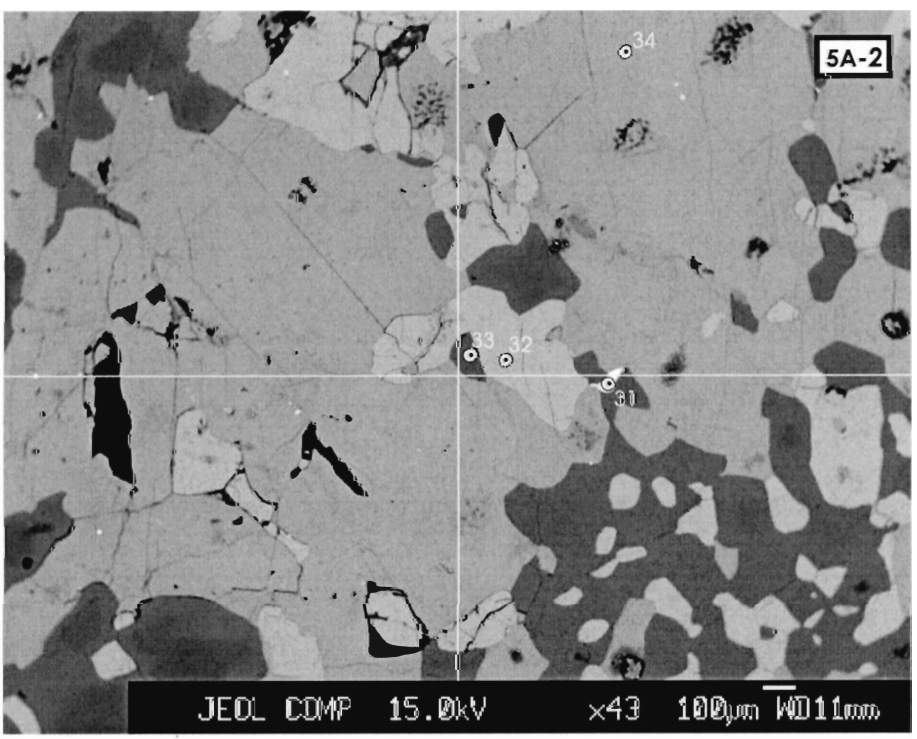
5A-2
34
33
32
31
JEOL COMP 15.0kV ×43 100µm WD11mm

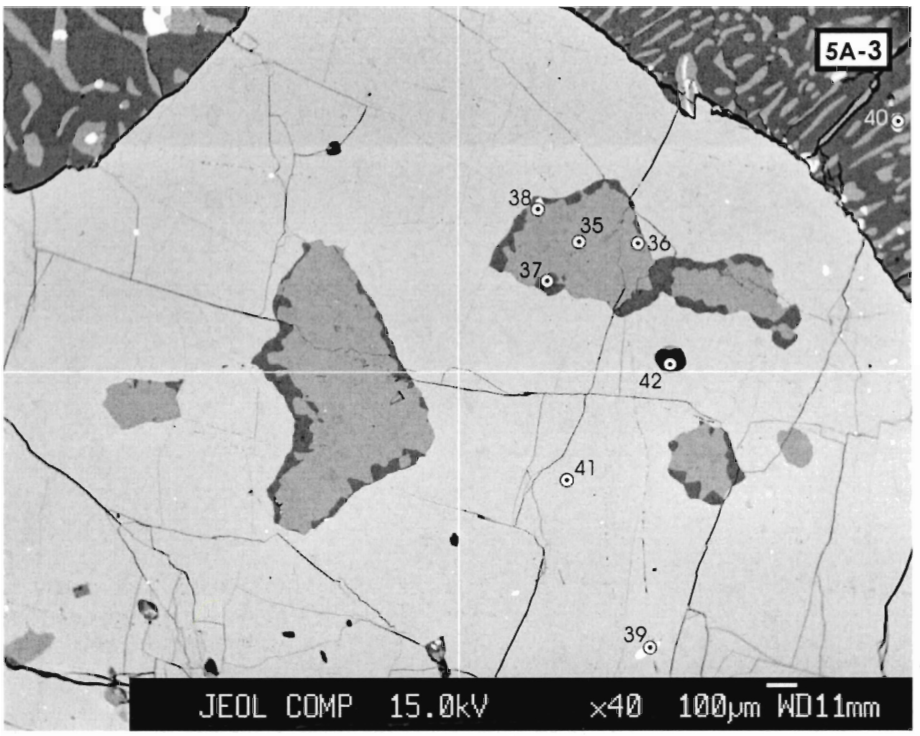
5A-3
40
38
35
36
37
42
41
39
JEOL COMP 15.0kV x40 100µm WD11mm

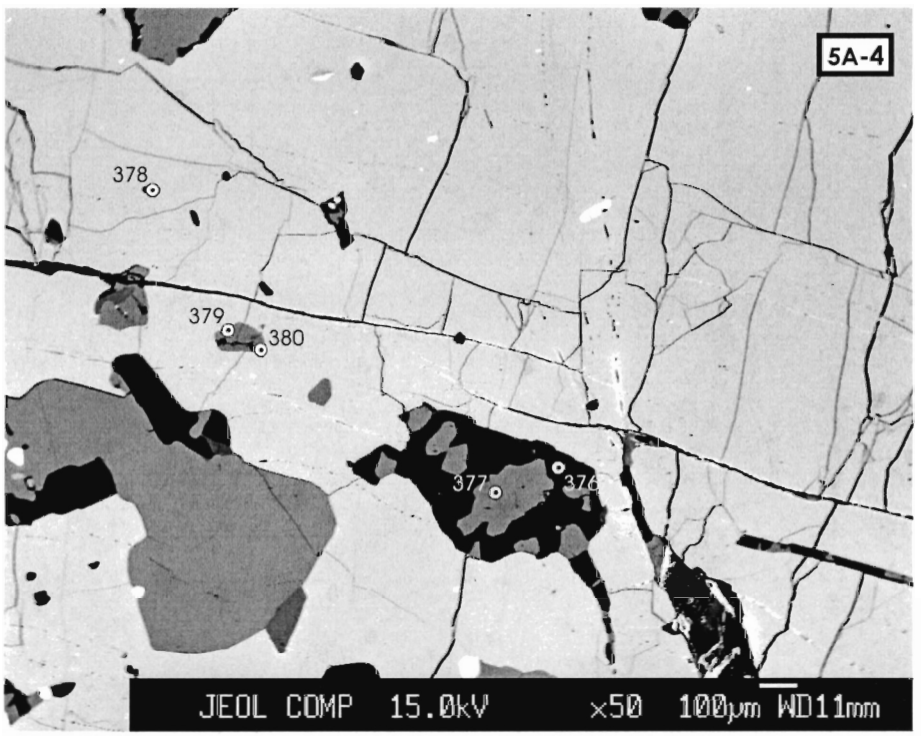
5A-4
378
379
380
377
376
JEOL COMP 15.0kV x50 100µm WD11mm

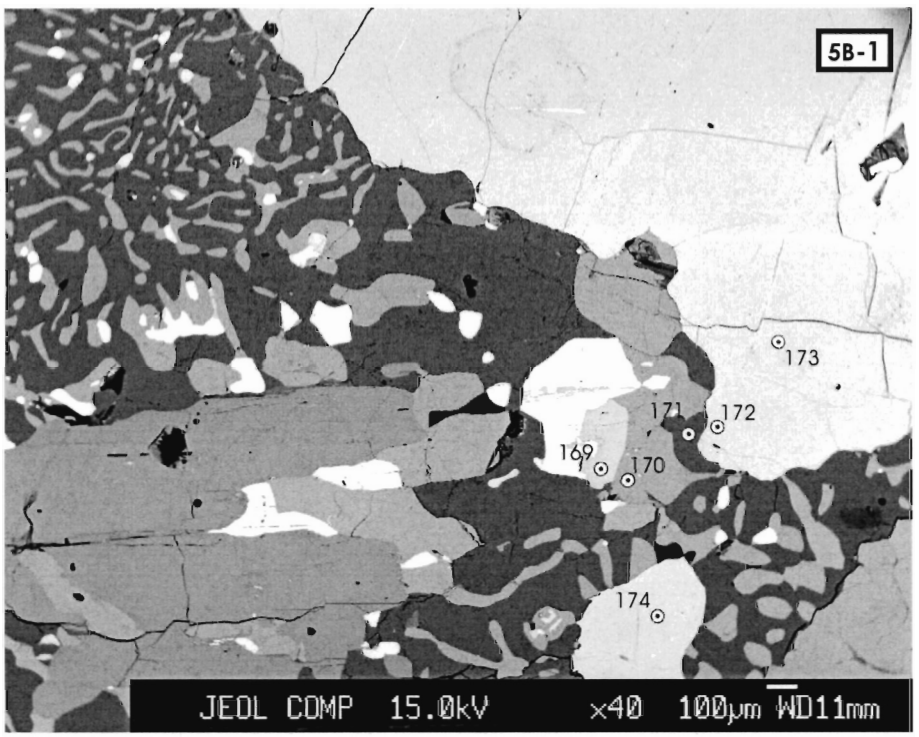
5B-1
173
171
172
169
170
174
JEOL COMP 15.0kV x40 100µm WD11mm

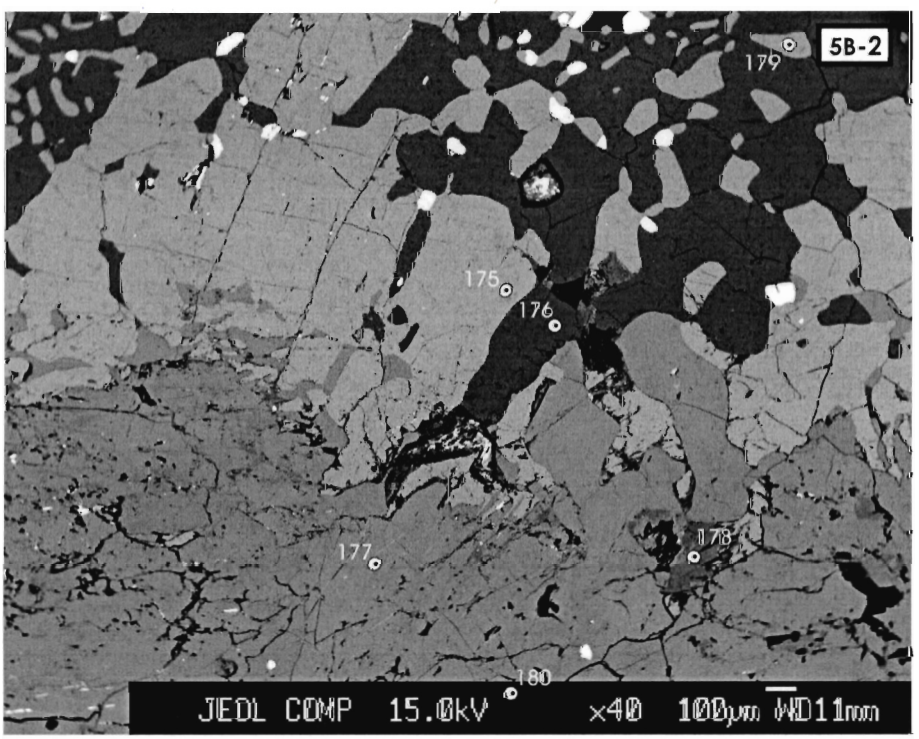
5B-2
179
175
176
177
178
180
JEOL COMP 15.0kV x40 100µm WD11mm

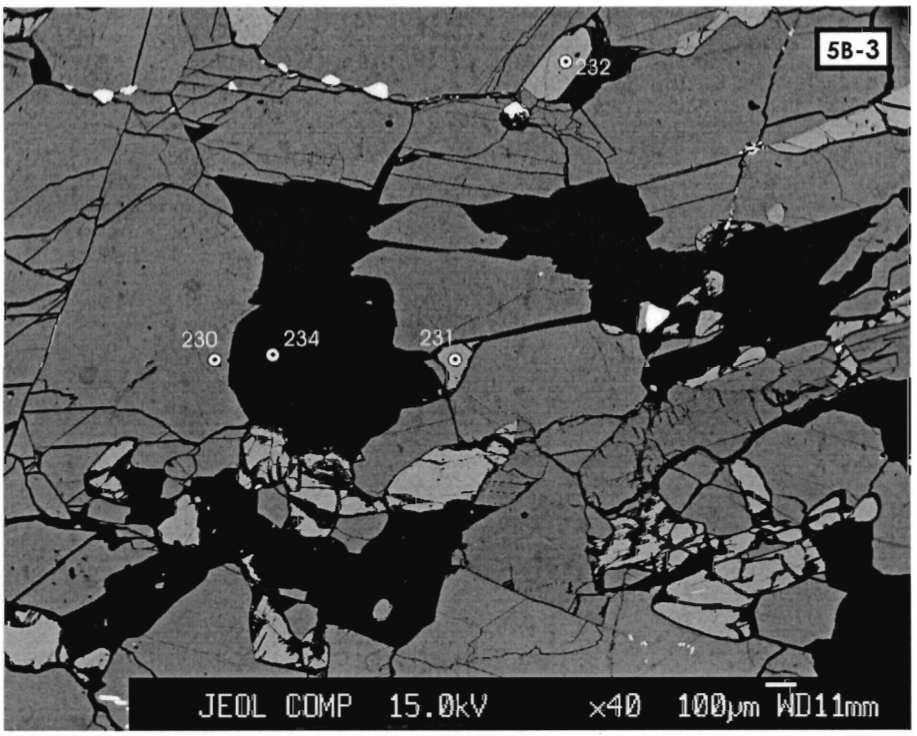
5B-3
232
230
234
231
JEOL COMP 15.0kV ×40 100µm WD11mm

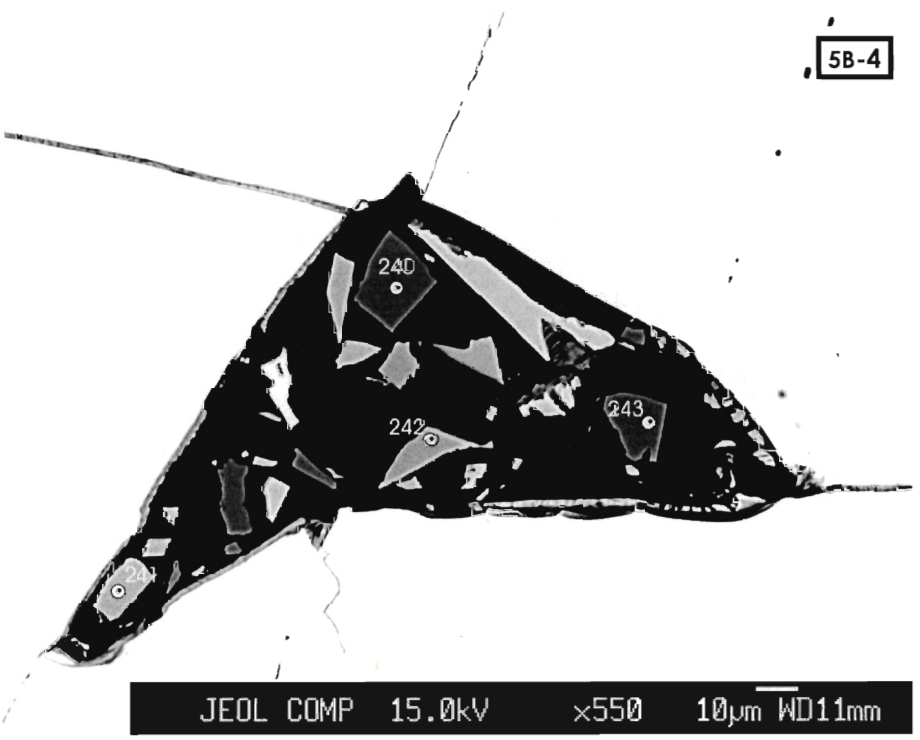
5B-4
240
242
243
JEOL COMP 15.0kV ×550 10µm WD11mm

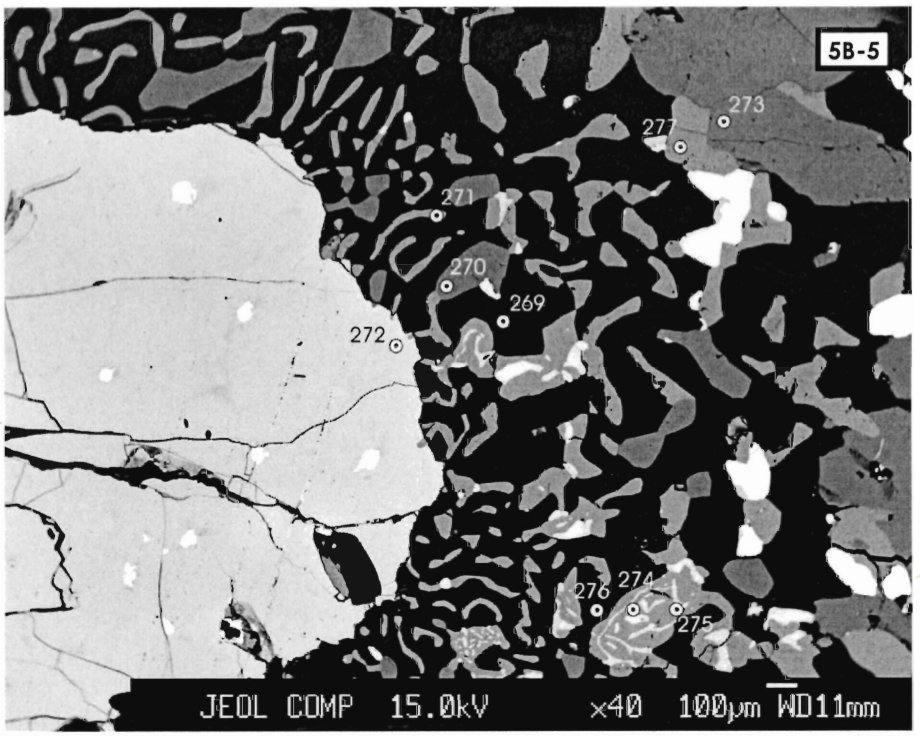
5B-5
273
277
271
270
269
272
276
274
275
JEOL COMP 15.0kV ×40 100μm WD11mm

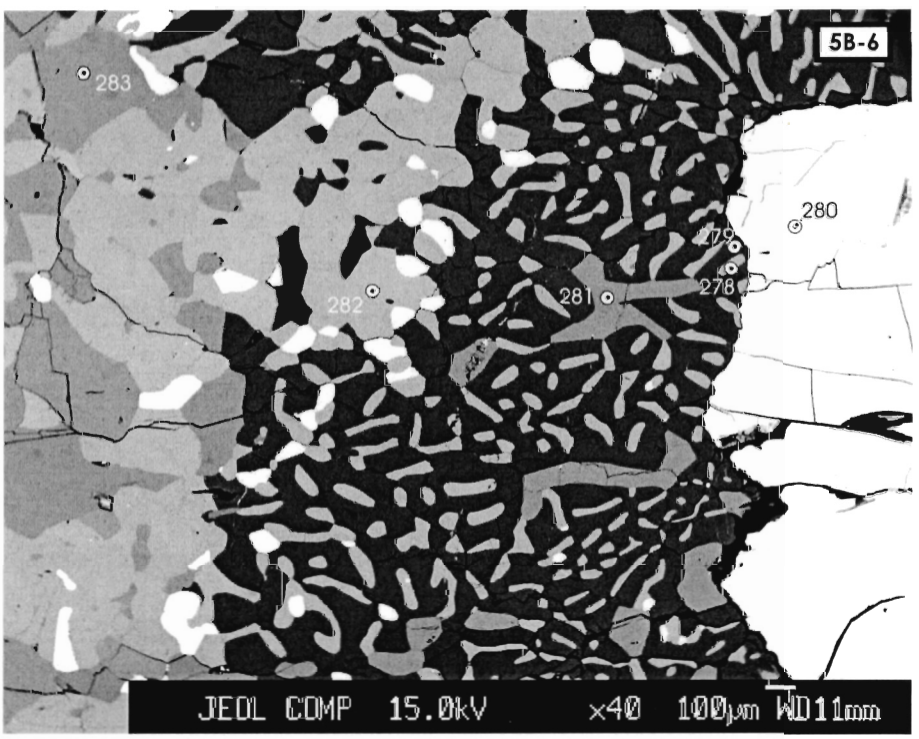
5B-6
283
280
279
278
281
282
JEOL COMP 15.0kV ×40 100μm WD11mm

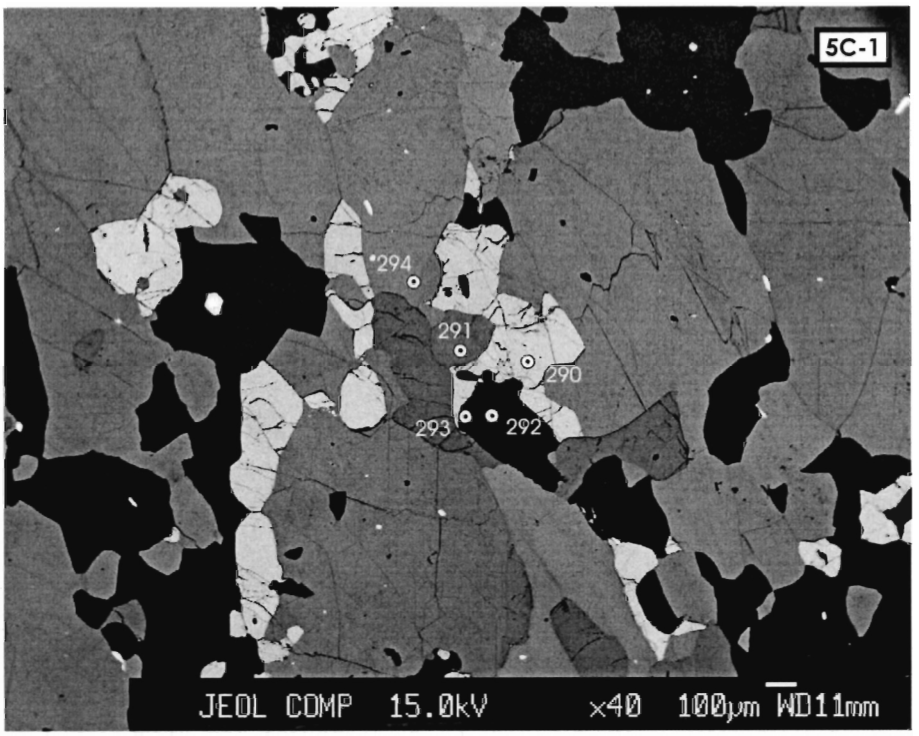
5C-1
294
291
290
293
292
JEOL COMP 15.0kV x40 100µm WD11mm

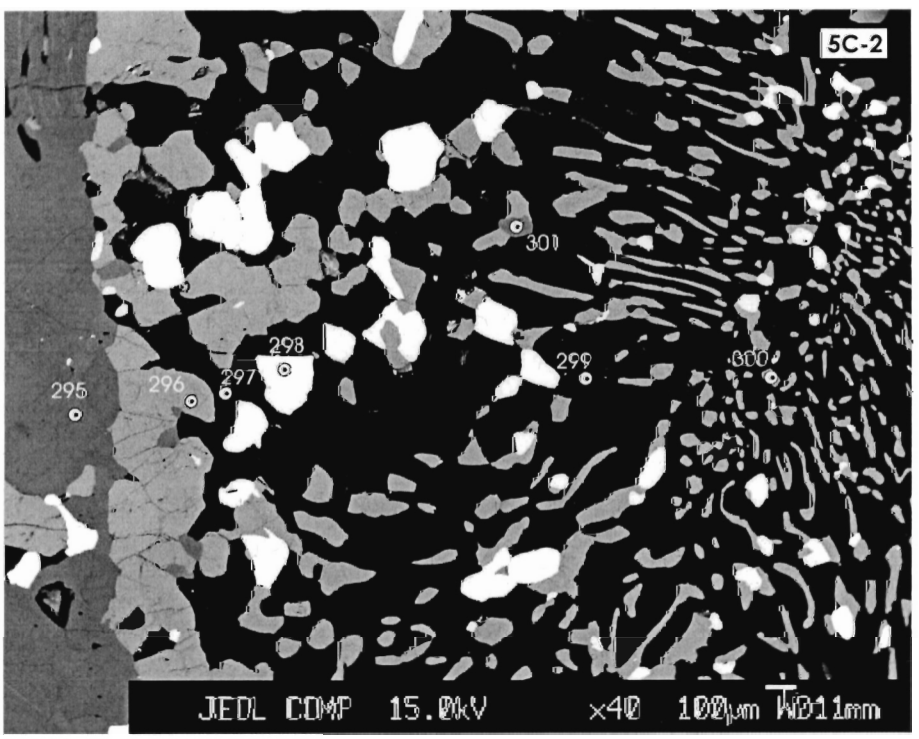
5C-2
301
298
297
296
295
299
300
JEOL COMP 15.0kV x40 100µm WD11mm

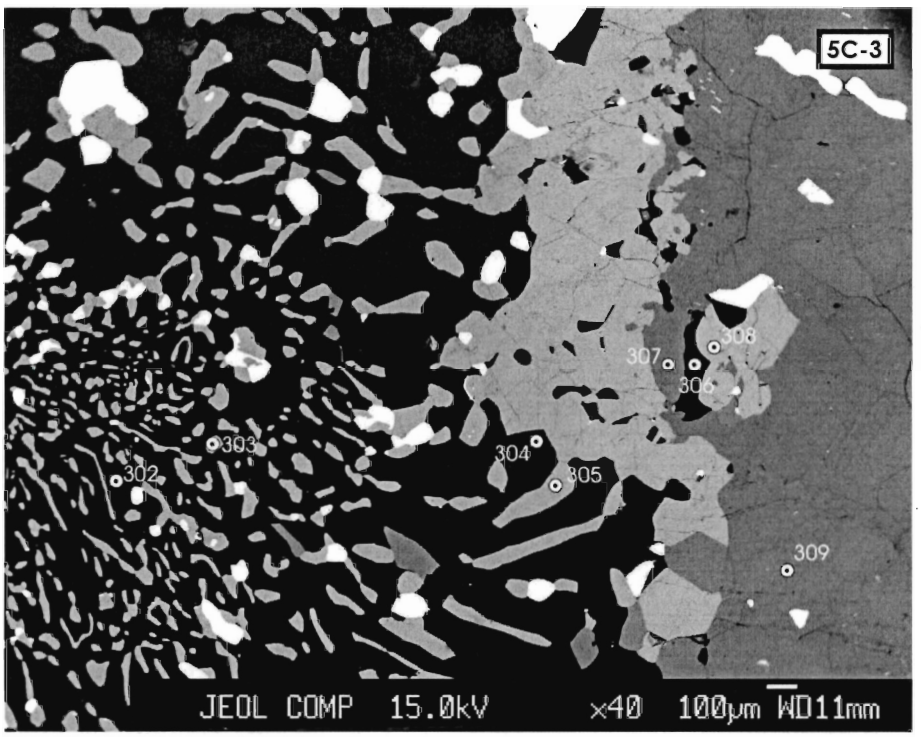
5C-3
308
307
306
303
304
305
302
309
JEOL COMP 15.0kV x40 100µm WD11mm

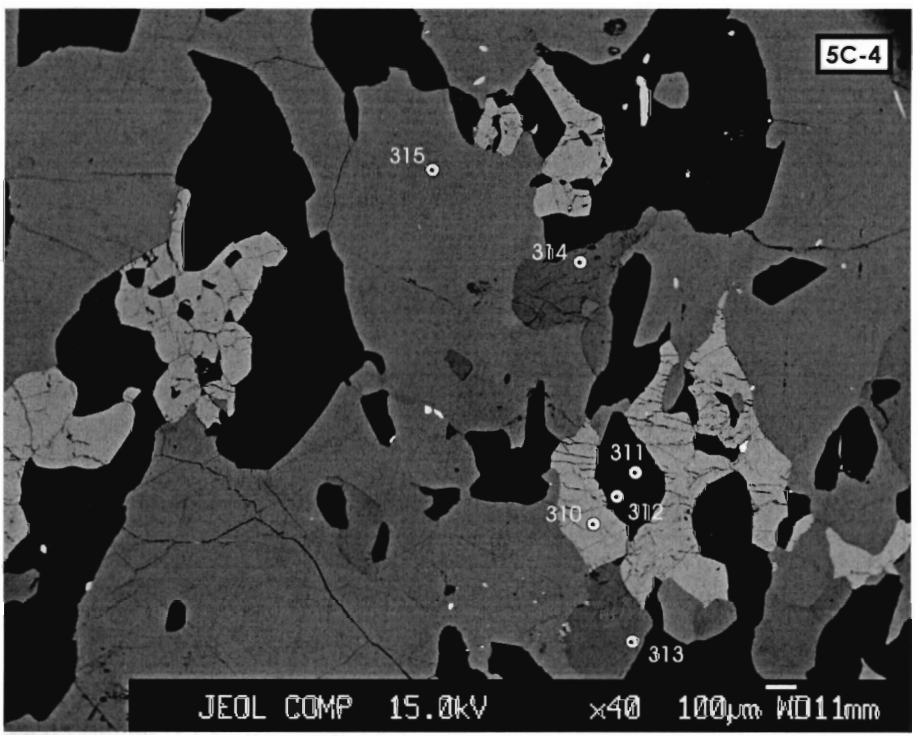
5C-4
315
314
311
312
310
313
JEOL COMP 15.0kV x40 100µm WD11mm

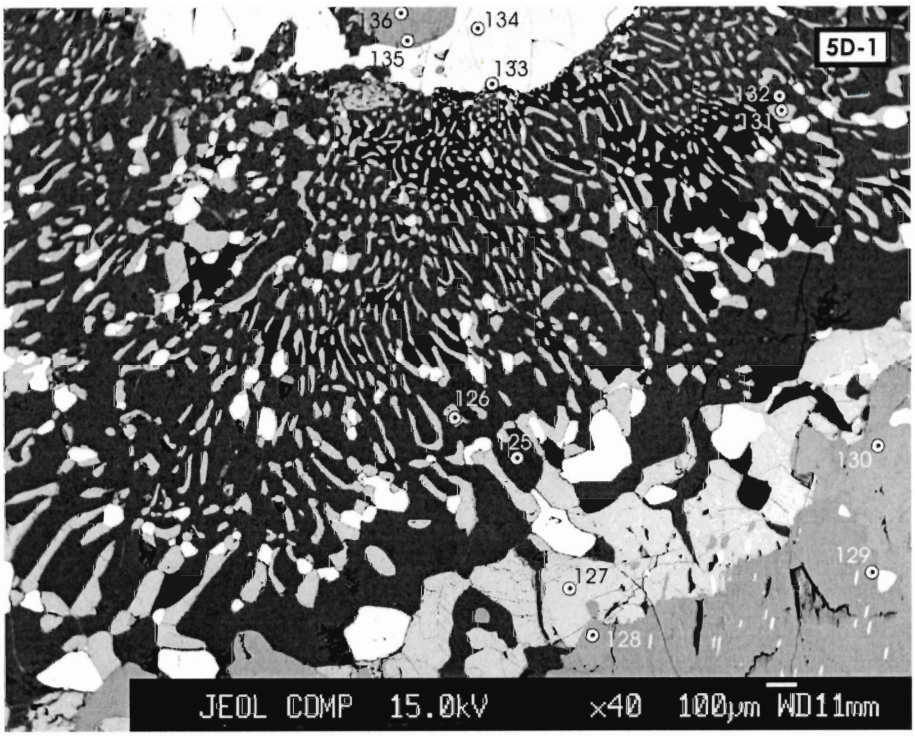
5D-1
136
134
135
133
132
131
126
125
130
129
127
128
JEOL COMP 15.0kV ×40 100μm WD11mm

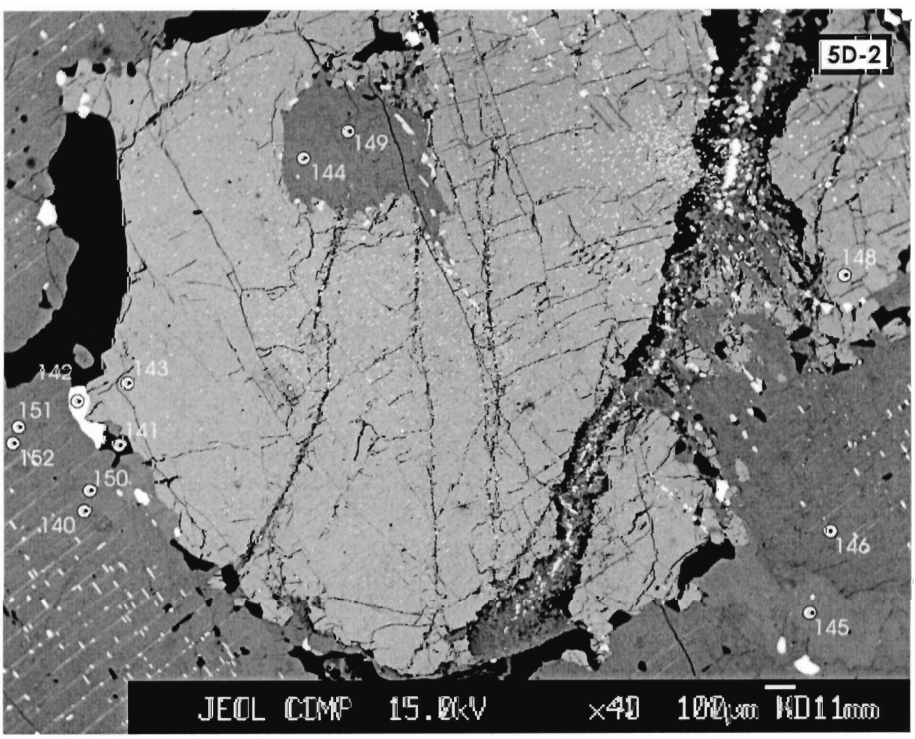
5D-2
149
144
148
142
143
151
141
152
150
140
146
145
JEOL COMP 15.0kV ×40 100μm WD11mm

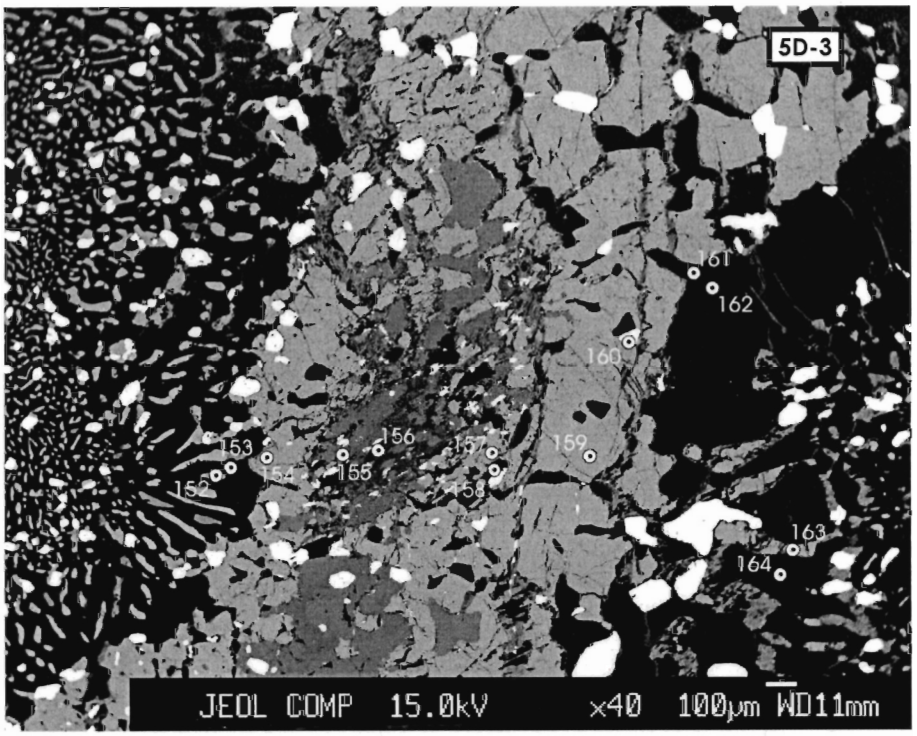
5D-3
161
162
160
153
156
157
159
154
155
152
158
163
164
JEOL COMP 15.0kV ×40 100µm WD11mm

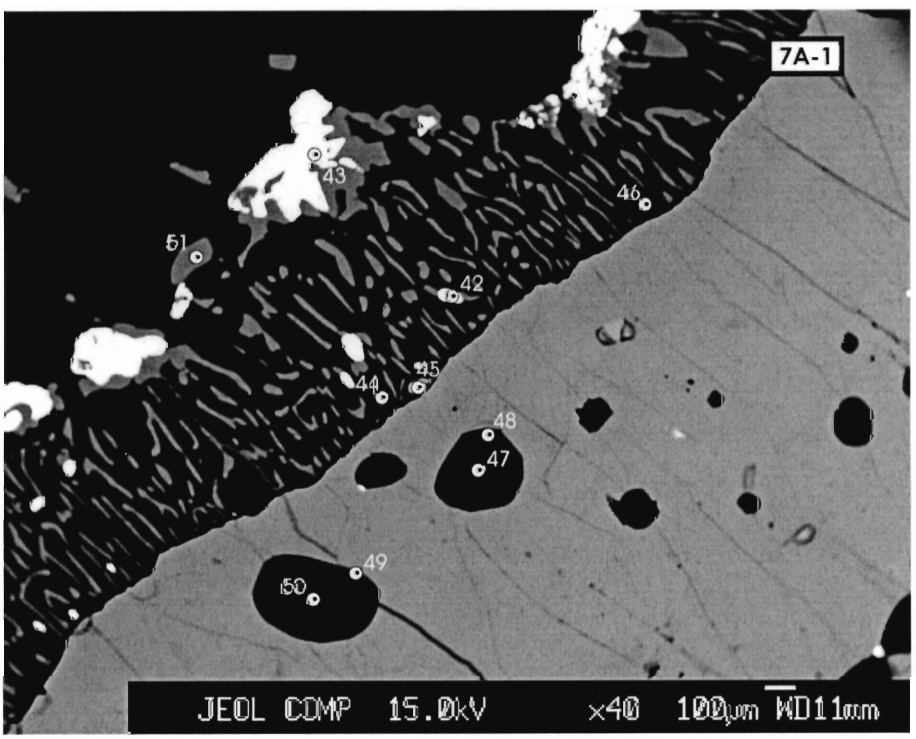
7A-1
43
46
51
42
45
44
48
47
49
50
JEOL COMP 15.0kV ×40 100µm WD11mm

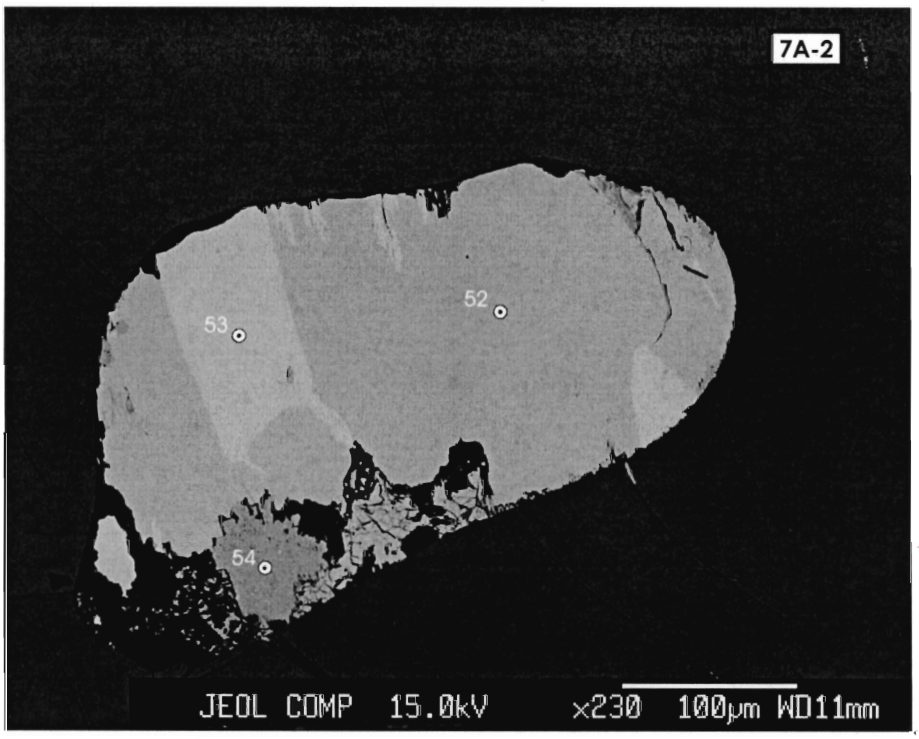
7A-2
52
53
54
JEOL COMP 15.0kV ×230 100µm WD11mm

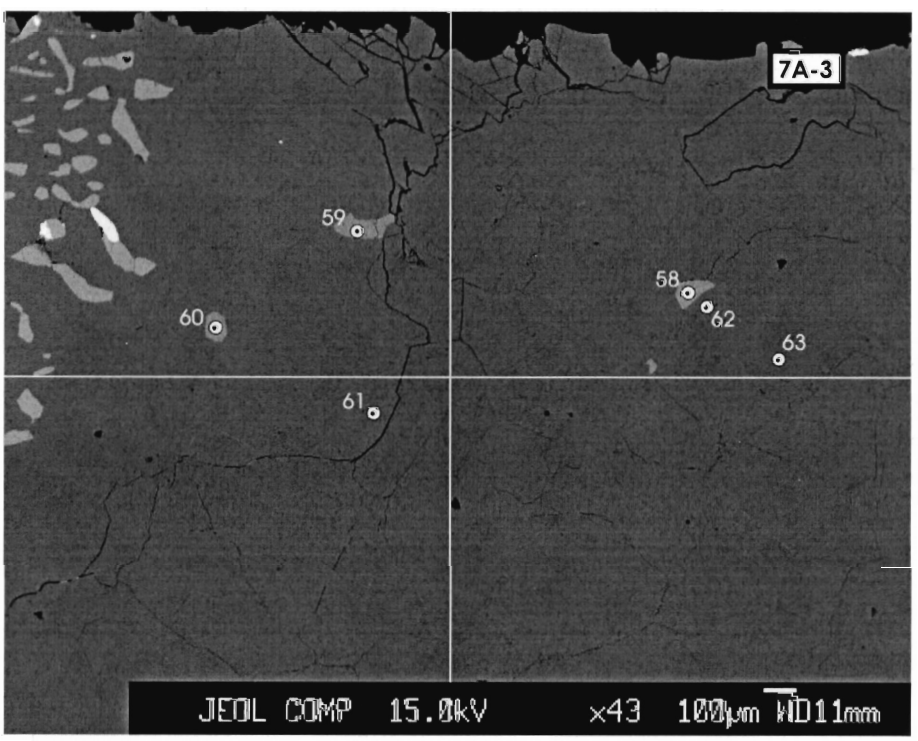
7A-3
59
60
61
58
62
63
JEOL COMP 15.0kV ×43 100µm WD11mm

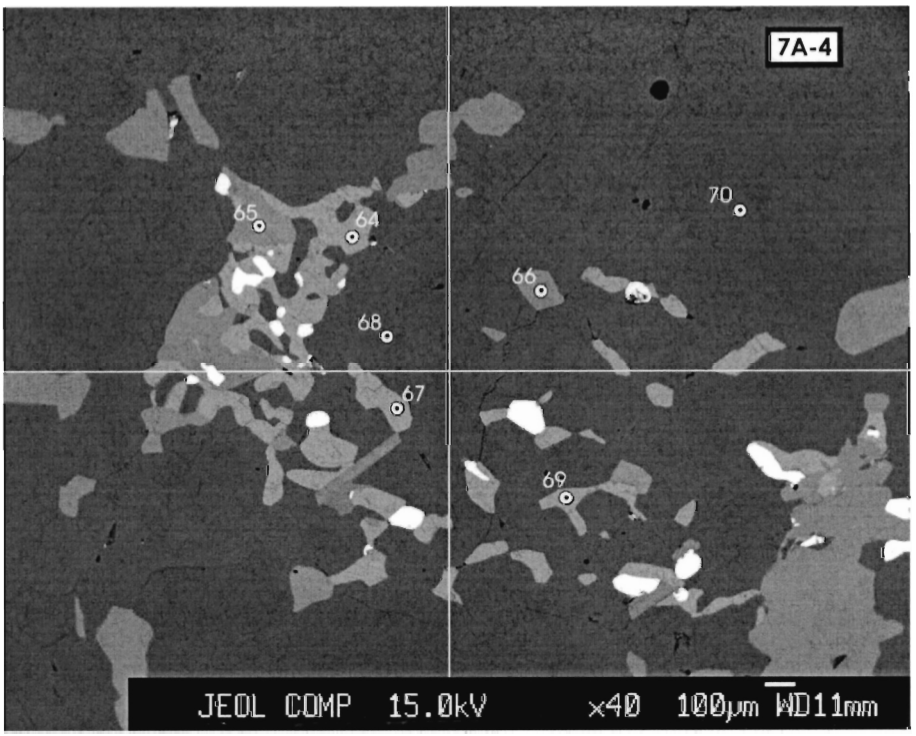
7A-4
65
64
68
70
66
67
69
JEOL COMP 15.0kV x40 100µm WD11mm

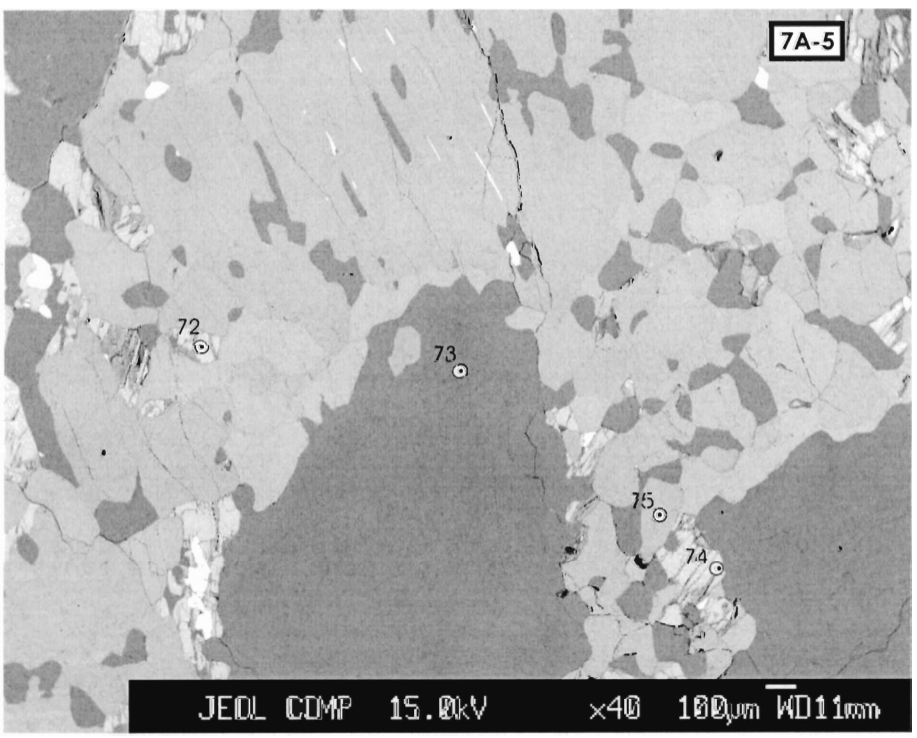
7A-5
72
73
75
74
JEOL COMP 15.0kV x40 100µm WD11mm

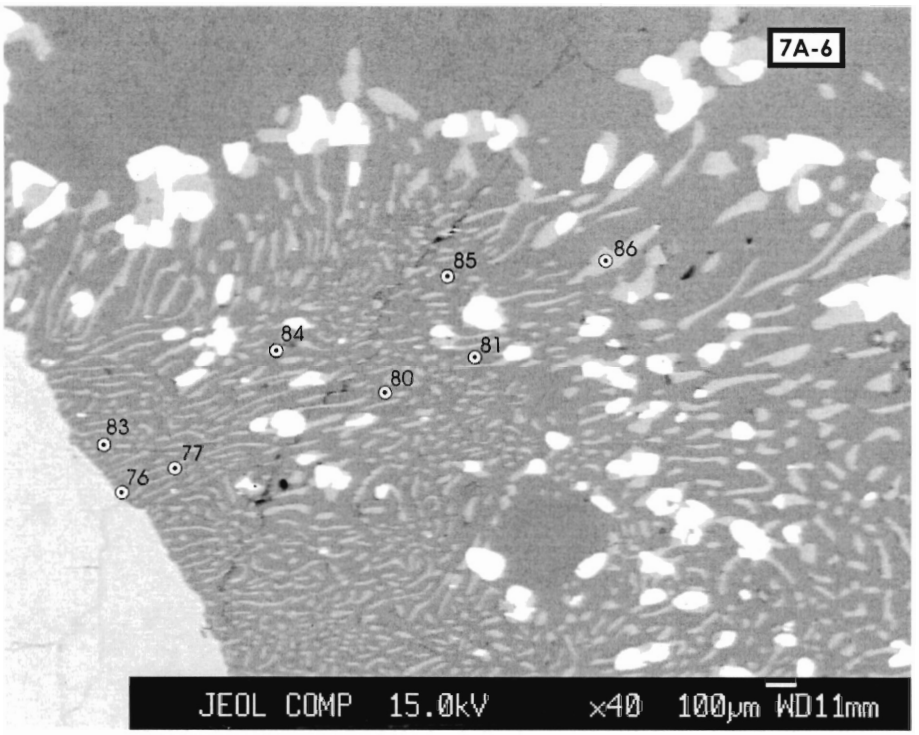
7A-6
85
86
84
81
80
83
77
76
JEOL COMP 15.0kV x40 100µm WD11mm

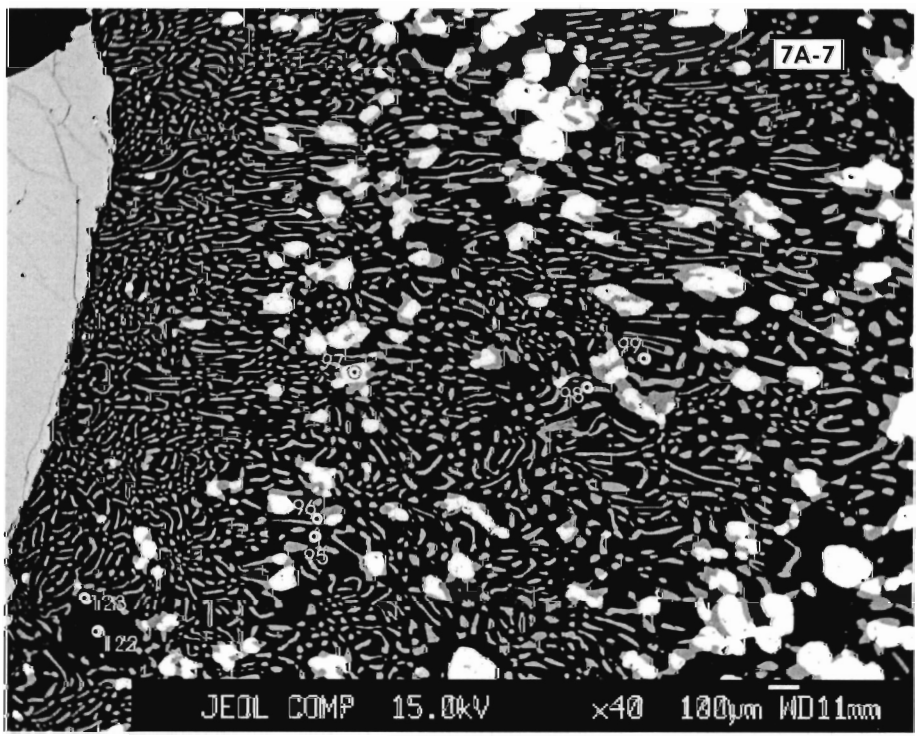
7A-7
99
97
98
96
95
123
122
JEOL COMP 15.0kV x40 100µm WD11mm

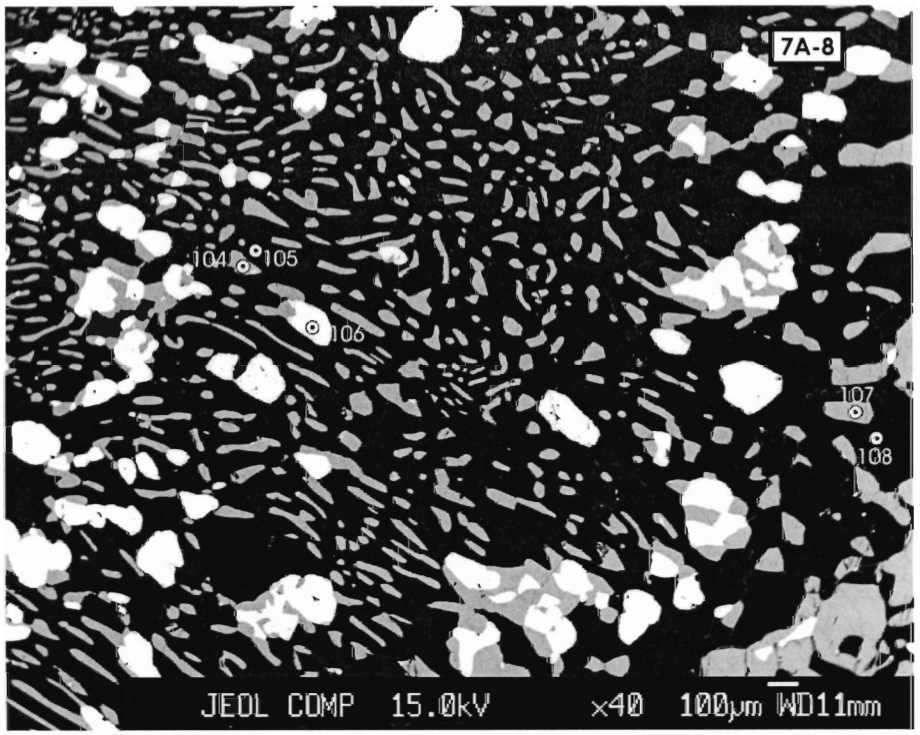
7A-8
104
105
106
107
108
JEOL COMP 15.0kV x40 100µm WD11mm

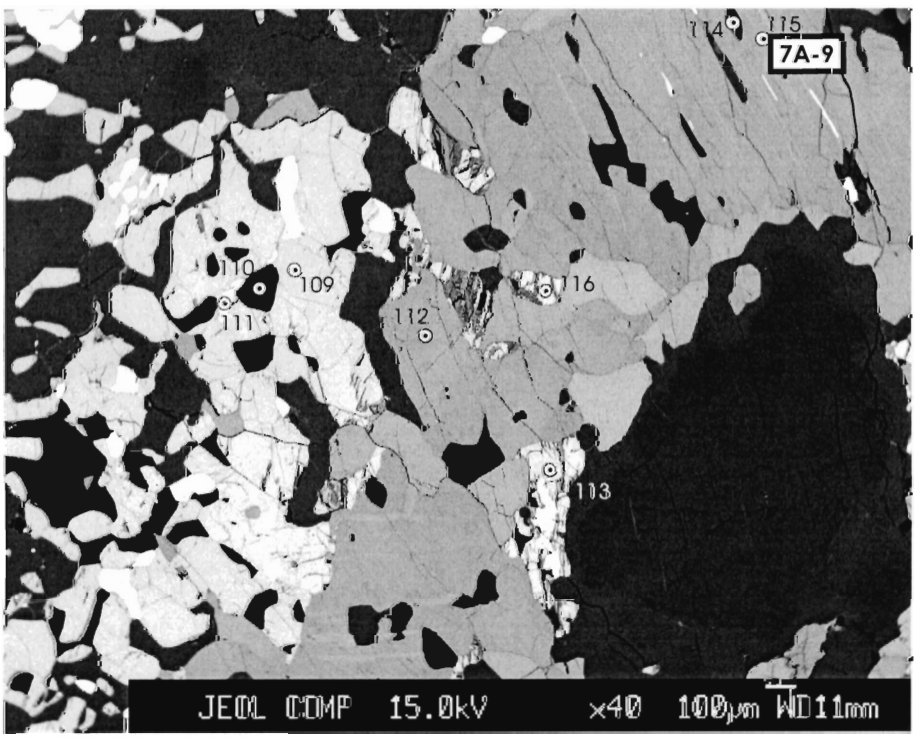
114
115
7A-9
110
109
111
112
116
113
JEOL COMP 15.0kV x40 100µm WD11mm

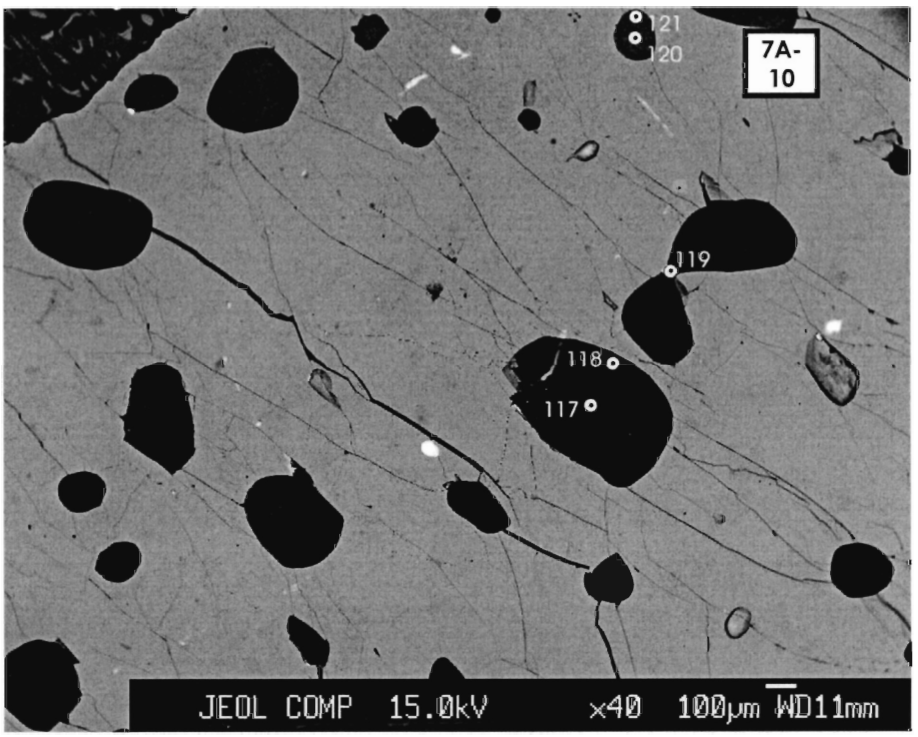
121
120
7A-
10
119
118
117
JEOL COMP 15.0kV x40 100µm WD11mm

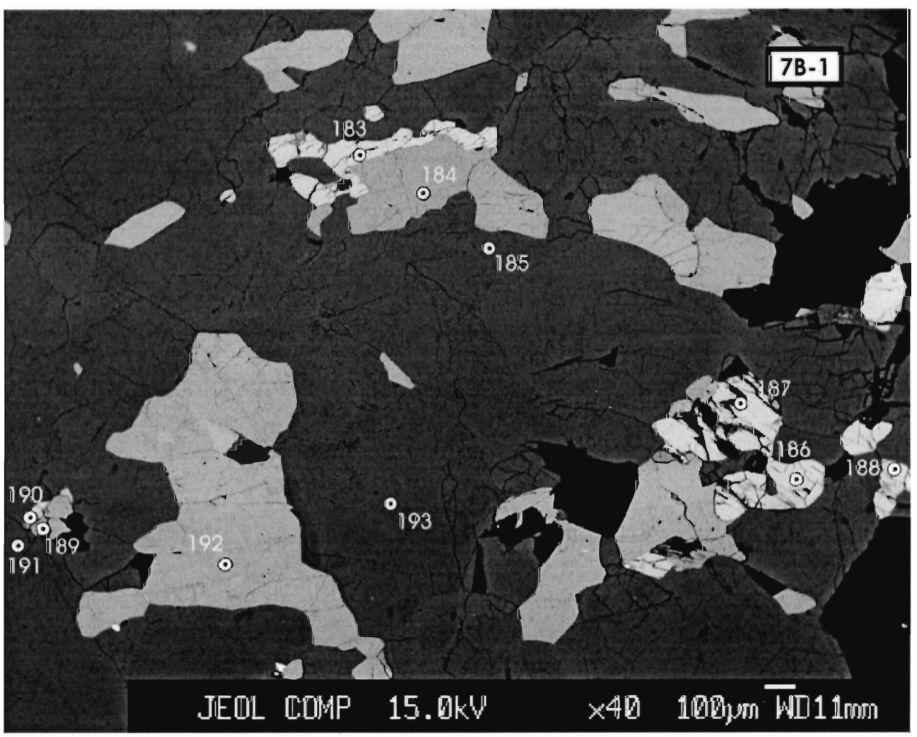
7B-1
183
184
185
187
186
188
190
189
191
192
193
JEOL COMP 15.0kV x40 100µm WD11mm

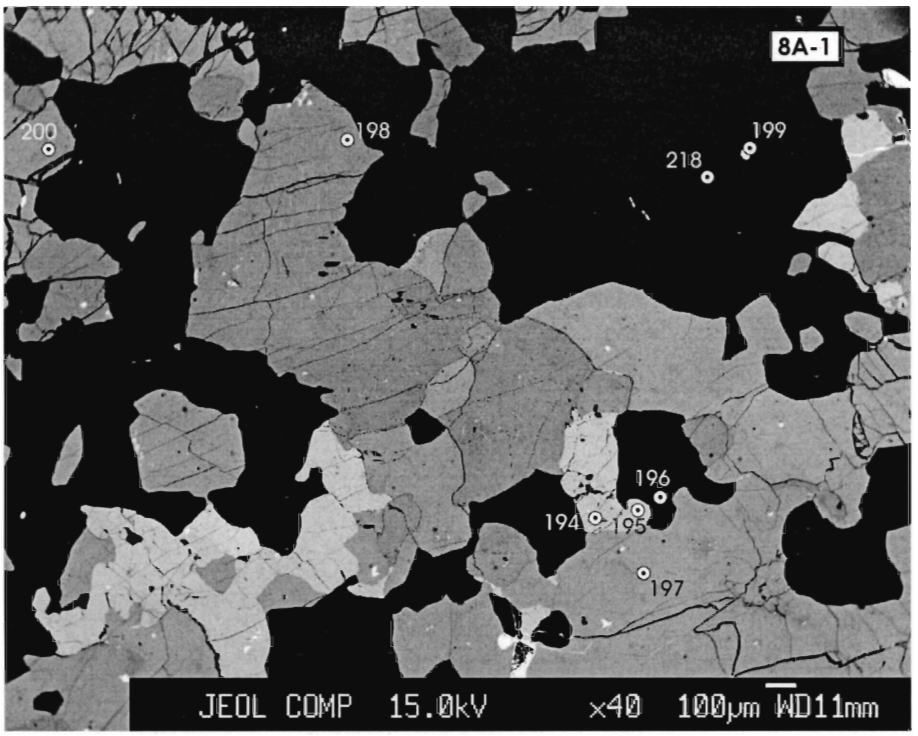
8A-1
200
198
199
218
196
194
195
197
JEOL COMP 15.0kV x40 100µm WD11mm

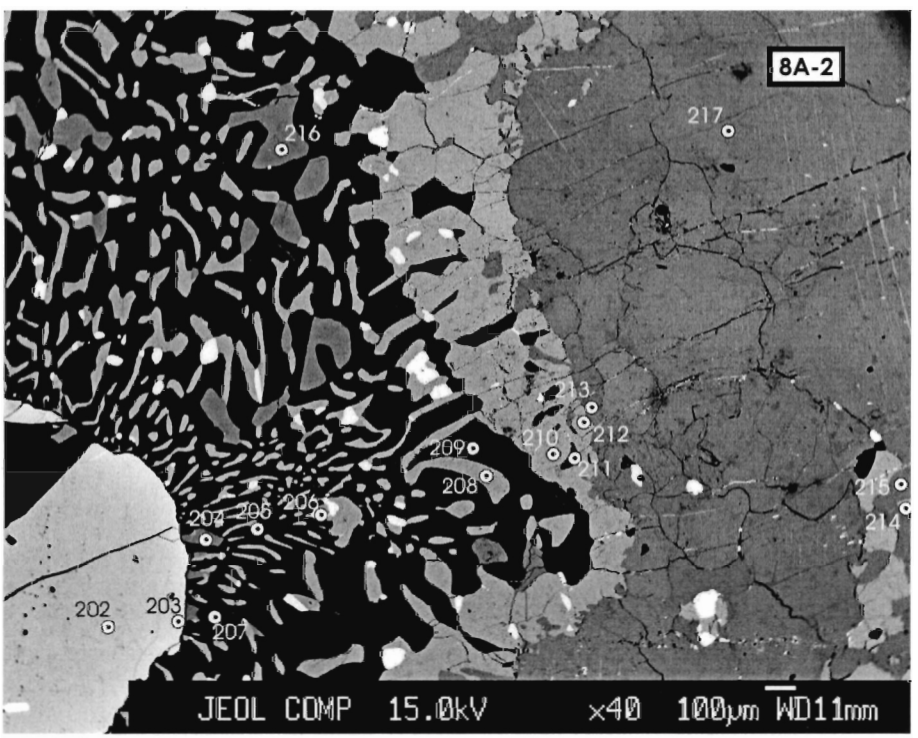
8A-2
216
217
213
212
209
208
211
215
214
204
205
206
202
203
207
JEOL COMP 15.0kV x40 100µm WD11mm

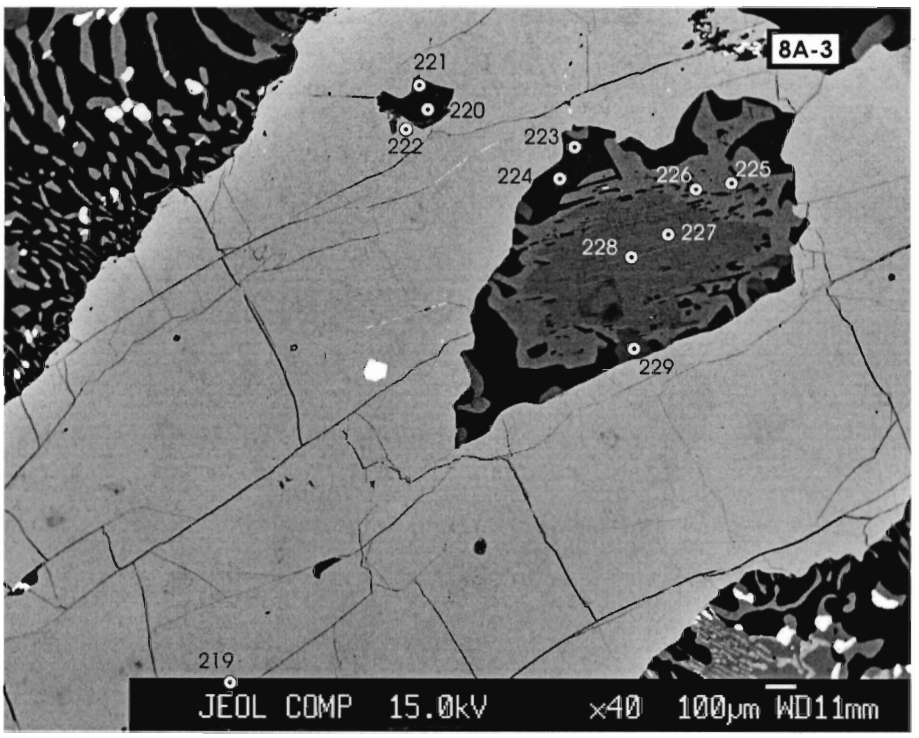
8A-3
221
220
222
223
224
226
225
227
228
229
219
JEOL COMP 15.0kV x40 100µm WD11mm

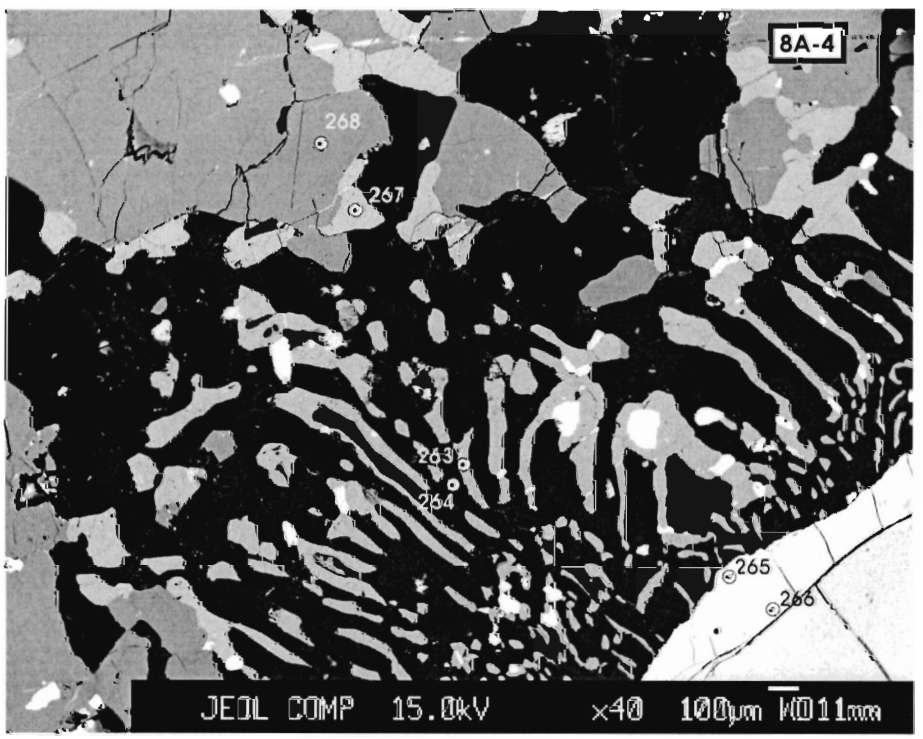
8A-4
268
267
263
264
265
266
JEOL COMP 15.0kV x40 100µm WD11mm

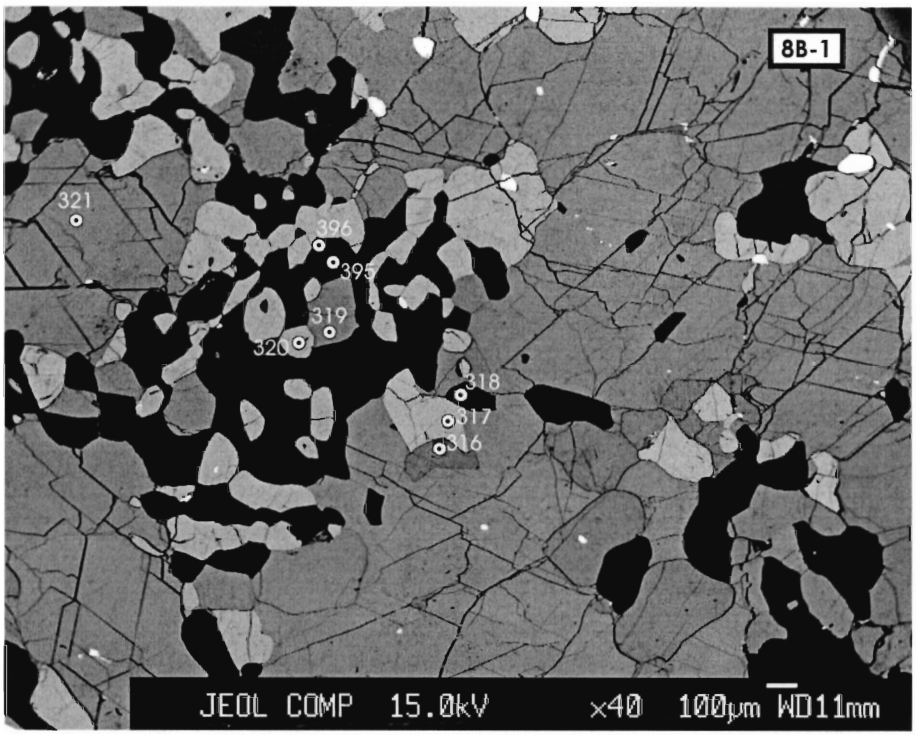
8B-1
321
396
395
319
320
318
317
316
JEOL COMP 15.0kV x40 100µm WD11mm

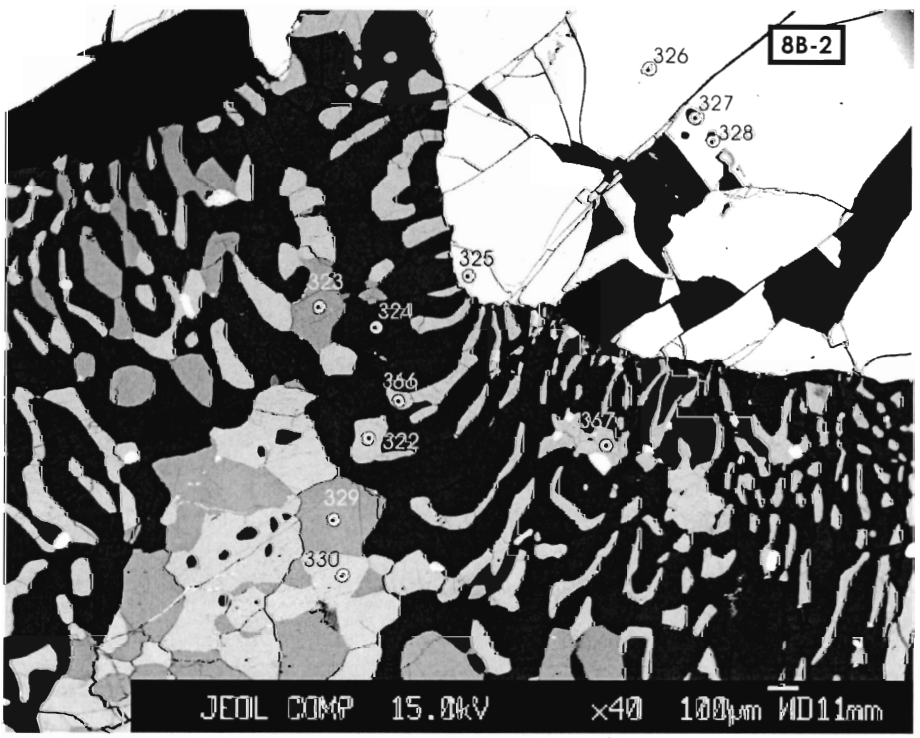
8B-2
326
327
328
325
324
322
329
330
JEOL COMP 15.0kV x40 100µm WD11mm

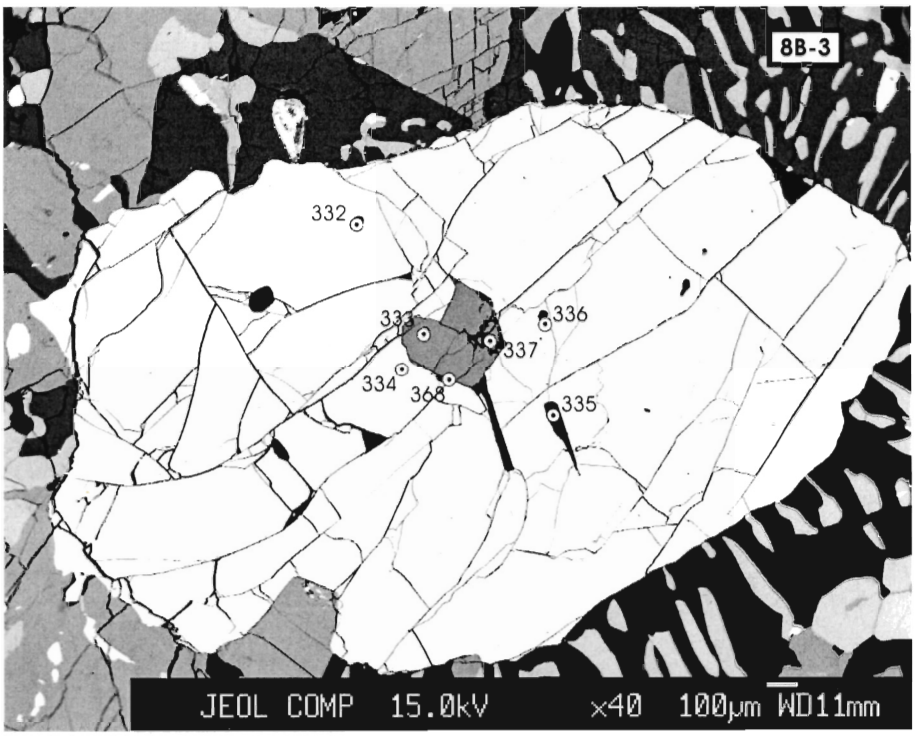
8B-3
332
333
336
337
334
368
335
JEOL COMP 15.0kV x40 100µm WD11mm

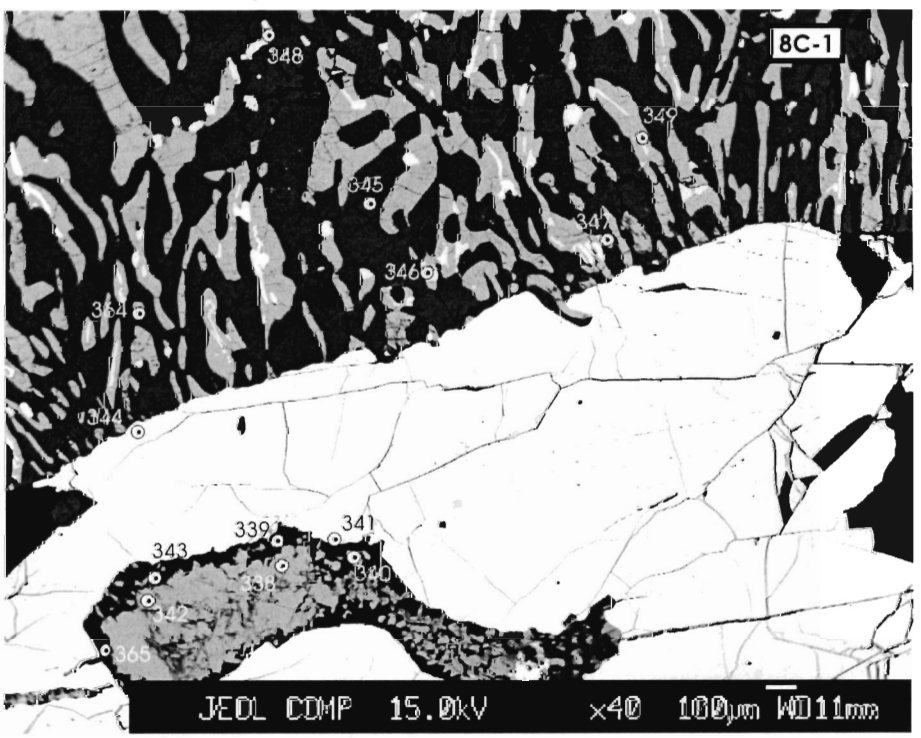
8C-1
348
349
345
347
346
364
344
339
341
343
340
342
365
JEOL COMP 15.0kV x40 100µm WD11mm

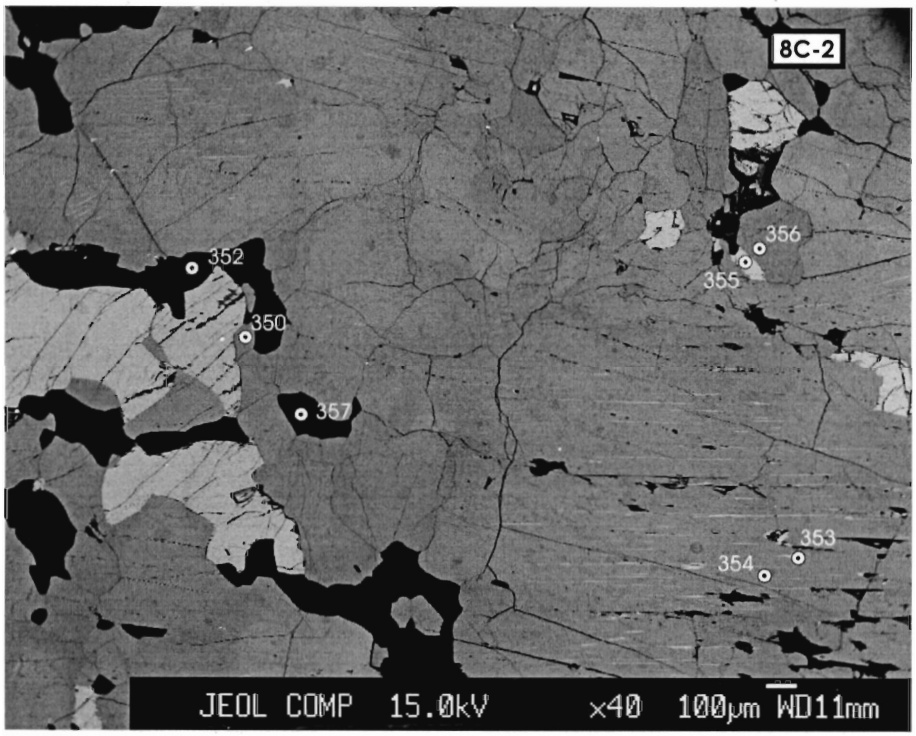
8C-2
352
350
357
356
355
353
354
JEOL COMP 15.0kV ×40 100μm WD11mm

APPENDIX C
AR-AR THERMOCHRONOLOGY

Results for $^{39}Ar/^{40}Ar$ analyses from selected samples are presented in Tables C.1, C.2, C.3, and C.4.

Samples were irradiated at the McMaster University Nuclear Reactor in Hamilton, Ontario on December 3rd, 2007. Samples were irradiated in a high neutron flux site 5C in the reactor. They were contained in ~1cm diameter high-purity Aluminium foil in individual containers, interleaved vertically with standards in a single C-103 type canister. The canister is ~5cm long and lined with Cadmium to shield neutrons which would cause unwanted interfering reactions. The standard used for Ar corrections and J calculations was the Fish Canyon tuff sanadine with an age of 28.13 ± 0.1 Ma.

Table C.1 $^{39}Ar/^{40}Ar$ results for Y105A

T°C	^{39}Ar(mV)	^{39}Ar(%)	AGE (Ma)±1Õ	% ATM	$^{37}Ar/^{39}Ar$	$^{36}Ar/^{40}Ar$	$^{39}Ar/^{40}Ar$	% IIC
750	1.8	0.3	2884 ± 56	69.5	2.71	0.002352	0.000181	0.18
950	2.2	0.4	4449 ± 10	4.9	4.99	0.000168	0.000207	0.33
1000	34.8	6.1	1772 ± 6	0.8	3.9	0.000027	0.001398	0.29
1025	51	9	1766 ± 6	0.5	3.61	0.000017	0.001409	0.27
1050	200.3	35.6	1768 ± 6	0.2	3.64	0.00001	0.00141	0.27
1075	179	31.8	1762 ± 6	0.3	3.53	0.00001	0.001418	0.26
1100	64.1	11.4	1751 ± 6	0.6	3.51	0.000021	0.001427	0.26
1150	6.9	1.2	1752 ± 10	9.5	4.78	0.000324	0.001297	0.36
1200	4.8	0.8	1785 ± 18	17.7	6.88	0.000601	0.001146	0.52
1250	4.2	0.7	1842 ± 20	21.8	7.78	0.000739	0.001036	0.58
1350	12.4	2.2	1813 ± 10	14	11.42	0.000475	0.001168	0.86

MEAN AGE(1000°C-1100°C)= 1764 ± 12 Ma (2Õ UNCERTAINTY, INCLUDING ERROR IN J)
J = 0.002356 ± .0000215

Table C.2 $^{39}Ar/^{40}Ar$ results for Y106

T°C	^{39}Ar(mV)	^{39}Ar(%)	AGE (Ma)±1Õ	% ATM	$^{37}Ar/^{39}Ar$	$^{36}Ar/^{40}Ar$	$^{39}Ar/^{40}Ar$	% IIC
750	1.9	0.4	2438 ± 63	73.5	1.12	0.00249	0.000219	0.07
850	0.2	0	32469 ± 19	19.5	1.26	0.000661	0.000379	0.08
950	3.6	0.8	2095 ± 8	11.5	8.02	0.000389	0.000961	0.58
975	12.3	3	1789 ± 6	2.1	5.17	0.000072	0.001375	0.39
1000	32.5	7.9	1751 ± 6	1.6	3.98	0.000056	0.001429	0.3
1025	48.5	11.8	1732 ± 6	0.6	4.81	0.000021	0.001469	0.36
1050	76	18.5	1740 ± 6	0.4	4.77	0.000016	0.00146	0.36
1075	120.6	29.3	1769 ± 6	0.2	4.16	0.000007	0.001427	0.31
1100	74.3	18.1	1727 ± 6	0.7	3.39	0.000025	0.001473	0.25
1125	7.9	1.9	1761 ± 13	8.6	4.76	0.000294	0.001315	0.36
1150	4.7	1.1	1717 ± 20	16.4	5.16	0.000556	0.001251	0.39

MEAN AGE(975°C-1200°C)= 1748 ± 11Ma (2σ UNCERTAINTY, INCLUDING ERROR IN J)
J = 0.002384 ± .0000215

Table C.3 $^{39}Ar/^{40}Ar$ results for Y107

T°C	^{39}Ar(mV)	^{39}Ar(%)	AGE (Ma)±1Õ	% ATM	$^{37}Ar/^{39}Ar$	$^{36}Ar/^{40}Ar$	$^{39}Ar/^{40}Ar$	% IIC
750	3.7	0.7	1419 ± 59	78.1	12.28	0.002644	0.000432	0.98
950	13.8	2.9	1755 ± 6	7.7	3.52	0.000262	0.001327	0.26
975	11.4	2.4	1704 ± 9	0.8	1.85	0.000029	0.001494	0.14
1000	12.2	2.5	1709 ± 10	0.4	2.85	0.000016	0.001492	0.21
1025	22.8	4.8	1713 ± 7	0.2	3.85	0.000009	0.001489	0.29
1050	51.8	10.9	1709 ± 6	0.1	4.03	0.000004	0.001497	0.3
1075	117.1	24.7	1724 ± 6	0.1	3.76	0.000004	0.001477	0.28
1100	127.4	26.8	1724 ± 6	0.1	4.01	0.000004	0.001478	0.3
1150	90.1	19	1709 ± 6	0.1	4.26	0.000003	0.001497	0.32
1200	5.2	1.1	1725 ± 12	2.8	4.23	0.000096	0.001436	0.32
1250	5.3	1.1	1718 ± 14	3	4.04	0.000102	0.001442	0.3

MEAN AGE(1025°C-1150°C)= 1718 ± 12 Ma (2σ UNCERTAINTY, INCLUDING ERROR IN J)
J = 0.002369 ± .0000215

Table C.4 $^{39}Ar/^{40}Ar$ results for Y108

T°C	^{39}Ar(mV)	^{39}Ar(%)	AGE (Ma)±1Õ	% ATM	$^{37}Ar/^{39}Ar$	$^{36}Ar/^{40}Ar$	$^{39}Ar/^{40}Ar$	% IIC
750	2.3	0.3	1614 ± 88	83.4	17.67	0.002822	0.000274	1.37
950	2.7	0.4	2713 ± 9	9.3	18.34	0.000317	0.00062	1.28
975	11.6	1.7	1773 ± 9	0.7	6.41	0.000025	0.001422	0.48
1000	29.3	4.4	1757 ± 6	0.2	6.6	0.000009	0.00145	0.5
1025	66.7	10.1	1743 ± 6	0.1	6.48	0.000004	0.00147	0.49
1050	137	20.7	1754 ± 6	0	6.64	0.000002	0.001456	0.5
1075	246.3	37.3	1755 ± 6	0	5.56	0.000002	0.001455	0.42
1100	120.6	18.2	1759 ± 6	0.1	6.32	0.000004	0.001449	0.48
1150	16.2	2.4	1742 ± 8	1.5	7.32	0.000052	0.00145	0.55
1200	6.9	1	1808 ± 9	4.7	8.72	0.00016	0.001324	0.65
1250	4.1	0.6	1770 ± 22	6.9	9.19	0.000234	0.001337	0.69

MEAN AGE(975°C-1150°C)= 1754 ± 12 Ma (2σ UNCERTAINTY, INCLUDING ERROR IN J)
J = 0.002397 ± .0000215